

All-Polymer Electrochemical Sensors

Kafka, Jan Robert; Larsen, Niels Bent; Skaarup, Steen; Geschke, Oliver

Publication date:
2012

Document Version
Publisher's PDF, also known as Version of record

[Link back to DTU Orbit](#)

Citation (APA):
Kafka, J. R., Larsen, N. B., Skaarup, S., & Geschke, O. (2012). All-Polymer Electrochemical Sensors. Kgs. Lyngby: Technical University of Denmark (DTU).

DTU Library

Technical Information Center of Denmark

General rights

Copyright and moral rights for the publications made accessible in the public portal are retained by the authors and/or other copyright owners and it is a condition of accessing publications that users recognise and abide by the legal requirements associated with these rights.

- Users may download and print one copy of any publication from the public portal for the purpose of private study or research.
- You may not further distribute the material or use it for any profit-making activity or commercial gain
- You may freely distribute the URL identifying the publication in the public portal

If you believe that this document breaches copyright please contact us providing details, and we will remove access to the work immediately and investigate your claim.

All-Polymer Electrochemical Sensors

PhD Thesis

Jan Kafka

Supervisor: Niels Bent Larsen

Co-supervisors: Steen Skaarup and Oliver Geschke

Department of Micro- and Nanotechnology

Technical University of Denmark

February 2012



Preface

This thesis is one the requirements to fulfill in order to obtain the Ph.D. degree from the Technical University of Denmark. The work presented in this thesis has been carried out at the Department of Micro- and Nanotechnology (DTU Nanotech) at the Technical University of Denmark from July 2007 to February 2012, within the group for POEM and Polymer Microsystems for Cell Processing. This work was financially supported by the Danish Research Council for Technology and Production Sciences grant no. 26-04-0074.

The project was supervised by prof. Niels Bent Larsen (supervisor, DTU - Department of Micro- and Nanotechnology), associate professor Oliver Geschke (co-supervisor, Department of Micro- and Nanotechnology and Aquaporin A/S) and associate professor Steen Skaarup (co-supervisor, Department of Chemistry)

First of all, I would like to thank my supervisors: Oliver Geschke for the helpful introduction into the project, Niels Bent Larsen for the great support at any time, the inspiring discussions and the interest in even the smallest problems (as long as they were of great importance for myself), and finally Steen Skaarup for his patient explanations of electrochemical processes, the practical help by exploring electrochemical mysteries, and the support during the final writing period.

I would like to thank all former and current members of the POEM and Polymer Cell group, especially Thomas Steen Hansen who introduced me into the PEDOT handling and Johan Ulrik Lind for the fruitful discussions about successful and unsuccessful experiments. I am deeply grateful about the discussions with Maciej Skolimowski and his tireless efforts to teach me new software like SolidWorks or Comsol. I would also like to thank him and Joanna M. Lopacinska for helping us with our kids, especially during periods of heavy workload.

At last I would like to thank my friends and family, especially my mother, Maria, Ria, and Finn for their great support and understanding of my absence especially during the last month of my project.

Abstract

This thesis presents fabrication strategies to produce different types of all-polymer electrochemical sensors based on electrodes made of the highly conductive polymer poly(3,4-ethylenedioxythiophene) (PEDOT). Three different systems are presented, fabricated either by using microdrilling or by hot embossing. Microdrilling was applied to fabricate arrays of circular as well as tubular electrodes, while hot embossing was used to produce planar electrodes.

Arrays of circular electrodes were produced by using a new fast prototyping strategy for fabrication of microelectrodes. Electrical resistance-controlled microdrilling was applied to drill through an insulating polymer, covering a conductive layer of PEDOT. The sudden drop in electrical resistance between the metal drill and the PEDOT layer upon physical contact was employed as a stop criterion for the drilling process. Arrays of 3 × 3 microelectrodes of diameter 30 μm or 100 μm, respectively, with center-to-center electrode spacings of either 130 μm or 300 μm were fabricated. Their functionality was verified by amperometry on potassium ferrocyanide. Comparison of the experimentally obtained results to finite element modeling of the respective electrode configurations showed that the conducting polymer electrodes approach the steady state currents predicted from modeling, but at a much slower rate than expected. This was shown to be caused by the use of electroactive PEDOT electrodes. Subtraction of the latter contribution gave an approach to steady state currents within a few seconds, which was in very good agreement with the modeled response time.

Arrays of tubular electrodes were fabricated by drilling through a cyclic olefin copolymer (COC) foil which was modified with spin coated layers of polystyrene, PEDOT, and a second layer of polystyrene. The drilling process resulted in a cylindrical drilling shaft, later used as microfluidic channel, and a tubular electrode integrated in the shaft sidewall. A modification of the backside of the COC foil with a polystyrene and a PEDOT layer before the drilling process allowed the simultaneous fabrication of an additional planar electrode at the end of the drilling shaft. Arrays of ten Ø 100 μm tubular electrodes (center-to-center spacing of 300 μm) were produced. The reproducibility of the fabrication method was confirmed by consistent amperometric responses of independent fabricated electrode arrays towards potassium ferrocyanide. A sensor application was demonstrated by amperometric detection of hydrogen peroxide concentrations in the range of 0.1 to 5 mM.

Planar electrodes were fabricated by hot embossing of a microfluidic channel with sloped sidewalls into a PEDOT covered COC bulk material. During embossing the PEDOT layers at the sloped sidewalls became part of the channel while retaining electrical contact to the surface layer. Consequently, the PEDOT layers at the sloped area could be used as electrodes. Electrodes placed on opposite channel sidewalls were spatially separated by the microfluidic channel in between. The electrical insulation of the PEDOT electrodes from the PEDOT at the channel bottom was achieved by embossing a vertical step. Functionality of the final thermally bonded system was shown by amperometric detection of physiologically relevant glucose concentrations (0–10 mM).

Resumé

I denne afhandling præsenteres en række strategier til at fremstille elektrokemiske sensorer bestående udelukkende af polymerer. Sensorerne er baseret på poly(3,4-ethylenedioxythiophene) (PEDOT), en polymer med høj elektrisk ledningsevne. Tre forskellige systemer præsenteres, fabrikeret enten vha. mikroboring eller varmeprægning. Mikroboring blev benyttet til at fremstille mønstre af cirkulære såvel som rør-formede elektroder, mens varmeprægning blev benyttet til at fremstille plane elektroder.

Cirkulære elektroder blev fremstillet vha. en ny hurtig metode til at lave prototyper af mikroelektroder. Mikroboring blev benyttet til at bore gennem en elektrisk isolerende polymer placeret ovenpå en PEDOT film, styret af den elektriske modstand. Et pludseligt fald i den elektriske modstand mellem metalboret og PEDOT-filmen blev benyttet som kriterium for at stoppe boringen. Mønstre af 3 x 3 mikroelektroder med en diameter på 30 μm eller 100 μm , og med en center-til-center afstand på enten 130 μm eller 300 μm , blev fremstillet. Funktionaliteten af de fremstillede elektroder blev vist via amperometrisk måling af kalium ferro-/ferricyanid. Sammenligning af de eksperimentelle resultater med "finite element" modellering af de respektive elektrodekonfigurationer viste at strømstyrken nærmer sig en konstant værdi som fundet i modelleringen, men langsommere end forventet. Dette viste sig at være forårsaget af anvendelsen af PEDOT elektroder, som er elektroaktive. Efter fratrækning af elektrodernes bidrag opnås en konstant strømstyrke allerede indenfor få sekunder, i god overensstemmelse med responstiden i modelleringerne.

Mønstre af rørformede elektroder blev fremstillet vha. boring gennem en folie af cyklisk-olefin-co-polymer (COC) dækket med tre lag polymerer, først et lag polystyren, dernæst et lag PEDOT, og endelig endnu et lag polystyren. Boreprocessen efterlod en cylindrisk skakt som senere kunne anvendes som mikro-væskekanal med en rørformet elektrode integreret i skaktens sidevæg. Ved at modificere bagsiden af COC folien med et lag polystyren og et lag PEDOT før boreprocessen, kunne der samtidig yderligere fremstilles en plan elektrode ved enden af boreskakten. Et mønster af ti \varnothing 100 μm rørformede elektroder med en center-til-center afstand på 300 μm blev fremstillet. Fremstillingsmetodens reproducerbarhed blev bekræftet ved en række konsistente amperometriske målinger af kalium ferrocyanid på et antal uafhængigt fremstillede prøver. Der blev yderligere demonstreret amperometrisk måling af hydrogenperoxid i koncentrationer fra 0,1 mM til 5 mM.

Plane elektroder blev fremstillet ved varmeprægning af en mikro-væskekanal med skrånede sidevægge af en PEDOT film på et COC substrat. Under prægningen kom PEDOT laget på de skrånede sidevægge til at udgøre en del af kanalens længde samtidig med at den elektriske kontakt til overfladelaget bevarede. PEDOT film i de skrå områder kunne derfor anvendes som elektroder i kanalen. PEDOT elektroderne blev elektrisk isoleret fra PEDOT i kanalbunden ved at benytte et stempel med et lodret trin efter de skrånede vægge. Funktionaliteten af det endelige system blev vist ved amperometrisk detektion af glukose i fysiologisk relevante koncentrationer (0-10 mM).

Conference Proceedings

J. Kafka, N. B. Larsen, S. Skaarup and O. Geschke, Fabrication of an all polymer electrochemical sensor, DBS 2009, Freiburg, Germany (poster presentation) (29/03/09 - 01/04/09)

J. Kafka, N. B. Larsen, S. Skaarup and O. Geschke, Hot embossing of a polymeric electrochemical sensor based on poly(3,4-ethylenedioxythiophene), COMS 2009, Copenhagen, Denmark (oral presentation) (30/08/09 - 04/09/09)

J. Kafka, N. B. Larsen, S. Skaarup and O. Geschke, Fabrication of an all-polymer electrochemical sensor by using a one-step hot embossing procedure, MNE 2009, Ghent, Belgium (oral presentation) (28/09/09 – 01/10/09)

J. Kafka, N. B. Larsen, S. Skaarup and O. Geschke, One-step fabrication of an all-polymer electrochemical sensor by hot embossing, MicroTAS 2009, Jeju Island, South Korea (poster presentation) (01/11/09 - 05/11/09)

J. Kafka, O. Geschke, S. Skaarup and N. B. Larsen, Fast prototyping of conducting polymer microelectrodes using resistance-controlled high precision drilling, MNE 2010, Genoa, Italy (poster presentation) (19/09/10 – 22/09/10)

Publications

J. Kafka, N. B. Larsen, S. Skaarup, O. Geschke; Fabrication of an all-polymer electrochemical sensor by using a one-step hot embossing procedure; *Microelectronic Engineering* 87 (2010) 1239–1241

J. Kafka, O. Geschke, S. Skaarup, N. B. Larsen; Fast prototyping of conducting polymer microelectrodes using resistance-controlled high precision drilling; *Microelectronic Engineering* 88 (2010) 2589-2592

Table of Content

Preface	i
Abstract	ii
Resumé	iii
Conference proceedings	iv
Publications	iv
1 Introduction	1
1.1 Background and Motivation	2
1.2 Outline of the Thesis	4
2 Polymers for Microfluidic Systems	7
2.1 Non-Conducting Polymers	8
2.2 Conducting polymers	10
2.3 References	13
3 Microfabrication Methods	15
3.1 Micromachining	16
3.1.1 Introduction to Micromachining Processing	16
3.1.2 Analyses of Milling Equipment	21
3.1.3 Optimization of Micromilling Parameters	25
3.1.4 Stamp Fabrication for Hot Embossing	36
3.1.5 References	39
3.2 Hot Embossing	41
3.2.1 The Hot Embossing Process	42
3.2.2 Optimization of the Hot Embossing Process	44
3.2.3 References	51

3.3	Bonding of Microfluidic Channels	52
3.3.1	Indirect Bonding Techniques – “Adhesive Bonding”	52
3.3.2	Direct Bonding Techniques	52
3.3.3	References.....	54
4	Conducting Polymers in Electrochemical Biosensors.....	55
4.1	Electrochemical Biosensors.....	56
4.1.1	The Biological Recognition Element.....	56
4.1.2	Glucose Selective Electrodes	57
4.1.3	Integration of Electrodes into Polymer Fluidic Systems	57
4.2	Spin Coating of PEDOT	58
4.2.1	PEDOT Single-Layer Synthesis.....	59
4.2.2	PEDOT Multilayer Synthesis.....	64
4.3	Hydrogen Peroxide Detection on Prussian Blue modified PEDOT Layers	66
4.4	References.....	71
5	Fabrication of All-Polymer Electrochemical Sensors	75
5.1	Fast Prototyping of Conducting Polymer Microelectrodes using Resistance-Controlled High Precision Drilling	76
5.1.1	Introduction.....	76
5.1.2	Fabrication of Circular-Electrodes.....	77
5.1.3	Bonding.....	80
5.1.4	Finite Element Modelling of Electrode Arrays.....	81
5.1.5	Electrochemical Analysis of Microelectrodes	83
5.1.6	Summary	85
5.1.7	References.....	85

5.2	Fabrication of an All-Polymer Electrochemical Microfluidic System using a One-Step Microdrilling Procedure	86
5.2.1	Introduction	86
5.2.2	Fabrication Principle	87
5.2.3	Design of Spin Coating Chuck.....	88
5.2.4	Coherence of the PEDOT/TOPAS Assembly.....	90
5.2.5	Drilling of Electrode Arrays.....	93
5.2.6	Deformation of PEDOT during the Drilling Process.....	96
5.2.7	Optimized Electrode Array Fabrication	99
5.2.8	Bonding	100
5.2.9	The Electrochemical Microfluidic System.....	101
5.2.10	Summary	105
5.2.11	References:	106
5.3	Fabrication of an Electrochemical System by a One Step Hot Embossing Procedure	107
5.3.1	Introduction	107
5.3.2	Embossing of Isolated PEDOT Areas.....	109
5.3.3	Embossing of Sloped PEDOT Areas	112
5.3.4	Design of the Electrochemical Microfluidic System	117
5.3.5	Bonding of the Electrochemical Microfluidic System.....	119
5.3.6	Glucose Detection	122
5.3.7	Summary	125
5.3.8	References	125
6	Conclusions.....	129
7	Appendices	133

Chapter 1

Introduction

1.1 Background and Motivation

Sensors are devices that are based on a coupling of a recognition element with a transducer element and allow direct measurements of analytes in a sample [Zhang, 2008]. Electrochemical sensors, a sub-class of the chemical sensors, employ electrodes as transducer element, usually in a two or three electrode arrangement. The electrodes convert chemical signals into electrical signals. In most cases the sensor reaction takes place at the electrode-analyte interface which results in a high reliability, a low detection limit and a wide dynamic range of electrochemical sensors [Rozlosnik, 2009].

The miniaturization of electrodes yields faster response times and higher sensitivities of electrochemical sensors since microelectrodes experience a higher mass transfer rate at the electrode boundary and less interference from interfacial capacity. The application of microelectrodes enables measurements in highly resistive environments as well as very small sample volumes [Rozlosnik, 2009]. Due to the small size, microelectrodes yield currents in nanoampere range which requires very sensitive equipment and a well insulated electrical setup. The use of microelectrode arrays increases the resulting current and at the same time keeps the advantages of microelectrodes. However this is only valid for a proper array arrangement as discussed later in this thesis.

The first miniaturized electrochemical microfluidic systems were based on relative expensive silicon- or glass-based substrates fabricated by cleanroom technologies including photolithography and wet etching process [Illa, 2010]. Since these techniques were already well established and optimized for microelectronics, comparably small effort had to be done to adjust them for the fabrication of electrochemical microfluidic systems. The reduction in size and parallelization enabled fabrication of silicon based electrochemical sensors at reasonable prices and therefore a wide commercial application of these sensors in fields of clinical, industrial, environmental, and agricultural analysis [Zhang, 2008]. However, the high cost of the material, the many serial fabrication steps (cleaning, resist coating, photolithography, development, wet etching), and limitations on possible geometries lead to an increasing demand for new materials and fabrication methods [Becker and Gärtner, 2000; Illa, 2010].

The variety of low-cost polymer materials, especially thermoplastics, allowed a replacement of silicon and glass for many microfluidic applications. Subsequently microfluidic systems could be defined by applying high through-put forming strategies like hot embossing and injection molding which simplified the fabrication process. However, most thermoplastics could not withstand organic solvents as used in conventional photolithography processes for microelectrode fabrication [Becker and Gärtner, 2008]. New strategies were developed to overcome this issue: electrodeposition of metal through a mask [Takano, 2006], airbrushing [Walker, 2008] or ink-jet printing [Lesch, 2012] of metal particles containing solutions are

some of a variety of new methods to define metal based electrodes on polymer surfaces. Today, screen printing is the commonly used technique to apply and define electrodes on polymer surfaces. A carbon or metal based paste is applied through a mask to predefined surface areas. This technique allows low-cost fabrication of miniaturized and disposable electrochemical systems such as commercially available glucose sensors [Ahmed, 2007].

The higher conductivity and increased stability of conducting polymers over the last decades enabled the development of environmental friendly and low-cost electrochemical systems, completely based on polymers. Conducting polymers are still less conductive and less stable than noble metals which limits the area of applications. However, they are promising candidates for sensor applications where a high conductivity is not required [Rozlosnik, 2009].

Conducting polymers are easy to synthesize (in some cases also available in a prepolymerized state) and can be processed with structuring methods established for non-conducting polymers. The latter point is an important advantage for the optimization of the fabrication of electrochemical systems. If the non-conducting polymer support and the conducting polymer can be structured with the same techniques, it is only a matter of process optimization to combine both processes into one fabrication step. One-step fabrication processes not only reduce the fabrication time, they also minimize the risk of structural failures and contaminations during successive process steps as well as misalignments of fabricated electrodes and microfluidics during the final assembling of the sensor.

The aim of this work was to establish novel fabrication strategies for all-polymer electrochemical sensors. Three systems based on different types of electrodes were fabricated:

- a) Arrays of circular electrodes with different electrode arrangements
- b) Arrays of tubular electrodes by simultaneous integration into a microfluidic system
- c) Planar electrodes defined on slopes in microfluidic channel sidewalls

1.2 Outline of the Thesis

This thesis explores the necessary steps to fabricate three developed types of all-polymer, electrochemical microfluidic sensor systems. The thesis is divided into five main chapters: an introduction to commercially available polymers (Chapter 2), a part on polymer fabrication (Chapter 3), an overview of the applications of conducting polymers in electrochemical biosensors (Chapter 4), fabrication and analysis of the developed electrochemical systems (Chapter 5), and final conclusions (Chapter 6).

Chapter 2 gives a short introduction to commercially available non-conducting polymers (Chapter 2.1) and conducting polymers (Chapter 2.2) and discusses the beneficial properties of the non-conducting polymer TOPAS (a cyclic olefin copolymer) as well as the conducting polymer poly(3,4-ethylenedioxythiophene) (PEDOT).

Chapter 3 presents the theoretical background and necessary optimization steps towards accurate and reproducible fabrication of polymeric microfluidic systems. This includes the basics about micromachining operations with focus on microdrilling and micromilling as well as the fabrication of aluminum stamps (Chapter 3.1). A hot embossing based fabrication of microfluidic devices is discussed in Chapter 3.2. Finally bonding techniques are presented in order to encapsulate the fabricated open microfluidic channels (Chapter 3.3).

Chapter 4 discusses the integration of conducting polymers into electrochemical biosensors. After an overview about developed electrochemical biosensors, principles of electrochemical glucose sensing based on the detection of hydrogen peroxide are presented (Chapter 4.1). Theoretical background, the advantages as well as the optimization of spin coating processes are discussed in Chapter 4.2 which are applied to a spin coating based synthesis of a hydrogen peroxide sensitive electrode material (Chapter 4.3).

Chapter 5 presents the three fabricated electrochemical systems:

- Arrays of circular electrodes (Chapter 5.1):

Circular electrodes were fabricated by drilling through an insulating layer of non-conducting TOPAS to an underlying conducting PEDOT layer. The drilling process was stopped before drilling through the conducting polymer. The physical contact between the tool and the PEDOT layer was determined by an innovative resistant controlled microdrilling strategy. The resulting exposed circular PEDOT areas were following used as electrodes. The amperometric response to potassium ferrocyanide of arrays with electrodes of different diameters as well as different electrode spacing were recorded and verified using a finite element modeling.

- Arrays of tubular electrodes (Chapter 5.2):

Tubular electrodes were produced by drilling through a TOPAS foil modified with a conducting layer of PEDOT which was insulated on both sides with a layer of polystyrene. Drilling through the entire foil resulted in a cylindrical drilling shaft with an integrated tubular electrode in the shaft sidewall. A further modification of the backside of the TOPAS foil with a polystyrene and a PEDOT layer before the drilling process resulted in an additional planar electrode at the end of the drilling shaft. For the final application as electrochemical system, the drilling shaft was used as microfluidic channel, the tubular electrode as working electrodes and the planar electrode as counter electrode. Thus, the entire electrochemical system was finally fabricated in only one single microdrilling step. A sensor application was demonstrated by detecting different hydrogen peroxide concentrations after prussian blue modification of the PEDOT layer which was used as working electrode.

- Planar electrodes (Chapter 5.3):

Two planar electrodes were fabricated simultaneously by embossing a microfluidic channel with sloped sidewalls into a PEDOT covered TOPAS bulk substrate. Sloped sidewalls allowed an integration of the PEDOT layer into the microfluidic channel. The PEDOT layers on the sloped sidewalls were used as working and counter electrodes. The electrical insulation of the PEDOT electrodes from the PEDOT at the channel bottom was achieved by embossing a vertical step. Functionality of the electrochemical system was demonstrated by sensing glucose in physiologically relevant concentrations after a modification of the PEDOT with prussian blue and immobilization of glucose oxidase at the working electrode.

Chapter 6 presents the conclusions of the work.

References

- [Ahmed, 2008] Ahmed, M. U.; Hossain, M. M.; Tamiya, E. *Electroanalysis* 2008, 20, 616-626
- [Becker and Gärtner, 2000] Becker, H.; Gärtner, C. *Electrophoresis* 2000, 21, 12-26
- [Becker and Gärtner, 2008] Becker, H.; Gärtner, C. *Analytical and bioanalytical chemistry* 2008, 390, 89-111
- [Illa, 2010] Illa, X.; Ordeig, O.; Snakenborg, D.; Romano-Rodríguez, A.; Compton, R. G.; Kutter, J. P. *Lab on a chip* 2010, 10, 1254-61
- [Lesch, 2011] Lesch, A.; Momotenko, D.; Cortés-Salazar, F.; Wirth, I.; Tefashe, U. M.; Meiners, F.; Vaske, B.; Girault, H. H.; Wittstock, G. *Journal of Electroanalytical Chemistry* 2011, 666, 52-61
- [Rozlosnik, 2009] Rozlosnik, N. *Analytical and bioanalytical chemistry* 2009, 395, 637-45
- [Takano, 2006] Takano, N.; Doeswijk, L. M.; Boogaart, M. a F. V. D.; Auerswald, J.; Knapp, H. F.; Dubochet, O.; Hessler, T.; Brugger, J. *Journal of Micromechanics and Microengineering* 2006, 16, 1606-1613
- [Walker, 2008] Walker, C. E.; Xia, Z.; Foster, Z. S.; Lutz, B. J.; Fan, Z. H. *Electroanalysis* 2008, 20, 663-670
- [Zhang, 2008] Zhang, X.; Ju, H. Wang, J.; *Electrochemical Sensors, Biosensors and Their Biomedical Applications*, Elsevier; ISBN: 978-0-12-373738-0

Chapter 2

Polymers for Microfluidic Systems

2.1 Non-Conducting Polymers

The right choice of the polymer depends on the fabrication method as well as the final application. A cross-linked polymer, for example, can not be molded by hot embossing or injection molding once it is cured. A polymer which does not absorb light in the infrared range can not be structured by a carbon dioxide laser. Systems which have to withstand applied forces should not be made from elastic polymers, etc.

Commercially available polymers can be divided into three main groups: Thermosets, elastomers, and thermoplastics. The classification is based on the type of interconnection of the polymer chains within the polymer substrate [Becker and Gärtner, 2000].

Thermosets

Thermosets are strong covalent cross-linked polymers which are obtained by curing of a soft solid or viscous prepolymer. The curing is induced by heat, or suitable radiation, or both [IUPAC]. Thermosets have to be casted in their final shape, since the cross-linked polymer network does not allow molecular movement of the chains for a change in shape afterwards. Even the curing process takes place within some seconds, the device throughput is limited since the preparation time of the thermosetting prepolymer solution and further process steps involved are in the range of many minutes. This limits the application of thermosets mainly to academic use [Becker and Gärtner, 2008].

Elastomers

Elastomers have a low density of cross-links between the polymer chains and thus they display a rubber-like elasticity [IUPAC]. If an external force is applied, elastomers are able to elongate. If the force is withdrawn, the polymer relaxes and returns to the original shape [Becker and Gärtner, 2000]. Due to low cost and easy handling, elastomers became a primary material for low-volume fabrication of microfluidic devices. The oxygen and carbon dioxide permeability made elastomers, e.g. poly(dimethylsiloxane) (PDMS), well suited for cell-based system [Becker and Gärtner, 2008].

Thermoplastics

Most thermoplastics are high molecular weight polymers. The polymer chains are associated through intermolecular forces such as *van der Waals* or dipole-dipole forces. Thermoplastics soften when heated up to a type specific temperature range, called glass transition temperature (T_g). At temperatures equal to or higher than the T_g, thermoplastic polymers can be processed

by hot embossing or injection molding in order to mold them into a specific shape, which they will retain after cooling below the glass transition temperature [Becker and Gärtner, 2000].

The possibility of fast and easy molding made thermoplastics very interesting for research, but especially for industrial applications. A large variety of microfabrication methods like micromilling, laser ablation, hot embossing or injection molding have been optimized for fabrication of thermoplastic based microfluidic systems.

The first applications of thermoplastics in microfluidics were largely focused on polycarbonate (PC) and poly(methyl methacrylate) (PMMA). Both polymers were already well known and therefore well characterized. Among others cyclic olefin polymers (COP) and cyclic olefin copolymers (COC) are extremely promising for recent microfluidic applications. [Becker and Gärtner, 2000 and 2008]

TOPAS

TOPAS is a cyclic olefin copolymer (COP) synthesized by TOPAS Advanced Polymers. Apart from TOPAS, cyclic olefin copolymers are also available from other manufactures like Mitsui Chemicals, Ticona, Japan Synthetic Rubber, and Zeon Chemicals [Shin, 2005]. TOPAS combines beneficial properties with regard to microfluidic systems, like [TOPAS, Advanced Polymers, Shin, 2005 (and included references)]:

- high optical transparency even into the near UV range,
- highly insulating ($> 10^{14} \Omega \cdot m$),
- low water absorption ($< 0.01\%$),
- good processability,
- excellent biocompatibility,
- high resistance to acids, alkalis, as well as organic solvents.



Figure 1: chemical structure of TOPAS, consisting of ethylene and norbornene subunits. [adapted from TOPAS Advanced Polymers]

TOPAS is synthesized from norbornene and ethylene using a metallocene catalyst. The chemical structure is presented in Figure 1. The ratio of both monomer types present in the final polymer defines the glass transition temperature. Different TOPAS grades with glass transition temperatures from 80°C to 180°C are commercially available. The increase in glass transition temperature with an increase of the norbornene content is presented in Figure 2.

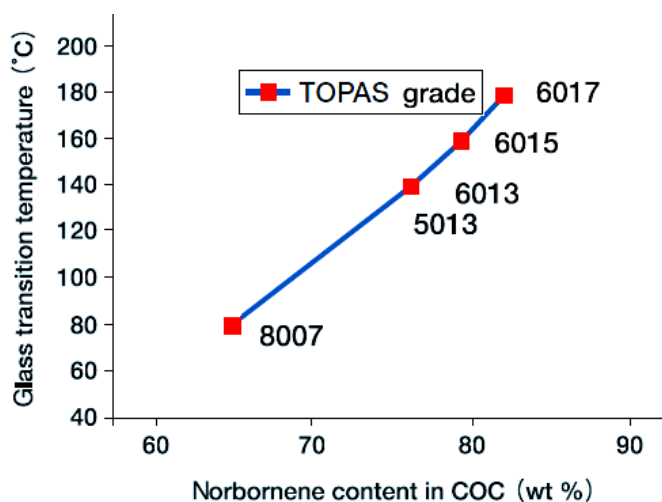


Figure 2: Dependency of the glass transition temperature of different TOPAS grades on the norbornene content [adapted from TOPAS Advanced Polymers]

2.2 Conducting polymers

The observation of an increased conductivity in an almost non-conducting polyacetylene film after exposure to halogen gas in 1977, renewed the interest to analyze and develop new conducting polymer systems [Gerard, 2002]. At that time Alan J. Heeger, Alan G. MacDiarmid, Hideki Shirakawa and co-workers exposed a polyacetylene film to oxidizing chlorine, bromine or iodine vapors causing a doping of the polymer film. The result was an increased conductivity by the factor of 10^7 [Shirakawa, 1977]. Today, doped polyacetylene films are still among the most conducting polymers with a specific conductivity of up to 10^5 S/cm^{-1} [Naarmann and Theophilou, 1987]. However, the degradability by oxygen in air prevented commercial application of polyacetylene widely [Kirchmeyer and Reuter, 2005].

Many efforts have been made to develop new conducting polymer types for commercial applications which combine properties like high conductivity, processability, and long term stability. Today, the commonly used candidates are polyaniline (PANI), polypyrrole (PPy), and polythiophene (PTh) [Gerard, 2002]. The basic chemical structures of these polymer classes are presented in Figure 3.

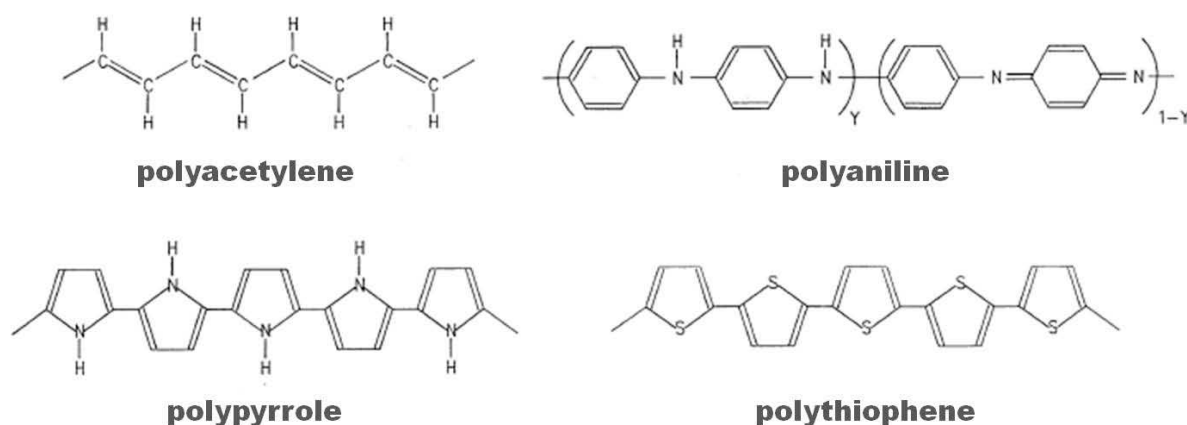


Figure 3: Chemical structure of common used conducting polymers [adapted from Gerard, 2002]

With the synthesis of poly(ethylenedioxythiophene) (PEDOT), Bayer Corporate Research laboratories developed a conducting polymer that meets industrial requirements. PEDOT which belongs to the group of polythiophenes is as all other conducting polymers only highly conductive in its doped state. Two types of PEDOT achieved highly commercial interest, PEDOT/TOS and PEDOT/PSS. They can be distinguished by the applied dopant [Kirchmeyer and Reuter, 2005].

PEDOT/TOS

PEDOT/TOS is an *in situ* polymerized PEDOT, doped with *p*-toluenesulfonate (tosylate, TOS). It is usually synthesized *in situ* during the manufacturing process. The monomer ethylenedioxythiophene (EDOT) is mixed with iron(III) tosylate and a pH stabilizer to control the reaction rate. The Fe^{3+} ion acts as oxidant for the polymerization of EDOT to PEDOT, the tosylate ions as dopant (Figure 4). Immediately after preparation, the polymerization solution has to be applied to a surface e.g. by spin coating. A following heating of the applied film (post-baking) evaporates remaining solvents and increases the polymerization rate. The polymerized film needs to be washed with de-ionized water or solvents to remove the oxidant, as well as excessive dopant [Kirchmeyer and Reuter, 2005].

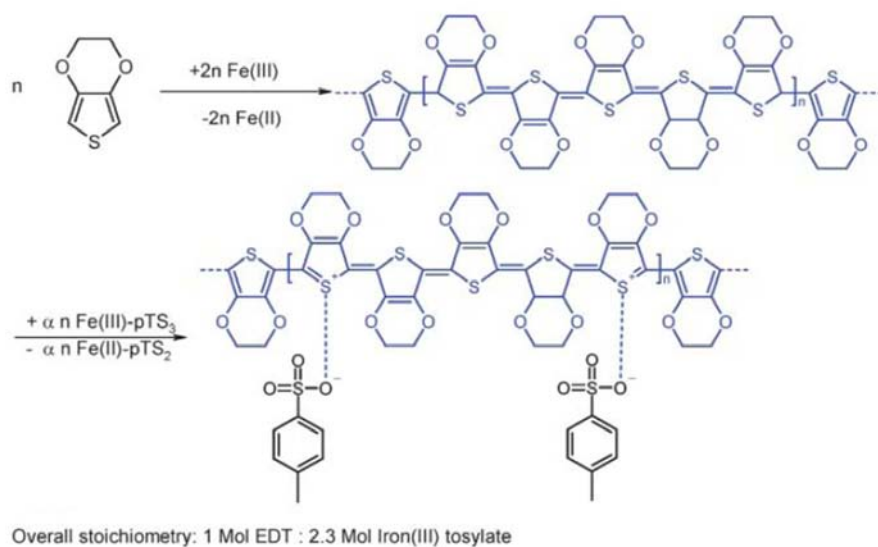


Figure 4: Oxidation of 3, 4-ethylenedioxythiophene (EDOT) with iron(III) tosylate. The first part represents the polymerization of EDOT, the second the doping of the poly(3, 4-ethylenedioxythiophene) with tosylate. [adapted from Kirchmeyer and Reuter, 2005]

Depending on the synthesis parameters PEDOT/TOS films with conductivities between 500 and 1000 S/cm can be obtained. Beside the high conductivity, the in situ polymerization allows an adjustment of the polymerization conditions to the manufacturing process e.g. by changing the viscosity of the polymerization solution through adding diluents. Furthermore, additional components can be added to the solution like mediators (e.g. prussian blue) which will be incorporated into the PEDOT film during the synthesis. The additives cause specificity of the PEDOT films which can be later used e.g. as sensor electrodes [Kirchmeyer and Reuter, 2005].

PEDOT/PSS

PEDOT/PSS commonly used for industrial purposes is a pre-polymerized PEDOT doped with polystyrene sulfonic acid (PSS). PEDOT/PSS is obtained from an aqueous dispersion of EDOT polymerized in the presence of PSS by using sodium peroxodisulfate as oxidant (Figure 5). The commercially available product is a dispersion of PEDOT/PSS complexes with excellent film-forming properties and is easy to process [Jonas and Heywang, 1994]. However, prepared films are basically an accumulation of PEDOT/PSS complexes which is the main reason for their reduced conductivity, compared to PEDOT/TOS. Films with conductivities of up to 10 S/cm [Groenendaal, 2000 (and included references)] have been obtained from PEDOT/PSS dispersions. [Kirchmeyer and Reuter, 2005]. The conductivity of

thin PEDOT/PSS film was increased by up to two orders of magnitude by adding solvents as well as a post-heat treatment. [Jönsson, 2003; Kim, 2011]. This is assumed to be based on a decreased complex size as well as a higher aggregation rate due to the removal of excess PSS by adding solvents [Yan and Okuzaki, 2009].

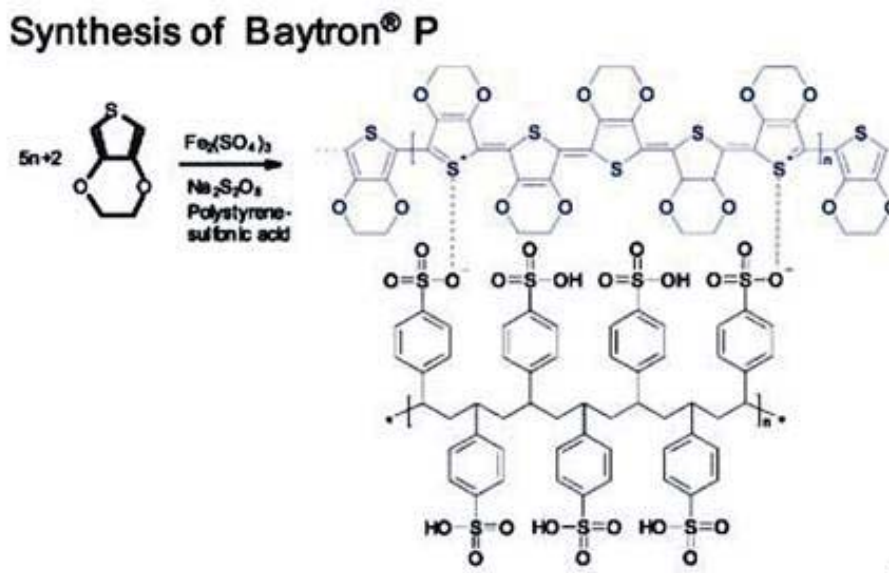


Figure 5: Polymerisation of PEDOT/PSS from an aqueous dispersion of EDOT presents of the dopant PSS by using sodium peroxodisulfate as oxidant [adapted from Kirchmeyer and Reuter, 2005]

2.3 References

- [Becker and Gärtner, 2000] Becker, H.; Gärtner, C. *Electrophoresis* **2000**, *21*, 12-26
- [Becker and Gärtner, 2008] Becker, H.; Gärtner, C. *Analytical and bioanalytical chemistry* **2008**, *390*, 89-111
- [Gerard, 2002] Gerard, M.; Chaubey, A.; Malhotra, B. D. *Biosensors & bioelectronics* **2002**, *17*, 345-59.
- [Groenendaal, 2000] Groenendaal, B. L.; Jonas, F.; Freitag, D.; Pielartzik, H.; Reynolds, J. R. *Development* **2000**, 481-494
- [IUPAC] IUPAC. *Compendium of Chemical Terminology*, 2nd ed. (the "Gold Book"). Compiled by A. D. McNaught

- and A. Wilkinson. Blackwell Scientific Publications, Oxford (1997). XML on-line corrected version: <http://goldbook.iupac.org> (2006-) created by M. Nic, J. Jirat, B. Kosata; updates compiled by A. Jenkins. ISBN 0-9678550-9-8. doi:10.1351/goldbook
- [Jonas and Heywang, 1994] Jonas, F.; Heywang, G. *Electrochimica Acta* **1994**, *39*, 1345-1347
- [Jönsson, 2003] Jönsson, S.; Birgersson, J.; Crispin, X.; Greczynski, G.; Osikowicz, W.; Denier van der Gon, A.; Salaneck, W.; Fahlman, M. *Synthetic Metals* **2003**, *139*, 1-10
- [Kim, 2011] Kim, Y. H.; Sachse, C.; Machala, M. L.; May, C.; Müller-Meskamp, L.; Leo, K. *Advanced Functional Materials* **2011**, *21*, 1076-1081
- [Kirchmeyer and Reuter, 2005] Kirchmeyer, S.; Reuter, K. *Journal of Materials Chemistry* **2005**, *15*, 2077
- [Naarmann and Theophilou, 1987] Naarmann, H.; Theophilou, N. *Synthetic Metals* **1987**, *22*, 1-8
- [Shin, 2005] Shin, J. Y.; Park, J. Y.; Liu, C.; He, J.; Kim, S. C. *Pure and Applied Chemistry* **2005**, *77*, 801-814
- [Shirakawa, 1977] Shirakawa, H.; Louis, E.; MacDiarmid, A.; Chiang, C.; Heeger, A. *Polymer* **1977**, 578-580.
- [TOPAS Advanced Polymers] [topas_brochure_product overview_english.pdf](http://www.topas.com/news-literature-brochures) available under: <http://www.topas.com/news-literature-brochures>
- [Yan and Okuzaki, 2009] Yan, H.; Okuzaki, H. *Synthetic Metals* **2009**, *159*, 2225-2228

Chapter 3

Microfabrication Methods

3.1 Micromachining

3.1.1 Introduction to Micromachining Processing

The systems presented at the end of this work (Chapter 5) are based on two basic micromachining operations: microdrilling and micromilling. Microdrilling was directly applied to fabricate circular- as well as tubular- electrodes (Chapter 5.1 and 5.2). This chapter covers only the basic technical principles. Detailed process descriptions can be found in the chapters where the corresponding electrode types are described.

Micromilling was applied to fabricate aluminum stamps which were used for hot embossing of the electrochemical system presented in Chapter 5.3. Due to predetermined system dimensions of below $100\ \mu\text{m}$ a fabrication strategy had to be developed to guaranty high accuracy of the milling process. Process optimization finally allowed the fabrication of feature dimensions down to $10\ \mu\text{m}$ in height using a standard desktop milling machine.

Microdrilling

A round hole is fabricated by rotation of a drilling tool / drill with usually two cutting edges which is moved parallel to the axis of rotation into the substrate (feed motion).

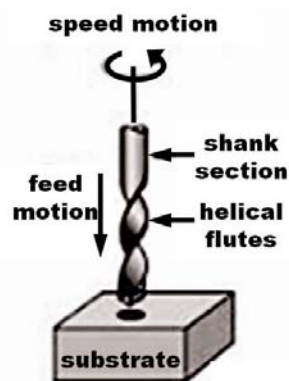


Figure 6: Principle of drilling process: rotating drilling tool creates a hole by penetration of the substrate in parallel direction to its axis of rotation. [adjusted picture originally from: Groover, 2010].

Micromilling

A plane or contoured surface is fabricated by using a rotating tool usually with two up to four cutting edges and a slow tool movement perpendicular to the tool's axis rotation (feed speed).

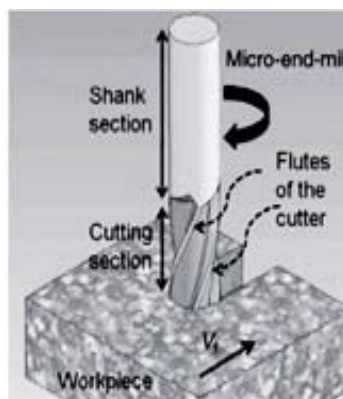


Figure 7: Principle of micromilling process: rotating milling tool consisting of shank and cutting section penetrates the substrate. Tool movement and therefore cutting direction is perpendicular to the tool's rotation axis. [picture: Koç and Özel, 2011]

The Cutting Tool

The cutting tool consists of shank and one or more flutes with cutting edges/teeth. The shank is the upper cylindrical part and used to fix the tool into the machine. The flutes are helical grooves at the lower end of the tool (Figure 8). The helical structure of the flutes (helix angle approx. 30° (Kyocera International, Inc.)) allows removal of material (swarf) by pulling it up the flute while the tool rotates. Continuous removal of swarf during the machining process avoids vibrations causing a higher accuracy as well as surface quality (surface finish). Furthermore the helices allow a (gradual) tool penetration into the substrate which would not be possible with straight flutes. [http://en.wikipedia.org/wiki/Milling_cutter]

The teeth (cutting edges) are sharp blades at the flute ends and responsible to remove the material from the substrate. A tooth divides the flutes into two surfaces: the rake and the flank face. The rake face is oriented at a certain angle (rake angle " α ") towards the cut material and directs the flow of the removed material (chip). The rake angle " α " is measured relative to the plane perpendicular to the work surface and can be positive or negative. The flank of the tool (backside of flute) provides a clearance between tool and newly formed surface and thereby protects the surface from abrasion which would degrade the surface finish. [Groover, 2010, http://en.wikipedia.org/wiki/Milling_cutter,]

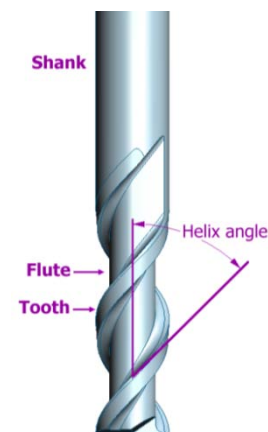


Figure 8: Illustration of a flat-end milling tool with shank and cutting section. The latter consists of helical flutes with cutting teeth at the ends. [picture obtained from: http://en.wikipedia.org/wiki/Milling_cutter]

Types of Cutters

A number of shapes of milling tools like flat-end or ball-nose end as well as drilling tools are commercially available. The choice of the right tool depends on the final structure as well as required final surface quality.

Flat-end mill



Flat-end mills have teeth at the flat tool face as well as at the periphery of the flutes. They are the most often used tools for vertical micro-milling operations and usually have between two and four teeth. An increased number of teeth increase the surface finish. [DORMER, http://en.wiki-pedia.org/wiki/Milling_cutter picture adapted from Kyocera].

Ball-end mill



Ball-end mills have, in contrast to flat-end mills a hemispherical end and are most often used for machining 3-D contoured shapes in moulds and dies. [http://en.wikipedia.org/wiki/Milling_cutter; picture adapted from Kyocera]

Microdrill



Most microdrills are made as twist drills. Two opposite cutting edges meet each other at the center of the end face. The meeting point is called “chisel edge”. Cutting takes place at the face end, flutes are responsible for swarf removal only. [Rai-Choudhury, 1997; http://en.wikipedia.org/wiki/Drill_bit picture adapted from Kyocera]

Cutting Conditions

A machining process is defined by feed speed (lateral movement across the substrate), cutting speed (mainly defined by the tool diameter and rotation) and depth of the cut (penetration of tool into substrate).

The most crucial parameter, especially for micromilling in metals, is the minimum undeformed chip thickness of removed material. It can be understood as a tool parameter which defines the lowest possible thickness of removed material (chip). By operating below this parameter, the tool is not able to removed material from the stock substrate

For macromilling the cutting edge of the tool can be assumed to be perfectly sharp and a chip is formed constantly during each cutting cycle since the chip thickness is usually much larger than the cutting edge radius of the tool [Chae, 2006]

For micromilling the assumption of a sharp tool is not valid since the cutting edge radius (“ r ”) becomes significant compared to the thickness of the removed material (“ h ”) (Figure 9). The undeformed chip thickness is typically comparable in size to the cutting edge radius [Aramcharoen, 2009]. If the ratio (undeformed chip thickness to cutting edge radius) is equal or less than 1 the effective rake angle (“ α ”) becomes negative. At negative rake angles (ratio <1) the material will be compressed and starts to flow. The material flowing into the axial direction of the tool will form burrs [Schaller, 1999; Lee, 2005; Bissacco, 2006]. A further decrease of the ratio leads to hardening of the material in front of the tool causing an increased tool wear and finally tool breakage. The minimum undeformed chip thickness is achieved when the ratio of undeformed chip thickness to the cutting edge radius is in the range from 0.1 to 0.4 [Yuan, 1996; Weule, 2001; Vogler, 2004, Malekian, 2011]

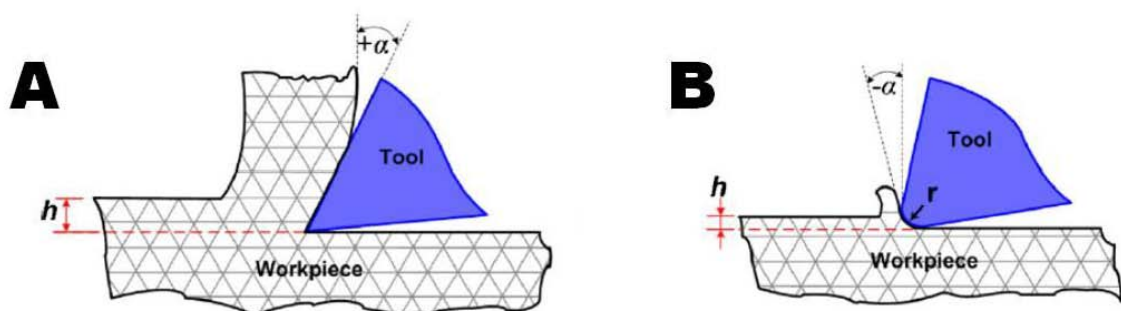


Figure 9: Schematic of the cutting edge in A) conventional macromilling and B) micromilling with the thickness of removed material (“ h ”), cutting edge radius (“ r ”), and effective rake angle (“ α ”) [adjusted from Aramcharoen, 2009]

Besides, it is suggested that the material becomes compressed if the chip thickness is lower than the minimum undeformed chip thickness. Compressed material is forced under the tool and recovers after the tool has passed (elastic deformation). No material will be removed during the tool passage. Elastic recovery of the material increases the surface roughness and therefore causes a poor surface finish [Filiz, 2007]. For a ratio (chip thickness to minimum undeformed chip thickness) equal to 1 only a part of the material will be removed. Shearing, deformation and recovery of the material cause a removal rate less than expected. For ratios above 1 (chip thickness larger than minimum undeformed chip thickness) the material is removed and a chip is formed with each tool passage (Figure 10). [Yuan, 1996; Chae, 2006]

Due to mentioned mechanisms, the cutting edge radius of the tool is the most critical parameter for the removal of material. It defines the minimum undeformed chip thickness which has a high impact on surface finish and feature accuracy [Weule, 2001, Özel, 2007, Malekian, 2011].

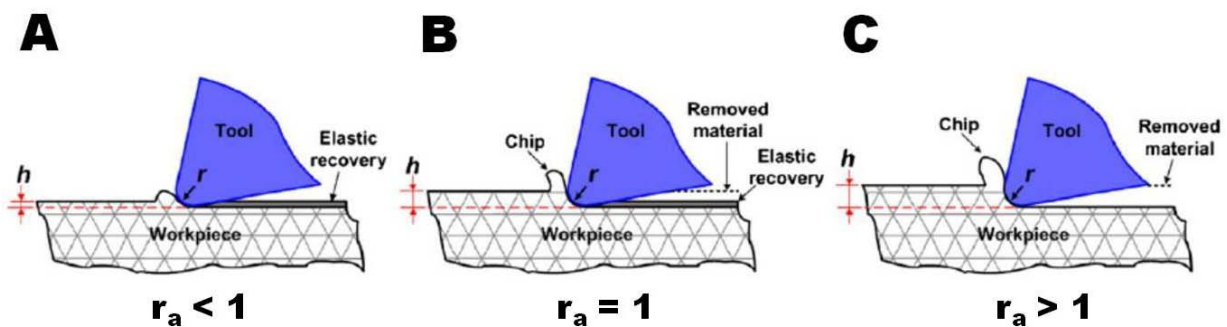


Figure 10: Chip formation relative to the minimum chip thickness in micromilling with the thickness of removed material (“ h ”), the ratio of chip thickness to minimum undeformed chip thickness (“ r_a ”), and the cutting edge radius (“ r ”) [adjusted from Aramcharoen, 2009]

3.1.2 Analyses of Milling Equipment

The following chapter presents initial analysis steps which were necessary to ensure a high surface finish as well as high feature quality. Imaging of cutting tools and methods to analyze the tool-substrate alignment are discussed as main points.

Initial Quality Control of New Microtools

To ensure a reproducible fabrication, tools were imaged using a scanning electron microscope (SEM) to analyze the initial conditions (Figure 11 A). Important parameters to evaluate were the diameter as well as the integrity of the tool. This was especially important, since tools were found to have a diameter of $\text{\O}30\ \mu\text{m}$ instead of $25\ \mu\text{m}$ as stated by the manufacturer (Figure 11 B). Broken teeth were found on new tools during imaging (Figure 11 C).

The application of dimensional wrong tools would result in wrong scaled features as well as dimensional irregularities. For example, application of tools with a too large diameter would cause cutting of already fabricated structures. Dull tools would cause a poor surface finish.

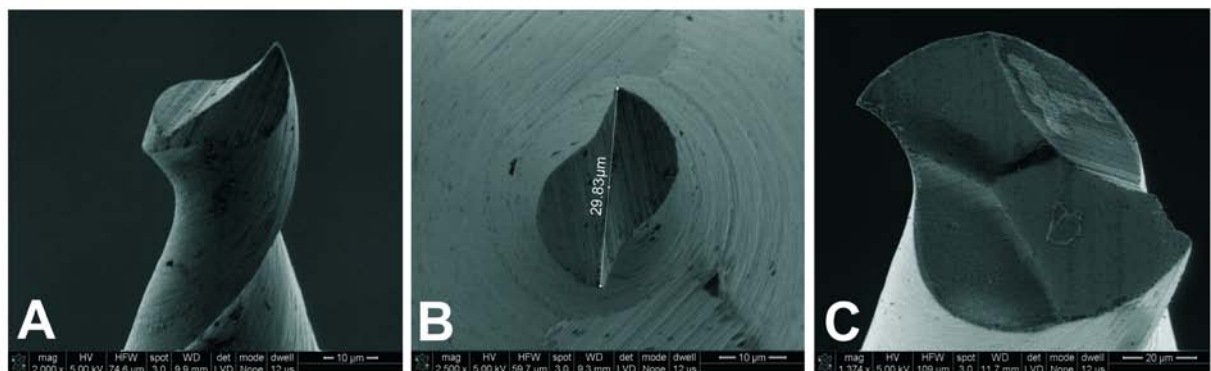


Figure 11: SEM images of (A) a new $\text{\O}30\ \mu\text{m}$ tool (30° tilted), (B) a $\text{\O}25\ \mu\text{m}$ flat-end mill, delivered with a diameter of approximately $30\ \mu\text{m}$ (top view), and (C) an unused $\text{\O}100\ \mu\text{m}$ flat-end mill with an already broken edge (45° tilted).

Tool-Substrate Alignment

For milling and drilling operations a desktop milling machine from Minitech (Minitech Mini-Mill/3PRO) was used (12 A). Aluminum samples were fixed to machine table using metal blocks which itself were screwed to the machine table. Blue clay was used to keep the coolant (water) in place (Figure 12 B).

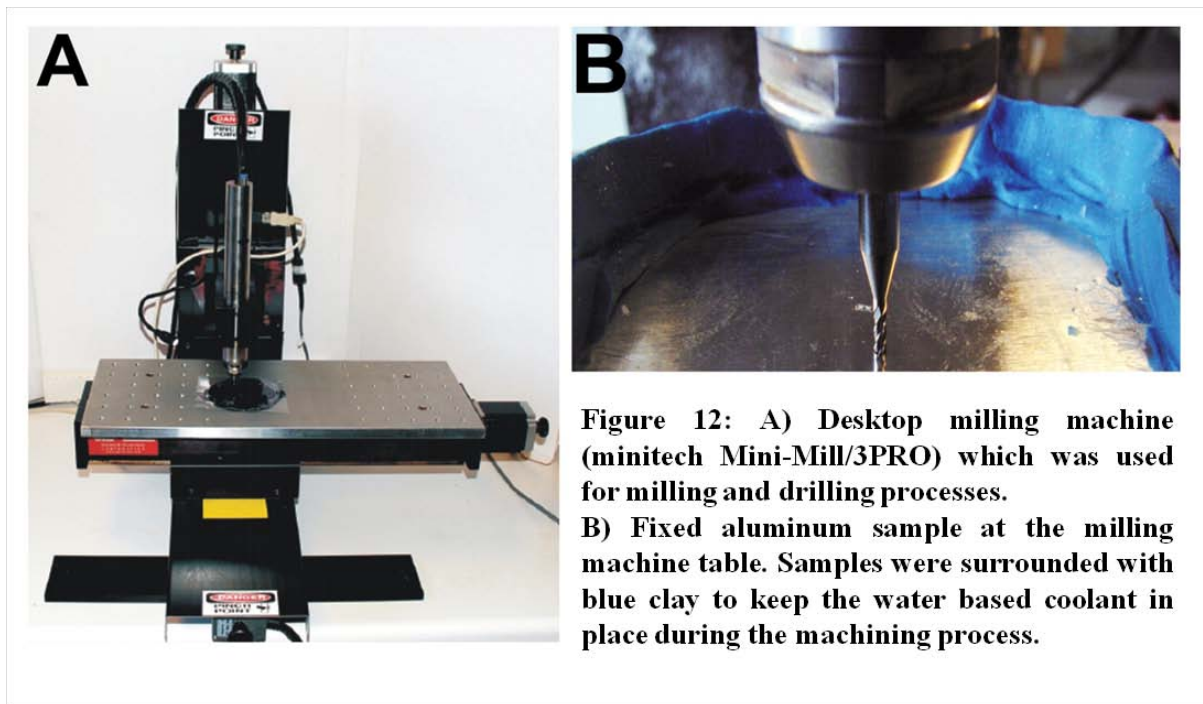


Figure 12: A) Desktop milling machine (minitech Mini-Mill/3PRO) which was used for milling and drilling processes. B) Fixed aluminum sample at the milling machine table. Samples were surrounded with blue clay to keep the water based coolant in place during the machining process.

The tool-sample alignment was analyzed by a stepwise lowering of a non-rotating tool down to surface contact. The exact contact point between tool and sample was determined by measuring the electrical resistance between tool and substrate (more precisely: between tool and a metal block used for clamping which was in electrical contact to the substrate) (figure 13). At the contact point, the electrical resistance dropped significantly from infinity ($> 40 \text{ MOhm}$) to some hundreds milliohm upon electrical contact between tool and aluminum sample. The tool was then manually rotated and lifted again. For sufficient tool-substrate alignments closed circles (Figure 14 A), for misalignments open circles at the substrate surface were observed (Figure 14 B).

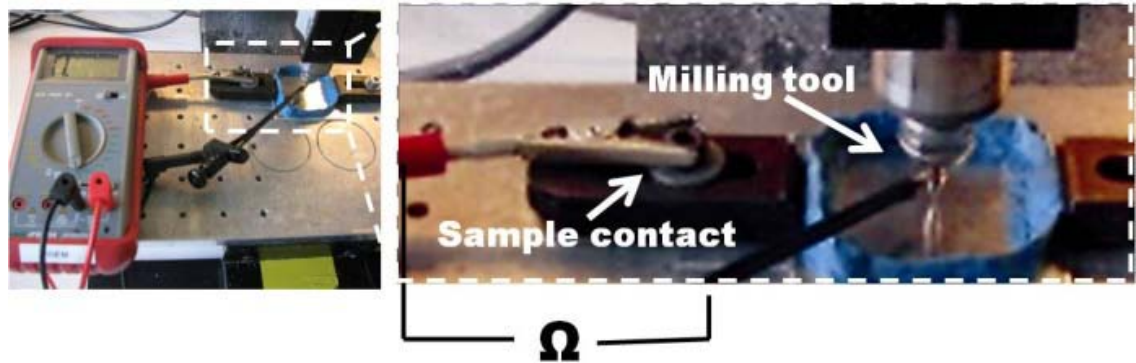


Figure 13: Leveling procedure: An aluminum sample (surrounded by blue clay) was mounted at the milling machine table. While measuring the electrical resistance between tool and the sample, the tool was stepwise lowered to the sample surface. At the contact point between tool and sample the electrical resistance dropped from infinity to some hundreds milliohm upon physical contact.

Misalignments could be caused by a tilted tool as well as tilted substrates or inhomogeneous surfaces. In case of repeated measurements distributed over the whole substrate resulted in:

- Identical circular pattern (incl. orientation) at different contact levels: The substrate was tilted and had to be aligned to the tool.
- Different circular patterns at the same level: The substrate surface was inhomogeneous and had to be exchanged.
- Identical pattern at the same contact level: The tool or spindle was tilted had to be aligned.

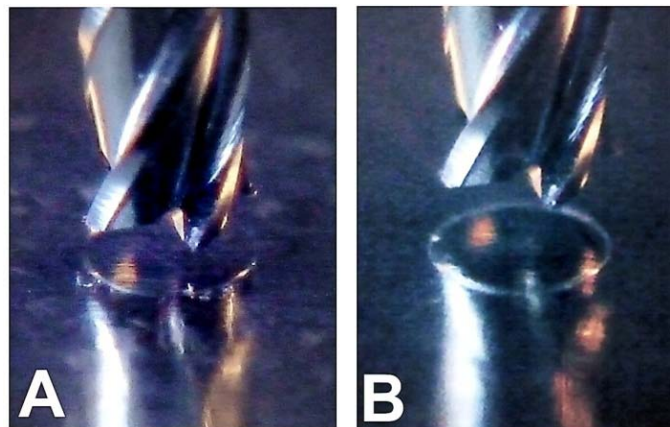


Figure 14: Ø3 mm, 4 flute flat-end mill above an aluminum surface after physical contact. At contact the tool was manually rotated and afterwards lifted. A) Open circles indicates bad, B) closed circles a good tool-surface alignment.

A good alignment was necessary to achieve a high surface finish as well as straight structures. Surfaces machined with a tilted tool showed a waved surface perpendicular to the milling direction. Due to the fact that one side of the tool was lower than the other, each tool track resulted in a tilted machined surface. Multiple tool tracks beside each other resulted in a waved surface finish (Figure 15). Structures, especially inverse channels, fabricated with a tilted tool showed distorted dimensions. This includes non-perpendicular sidewalls as well as non-horizontal top-planes (Figure 16). Depending on the grade of distortion and the following

application this is not necessarily a problem. However, in our case the fabricated structures were used for hot embossing and therefore a high precision and a low surface roughness was required. Distortions would reduce the stability of the structures and therefore increase the risk of deformation as well as breakage during hot embossing.

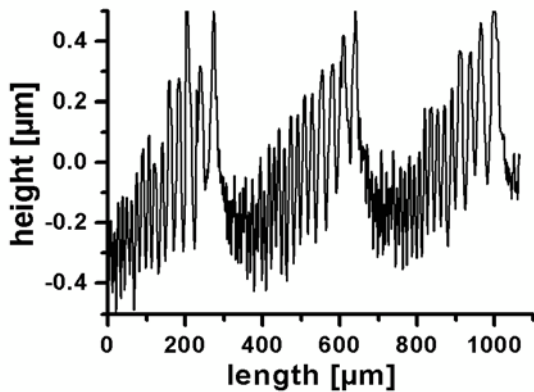


Figure 15: Profile of a machined aluminum surface. Presented are three milling tracks fabricated with a $\text{\O}1$ mm tool using an overlap of 0.7 mm of the tool diameter between the tracks (corresponding step distance: 300 μm).

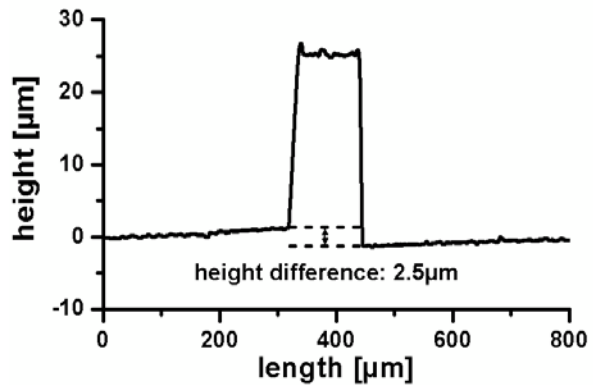


Figure 16: Example of a distorted inverse channel structure: A tilted tool caused a height difference between the left and right sidewall of about 2.5 μm .

Another important point is to ensure a precise tool change since it is not always possible to fabricate the entire feature with only one tool type. Electrical resistance controlled leveling allowed a tool change with a precision of about 1 μm especially important for the fabrication of structures in the low micrometer range (below 100 μm). Initial tool changes without electrical resistance control caused step heights of up to 10 μm between milled surfaces before and after tool change (Figure 17). For example, fabricated slopes, used for hot embossing experiments (Chapter 5.3.3), showed an initial step at the slope bottom which made PEDOT deformation studies impossible (Figure 17).

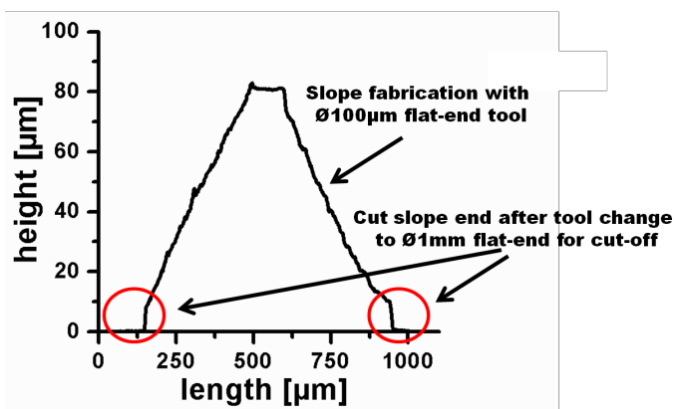


Figure 17: Fabricated ramp with two sloped side walls. Both slopes have an approximately 8 - 10 μm step at the start/end point caused by an unprecised tool change from a $\text{\O}100$ μm flat-end mill to a $\text{\O}1$ mm flat-end mill.

3.1.3 Optimization of Micromilling Parameters

A smooth surface is particularly important for following embossing experiments (Chapter 3.2). A high surface roughness increases the adhesion between polymer and stamp and can thereby cause release problems during demolding process. To achieve a good surface finish for fabricated stamps, the milling process parameters were optimized separately for planar and sloped surfaces.

3.1.3.1 Planar Surfaces

Optimized milling process parameters were required to fabricate stamps with a low surface roughness but also to achieve a high geometrical feature precision. Suboptimal process parameters lead to reduced quality e.g. imprecise feature dimensions or structural distortions.

Minimization of Surface Roughness

To achieve a low surface roughness, a speed test was realized by milling a 3 cm long line into an aluminum sample using cutting speeds from 32 m/min to 160 m/min. A cross variation of the feed speed from 10 mm/min to 50 mm/min resulted in corresponding chip thicknesses from 0.05 μm to 1.3 μm (tool: 4 flute, \varnothing 1 mm flat-end mill). Surface profiles were recorded with a “Dektak 8 stylus profiler”. The surface roughness was calculated with the internal profilometer software. To detect the influence of tool wear or material inhomogeneities on the resulting surface roughness, a line with a cutting speed of 80 m/min and a chip thickness of 0.2 μm was milled before and after each speed test as well as in between after every third line. Surface roughnesses obtained from milled lines at standard parameters were used to normalize all other surfaces roughnesses at each particular speed test. Therefore all roughness measurements are presented in comparison to the surface roughness achieved at standard parameters: cut speed: 80 m/min and chip thickness: 0.2 μm (Figure 18).

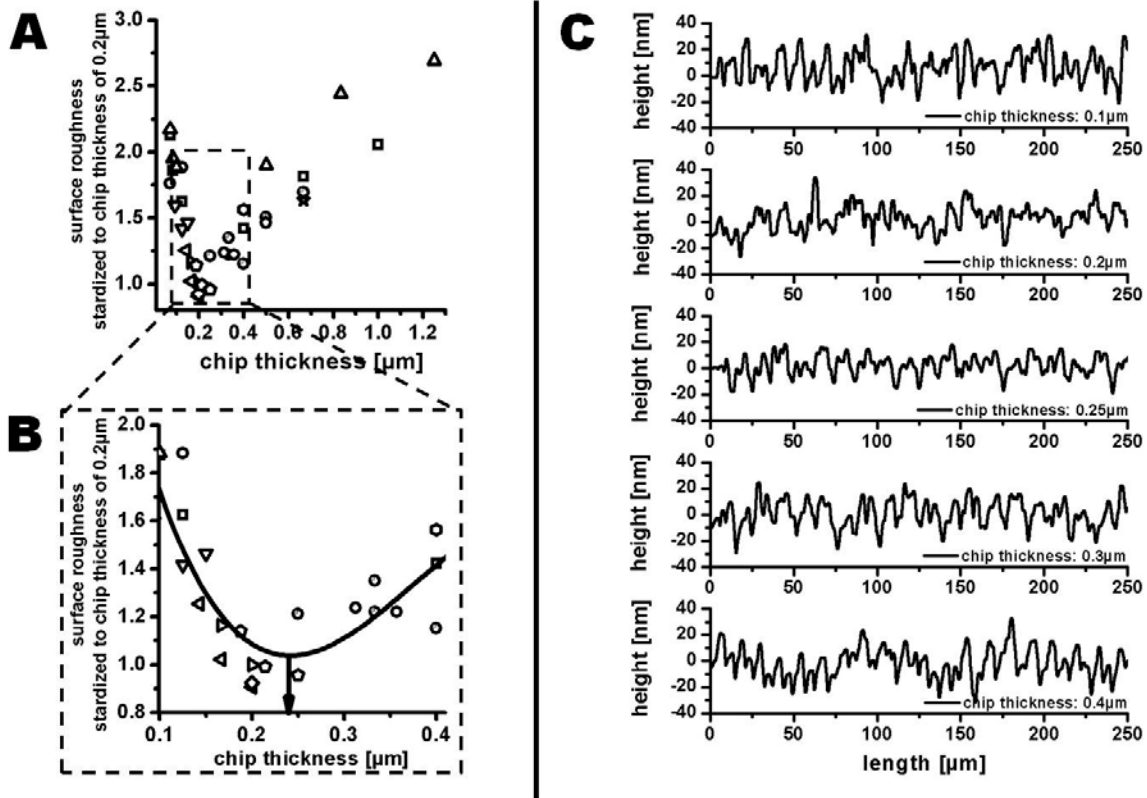


Figure 18: A) Surface roughnesses of three independent speed tests normalized to the surface roughness of a control, milled at 80m/min and a chip thickness of 0.2 μm after every third parameter change. Different symbols present independent speed tests. B) Magnification of A for a chip thickness range of 0.1 to 0.4 μm. C) Recorded surface profiles machined with parameter resulting in chip thickness from 0.1 to 0.4 μm.

A minimum in surface roughness was found for a chip thickness of 0.24 μm/tooth. An increase as well as a decrease of the chip thickness resulted in increased surface roughness (Figure 18 A and 18 B). The higher surface roughness at smaller chip thickness could be caused by the increasing dominance of elastic recovery as well as vibrations during operations below the minimum chip thickness. The higher surface roughness at larger chip thickness may be caused by an overload of the tool due to high material removal.

Figure 18 C shows profiles of aluminum surfaces machined with 0.1 μm/tooth up to 0.4 μm/tooth and visualize previous discussion. The most homogeneous surface was found for a material removal rate of 0.25 μm/tooth (theoretical minimum chip thickness: 0.24 μm). Vibrations as well as inhomogeneities are visible in profiles for surfaces treated with removal rates both smaller and larger than 0.25 μm/tooth.

Assuming a chip thickness of $0.24 \mu\text{m}/\text{tooth}$ is close to the minimum undeformed chip thickness, we can calculate the cutting edge radius of the tool using the ratio between minimum undeformed chip thickness to cutting edge radius of approximately 0.25 (average of [Yuan, 1996; Weule, 2001; Vogler, 2004, Malekian, 2011].). The resulting calculated cutting edge radius is approximately $1 \mu\text{m}$. An SEM image of a single tooth is shown in Figure 19 C. The inserted circle with a radius of $1.3 \mu\text{m}$ covers the tooth edge and supports the previous calculation.

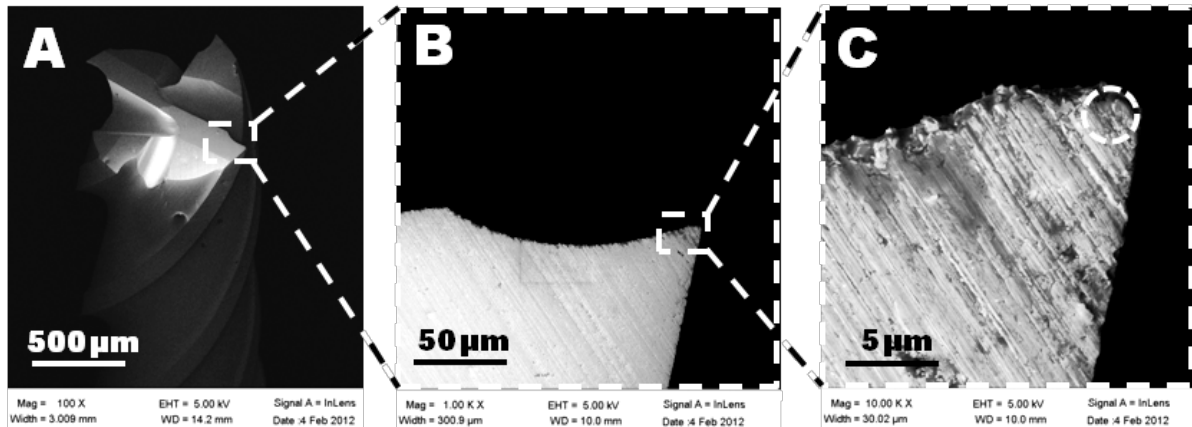


Figure 19: SEM images of A) a $\text{Ø}1 \text{ mm}$ four flute flat-end mill (30° tilted), B) a single cutting tooth (top view) and C) a cutting edge (top view). The inserted circle (radius of $1.3 \mu\text{m}$) at the cutting edge is aligned to the radius of the cutting edge.

Milling of inverse Channel Structures

Inverse channel structures were fabricated from aluminum plates using a $\text{Ø}1 \text{ mm}$ four flute flat-end mill with a feed rate of $0.25 \mu\text{m}/\text{tooth}$. Water was applied to the surface as coolant during milling. A modified profile of a $50 \mu\text{m}$ high and $100 \mu\text{m}$ wide inverted channel is presented in Figure 20.

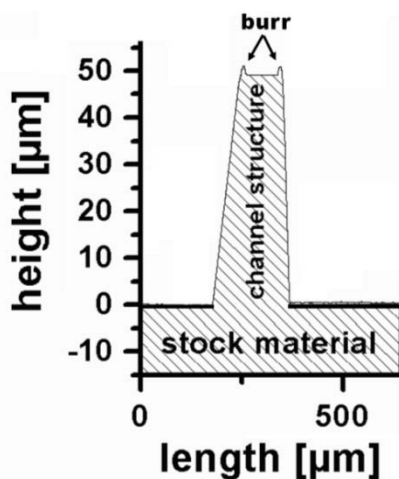


Figure 20: Modified profile of an inverse channel structure. For a better visualization the aluminum substrate was patterned.

The profile shows that the height of the fabricated structure is very precise. However, at both sides of the plateau remaining burrs from the fabrication process are visible. Burrs would lead to distortions in replicated structures of the following embossing experiments and therefore needed to be removed (chapter below). Furthermore, the two sidewalls of the inverse channel have different angles to the surface plane. A sufficient tool-substrate alignment was ensured before each milling process. To analyze if the tilted sidewalls in the profile are an artifact of the profilometric analysis or caused by the fabrication process, the channel structure was replicated in polydimethylsiloxane (PDMS) and imaged with an optical microscope (chapter next page).

Removal of Burrs

To remove the burrs at the plateau of the inverse channel structures, the machined samples were immersed two times for 15 min in a freshly prepared solution of phosphoric acid (H_3PO_4 , 85% in water), nitric acid (HNO_3 , 70% in water), and millipore water ($\geq 18 \text{ M}\Omega\text{cm}$) in a ratio of 74/3/23 (vol%) [MicroChemicals, 2009]. Hydrogen bubbles were constantly removed from the surface by ultrasonication. After each incubation the aluminum samples were rinsed thoroughly with deionised water. A profile of the structures was recorded before and after each etching step.

Complete profiles of the fabricated inverse channel structures before the etching step are presented in Figure 21 A. Burrs up to $6 \mu\text{m}$ in height are mainly placed at the left side of the plateaus. The profiles of the plateau after each etching step are presented in Figure 21 B and 21 C. The height of the burrs was significantly reduced already after 15 min etching (Figure 21 B). The second etching step of 15 min resulted in an almost complete removal of the burr (Figure 21 C).

Due to strongly increased feature quality, all subsequent fabricated samples were etched for 30 min before being further processed.

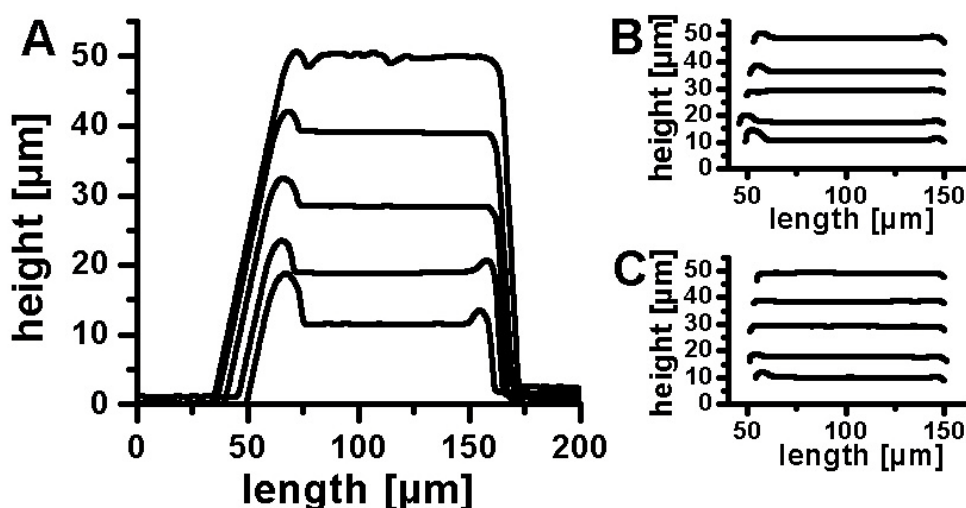


Figure 21: A) Profiles of inverse channel structures directly after machining, B) profiles of plateaus after 15min etching and C) after 30min etching. (B and C are the plateaus of same structures as presented in A)

Analysis of Sidewall Angles

A single profile of a channel structure after the etching process is presented in Figure 22 A, black trace. As observed in Figure 20, different sidewall angles are also visible in this profile. To determine the correct sidewall angle, a profile at the same spot after rotating the sample of 180° was recorded (Figure 22 A, red trace). The presented overlay shows that both scans have the same tilting for the “left” and the “right” sidewall even at opposite scan directions. Thus, the different sidewall angles are caused by the profilometer analysis (e.g. by a not vertically oriented stylus) and not by the milling operation.

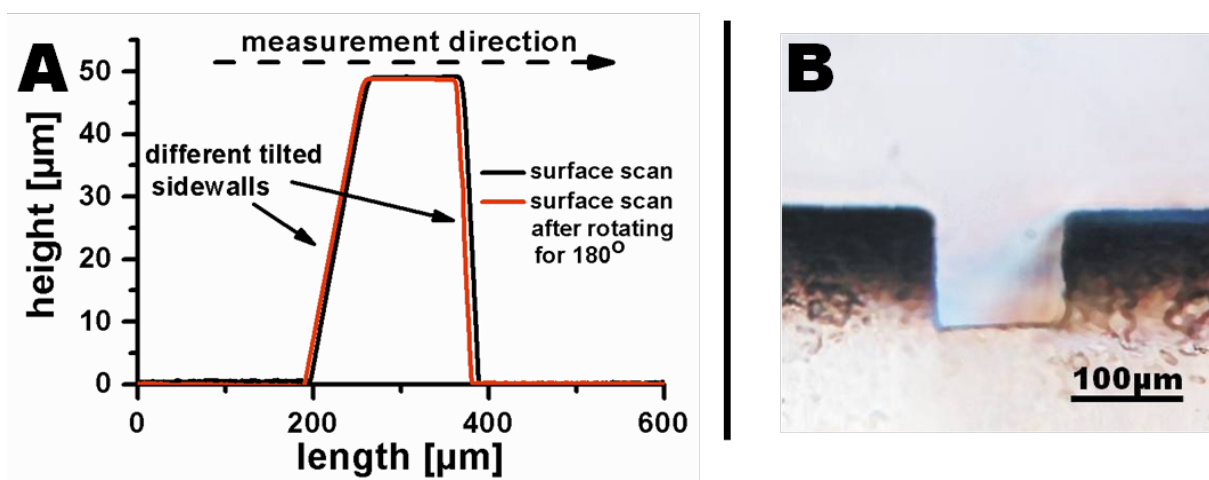


Figure 22: A) Overlay of profile scans of an inverse channel structure at the same spot before and after sample rotation of 180°. B) Cross section of inverse channel structure after replication in PDMS.

Chapter 3: Microfabrication Methods

To determine the correct sidewall angle, channel structures were replicated in polydimethylsiloxane (PDMS). After curing, the PDMS replica was cut across the channel and analyzed under a microscope. Figure 22 B shows a photograph of the channel cross section. The sidewalls are not completely vertical, but the PDMS replica shows that both sidewalls have slopes of close to 90° as expected, but not as observed by profilometry.

The right sidewall of the channel profile in Figure 22 A has an angle of 80° to the surface plane. This angle demonstrates the maximum capability of the profilometer to recognize any angle changes. The upper limit is probably based on the stylus geometry. Higher angles than 80° cause sterical hindrance and will not be detectable.

3.1.3.2 Sloped Surfaces

Milling of sloped surfaces was investigated to integrate the PEDOT electrodes into the final microfluidic system (Chapter 5.3). A milling procedure was developed to fabricate sloped surfaces of different angles to the surface plane in sufficient high quality. A good surface finish is particularly important in order to avoid fracture of the sub-micrometer thick PEDOT layer during the embossing process. Fractured PEDOT layers would cause inhomogeneous electrode areas.

Sloped surfaces can be fabricated using different tools:

- *Flat-End Mill*

Due to the sharp cutting edge perpendicular to the tool face a low surface roughness is most probably only possible by stepping down in the single micrometers. The advantage of a flat-end mill application is that the entire microfluidic system (slopes for electrodes as well as channel structure) can be produced without tool change. Thereby the risk of defects or misalignment in the structure can be reduced.

- *Ball Mill*

Using the hemispherical end of a ball mill for slope fabrication could result in a high surface quality of the sloped areas. Larger step sizes could be possible which would reduce the fabrication time. Ball mills down to $\text{Ø}100\ \mu\text{m}$ in diameter are commercially available.

- *Customized Tool with a defined Tapered Flute Angle*

Since these tools own a tapered flute, slopes can be easily fabricated by milling along the sidewall. However, only small angles from 1° to 5° are commercially available. Tools with larger angles can be produced on request but angles up to 30° or 45° are only possible to fabricate for tool diameters of about 2 mm. Application of a $\text{Ø}2\ \text{mm}$ tool for fabrication of a $100\ \mu\text{m}$ high slope increases the risk of inhomogeneities and poor surface quality.

Fabrication of Slopes using a Flat-End Mill

In order to achieve a high surface quality at sloped surfaces the influence of cutting speed (at a fixed feed rate) and step size in height were investigated separately. All experiments were carried out using a $\varnothing 100\ \mu\text{m}$, 2 flute flat-end mill. The influence of cutting speeds in the range of 0.3 m/min to 9.4 m/min was investigated at feed rates from $5\ \mu\text{m}/\text{tooth}$ down to $0.17\ \mu\text{m}/\text{tooth}$, respectively, using a constant step size in height of $4\ \mu\text{m}$. The influence of the height step size was analyzed in the range of $1\ \mu\text{m}$ to $5\ \mu\text{m}$ in $1\ \mu\text{m}$ steps using a cut speed of 3.14 m/min and a feed rate of $0.5\ \mu\text{m}/\text{tooth}$. The influence of cut speed as well as step size was investigated on slopes with angles of 30° and 50° to the surface plane.

Cutting Speed

No influence of the cutting speed on the slope quality was found in the analyzed range from 0.3 m/min to 9.4 m/min and feed rates of $5\ \mu\text{m}/\text{tooth}$ down to $0.17\ \mu\text{m}/\text{tooth}$. All 30° slopes were similar, the same for all 50° slopes. A significant difference was found between 30° and 50° sloped surfaces. 50° slopes showed a much smoother surface than 30° slopes (Figure 23). This can be explained by the lateral movement of the tool during milling. A 30° slope at given height steps of $4\ \mu\text{m}$ results in much larger lateral movement than for a 50° slope.

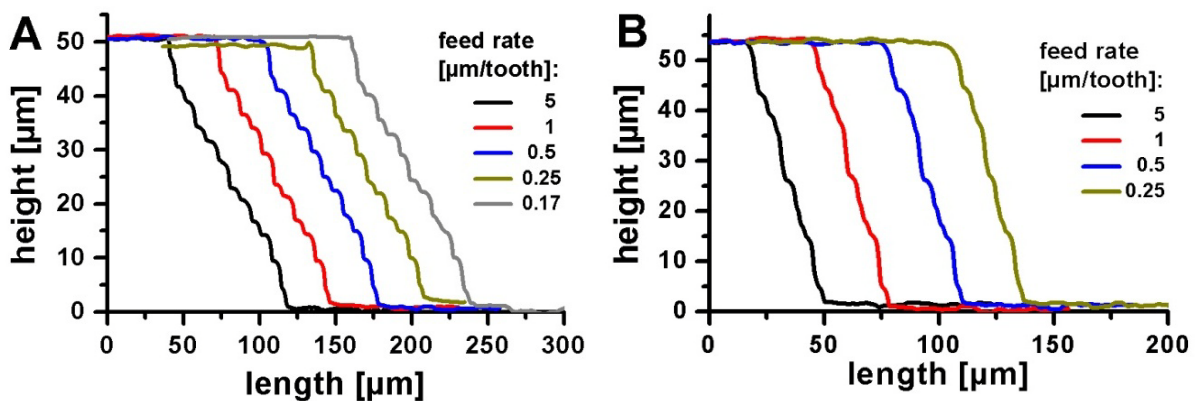


Figure 23: Profiles of $50\ \mu\text{m}$ high slopes fabricated at feed rates reaching from $0.17\ \mu\text{m}/\text{tooth}$ to $5\ \mu\text{m}/\text{tooth}$ using a $\varnothing 100\ \mu\text{m}$, two flute flat-end mill with angles of A) 30° and B) 50° to the surface plane

Step Size Variation

Profiles of slopes fabricated at different step sizes with angles of 30° or 50° to the surface plane are presented in Figure 24. The surface quality for 30° slopes decreased with increasing step size (Figure 24 A). Tool tracks for each single step were visible for step sizes larger than 3 μm. For step sizes of 1 μm and 2 μm no significant difference was observed. Slopes with an angle of 50° to the surface plane were mainly independent of the step size in the analyzed range (Figure 24 B). That indicates that step sizes in the single micrometer range are especially important for low angled slopes.

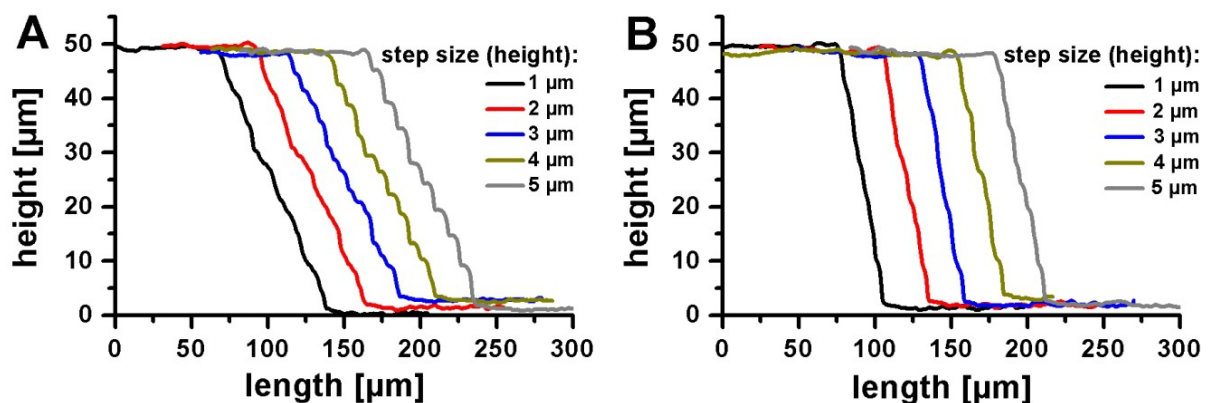


Figure 24: Profiles of 50 μm high slopes fabricated with step sizes in height of 1 μm to 5 μm using a Ø100 μm 2 flute flat-end mill with angles of A) 30° and B) 50° to the surface plane

Fabrication of Slopes using a Ball-End Mill

Slopes with angles of 30° and 50° to the surface plane were fabricated using a Ø100 μm ball-end mill at a cut speed of 3.14 m/min and a feed rate of 0.5 μm/tooth. As shown for the slope fabrication using a flat-end mill, the step size has the main impact on the slope fabrication. Step sizes in height from 1 to 5 μm were investigated.

All fabricated slopes possess a very high surface quality (Figure 25). Therefore a Ø100 μm ball-end mill is well suited for slope fabrication. However all vertical planes were very rough. Single tool tracks were visible caused by the hemispherical end of the ball mill. In case ball-end mills are used for slope fabrication, vertical planes need to be polished with a flat-end mill. The necessary tool change would expand the fabrication cycle and increase the risk of misalignments in all operational directions (x,y,z).

Besides, the hemispherical end of the ball-end mill caused round corners especially at the bottom of the slope. This might be acceptable for the applied tool diameter of 100 μm (corner radius = 50 μm) and low slope angles. However, the higher the slope angles the stronger the influence of the hemispherical end of the tool. Some tool producing companies like Kyocera

suggest not to use or even to avoid $\text{Ø}100\ \mu\text{m}$ ball-end mills since the tool diameter of fabricated tools are irregular and the tool itself eventually unstable. Kyocera finally stopped the fabrication of $\text{Ø}100\ \mu\text{m}$ ball-end mills. Application of a $\text{Ø}200\ \mu\text{m}$ ball-end mill as suggested would increase the corner radius to $100\ \mu\text{m}$ and therefore ball-end mills would not be suitable for fabrication of $50\ \mu\text{m}$ high slopes.

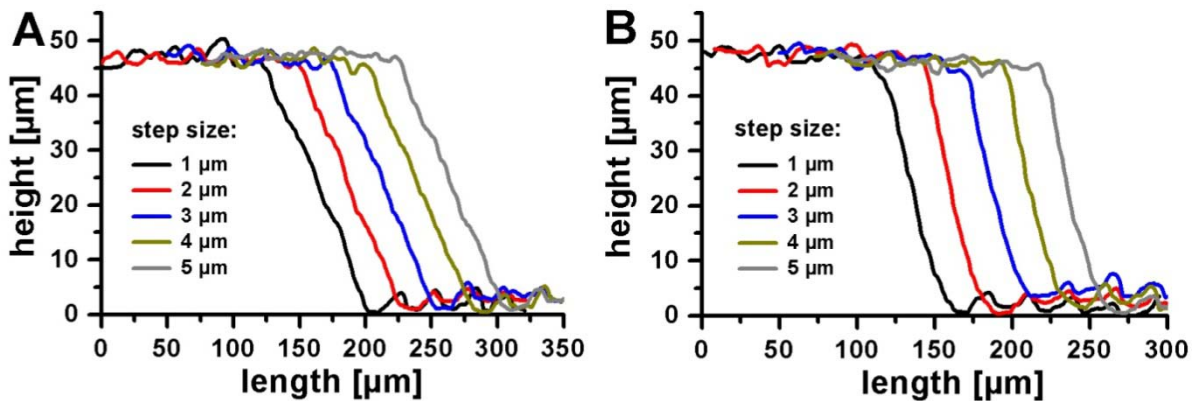


Figure 25: Profiles of $50\ \mu\text{m}$ high slopes fabricated with step sizes in height of 1 to $5\ \mu\text{m}$ using a $\text{Ø}100\ \mu\text{m}$ 2 flute ball-end mill with angles of A) 30° and B) 50° to the surface plane

Fabrication of Slopes using a Customized Tool

Slopes were fabricated using a $\text{Ø}2\ \text{mm}$ custom made flat-end mill with a tapered flute of 45° at the bottom (obtained from Kyocera). In order to achieve a high surface quality different cutting speeds from $6.3\ \text{m/min}$ to $188.4\ \text{m/min}$ at feed rates from $5\ \mu\text{m/tooth}$ down to $0.17\ \mu\text{m/tooth}$ were analyzed. The recorded profiles of fabricated slopes are presented in Figure 26.

Slopes fabricated using a feed rate of $5\ \mu\text{m/tooth}$ (cut speed: $6.3\ \text{m/min}$) showed a very good surface quality. A decreasing feed rate decreased the surface quality (Figure 26). An increased amount of inhomogeneities at smaller feed rates can be explained by operating below the minimum undeformed chip thickness. Even though a high surface quality was achieved at high feed rates all slopes had a non-linear slope bottom/round slope end. This is most likely caused by a dull edge at the tool face or by irregularities in the tool geometry.

Custom made tools for fabrication of slopes were not further investigated. The non-linear geometry of fabricated slopes, the comparable large tool diameter ($\text{\O}2$ mm tool compared to a $100\ \mu\text{m}$ slope), and the fact that for every demanded slope angle a new tool had to be designed and fabricated (minimum request amount 25 pieces) made custom made tools inappropriate.

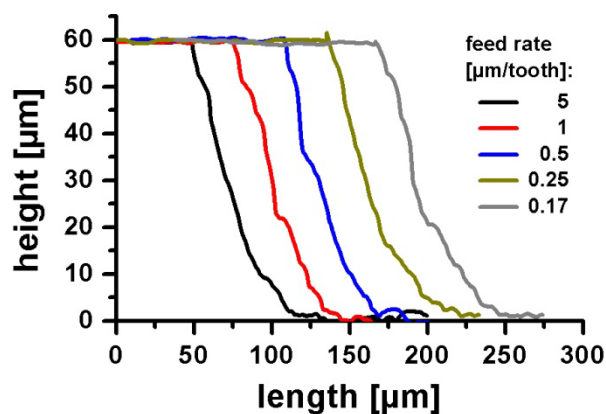


Figure 26: Profiles of $60\ \mu\text{m}$ high slopes fabricated at feed rates from $0.17\ \mu\text{m}/\text{tooth}$ to $5\ \mu\text{m}/\text{tooth}$ using a $\text{\O}2$ mm, 2 flute, 45° tapered flat-end mill with angles of A) 30° and B) 50° to the surface plane

Summary of Slope Fabrication

Slope fabrication is possible with all three types of milling tools. However, the application of a flat-end milling tool allows the fabrication of sloped as well as vertical surfaces with only one tool. Even though the quality at the sloped surfaces machined with a ball-end mill is better, the surface finish at horizontal planes is unacceptable. A tool change at these surfaces is especially critical, since the base level is not clearly defined. By using for example the resistant controlled leveling (described above) it would not be possible to define the base level since the electrical resistance would already drop upon contact with the top parts of the rough surface. Initial experiments with custom made tapered tools were not promising as well. Therefore, slopes for PEDOT deformability study were fabricated using a $\text{\O}100\ \mu\text{m}$ flat-end mill.

3.1.4 Stamp Fabrication for Hot Embossing

To fabricate stamps for hot embossing experiments (Chapter 3.2), circular stamps of 50 mm in diameter were cut out of an aluminum plate. Two different types of fabricated stamps are discussed in this chapter:

- Stamps presenting inverse channel structures of different heights for PEDOT disconnection study (Chapter 5.3.2) as well as for embossing the microfluidic system.
- Stamps presenting different slopes for PEDOT deformation studies (Chapter 5.3.3) as well as for integration of electrodes into the channel sidewalls of the final electrochemical system.

All stamps were characterized by profilometry as well as optical microscopy after replication in PDMS

Fabrication of an Inverse Channel Structures

Ten inverse channel structures from 50 μm up to 400 μm in width and 10 to 50 μm (10 μm steps) in height were milled out of a 2 mm thick aluminum substrate. A $\text{\O}1$ mm four flute flat-end mill at a feed rate of 0.25 $\mu\text{m}/\text{tooth}$ was used for all channel structures. They were arranged in two rows, each with five channels (Figure 27 A). At both sides, channel structures ended in a large connection platform (Figure 27 B). These platforms formed the mechanical support of channel structures during milling as well as embossing, and were used as connection points for electrical resistance measurements to characterize PEDOT disconnection across the sidewall (Chapter 5.3.2).

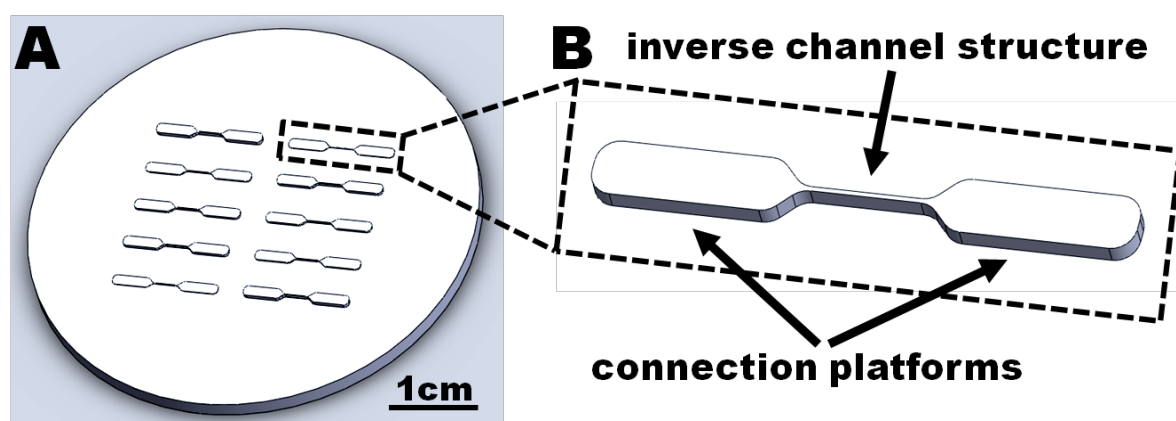


Figure 27: A) Model of a $\text{\O}50$ mm stamp carrying ten inverse channel structures aligned in two rows with each five inverse channels. B) Magnification of a single inverse channel structure: the channel is placed between two connection platforms.

Analysis of Inverse Channel Structures

Profiles of fabricated inverse channel structures from 50 to 400 μm in width and 10 to 50 μm in height are presented in Figure 28. For PEDOT disconnection studies it was crucial to achieve a predetermined height within a tolerance of $\leq 5 \mu\text{m}$. The profiles demonstrate the successful fabrication of the inverse channel structures. Except for one structure (Figure 28 C – height of 60 μm instead of 50 μm), all fabricated structures were within the five micrometer deviation of the predefined height.

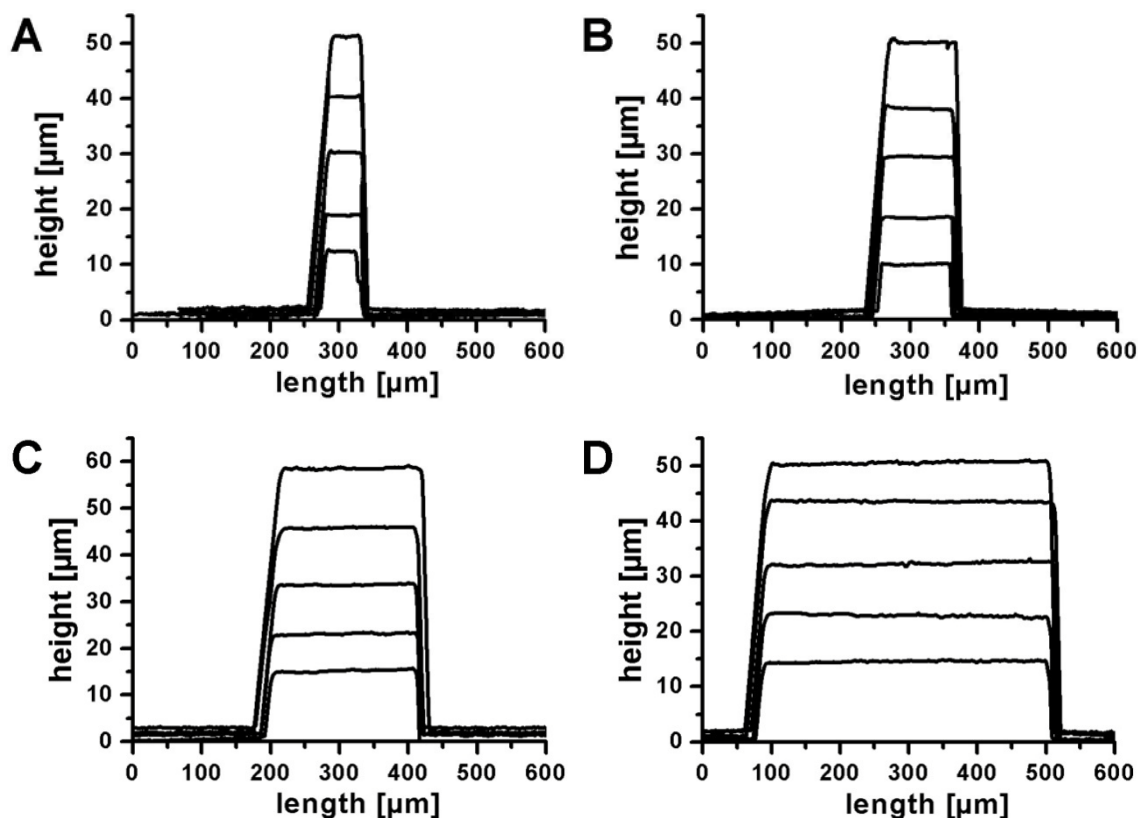


Figure 28: Profilometry traces across milled inverse channel structures from 50 to 400 μm in width and 10 to 50 μm in height.

Fabrication of Sloped Surfaces

A stamp with inverse channel structures and angled sloped surfaces was fabricated using a $\text{Ø}100\ \mu\text{m}$ flat-end mill. According to the process optimization a cut speed of 3.1 m/min and a feed rate of $0.5\ \mu\text{m}/\text{tooth}$ were used. A step size in height of $1\ \mu\text{m}$ was applied. Sloped surfaces were angled from 15° to 60° to the surface plane. The basic structures were designed and arranged as the inverse channel structures. Slopes were placed at both sides of the inverse channels (Figure 29). The design was chosen since it is very similar to the final sensor design. Thus, obtained results during embossing experiments are directly applicable for the sensor fabrication.

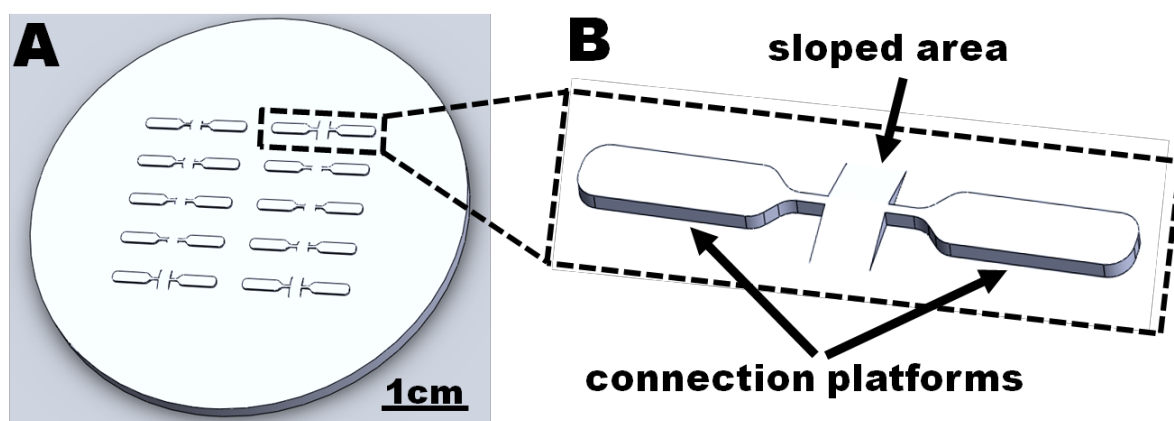


Figure 29: A) Model of a $\text{Ø}50\ \text{mm}$ stamp carrying ten inverse channel structures with angled slopes at the center. B) Magnification of a single inverse channel structure with corresponding slope: the channel with the slope is placed between two connection platforms.

Analysis of Sloped Surfaces

Profiles of the slopes are presented in Figure 30, left (solid lines). The inserted dotted lines indicate the predefined slope angle. A comparison of the inserted perfect slope angles with the recorded profiles shows that all fabricated slopes own the right angles ($\pm 3^\circ$). Except for the 15° slope all surfaces were fabricated with a very good surface finish. The 15° tilted surface showed small irregularities of maximum $3\ \mu\text{m}$ in height which was accepted for following embossing experiments.

To verify the recorded profiles, slopes were replicated in PDMS and visualized using an optical microscope (Figure 30, right). The analysis of the dimensions resulted in good agreement with the surface scans of the profilometer.

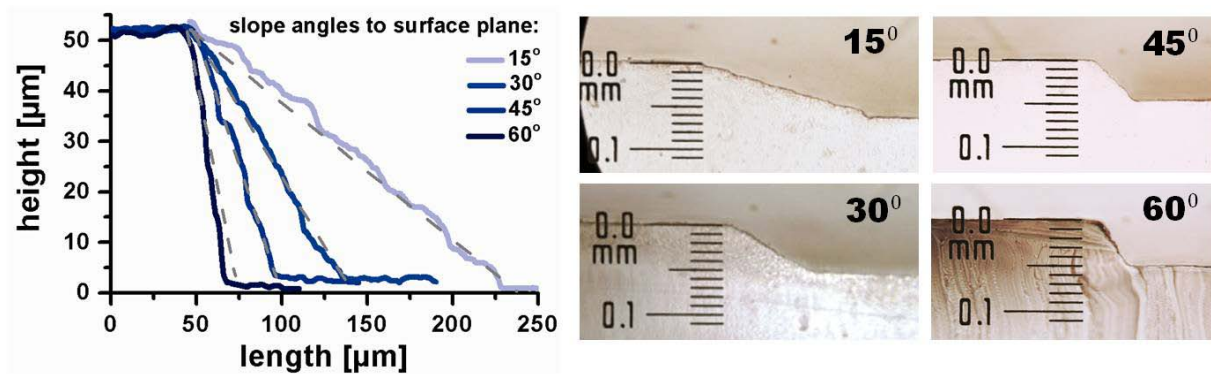


Figure 30: left: Profiles of 50 μm high slopes fabricated with a step size in height of 1 μm using a $\text{Ø}100 \mu\text{m}$ 2 flute flat-end mill with angles of 15° (light blue) up to 60° (dark blue) to the surface plane. B) Cross section of sloped surfaces after replication in PDMS

3.1.5 References

- [Aramcharoen, 2009] Aramcharoen, A.; Mativenga, P. T. *Precision Engineering* **2009**, 33, 402-407
- [Bissacco, 2006] Bissacco, G.; Hansen, H. N.; De Chiffre, L. *CIRP Annals - Manufacturing Technology* **2006**, 55, 593-596
- [Chae, 2006] Chae, J.; Park, S.; Freiheit, T. *International Journal of Machine Tools and Manufacture* **2006**, 46, 313-332
- [Dormer] www.knucklebusterinc.com/features/wp-content/2011/10/Milling_101.pdf
- [Filiz, 2007] Filiz, S.; Conley, C. M.; Wasserman, M. B.; Ozdoganlar, O. B. *International Journal of Machine Tools and Manufacture* **2007**, 47, 1088-1100
- [Groover, 2010] Groover, M. P.; *John Wiley & Sons, Inc.*; Fundamentals of Modern Manufacturing: Materials, Processes, and Systems; chapter 21; **2010**; ISBN: 978-0-470-46700-8
- [Koç and Özel, 2011] Koç, M.; Özel, T.; *John Wiley & Sons, Inc.*; Micro-Manufacturing: Design and Manufacturing of Micro-Products - Chapter 8; **2011**; ISBN: 978-0-470-55644-3

Chapter 3: Microfabrication Methods

- [Kyocera] Kyocera International, Inc; <http://www.kyoceramicrotools.com/>
- [Lee, 2005] Lee, K.; Dornfeld, D. *Precision Engineering* **2005**, 29, 246-252
- [Malekian, 2011] Malekian, M.; Mostofa, M. G.; Park, S. S.; Jun, M. B. G. *Journal of Materials Processing Technology* **2011**, 212, 553-559
- [MicroChemicals; 2009] MicroChemicals; www.microchemicals.eu/technical_information/aluminium_etching.pdf; **2009**
- [Özel, 2007] Özel, T.; Liu, X.; Dhanorker, A. *Rutgers-Department of Industrial and Systems Engineering* **2007**
- [Rai-Choudhury, 1997] Rai-Choudhury, P.; *SPIE Press*; Handbook of Microlithography, Micromachining, and Microfabrication, **1997**; ISBN: 978-0819423795
- [Schaller, 1999] Schaller, T.; Bohn, L.; Mayer, J.; Schubert, K. *Precision Engineering* **1999**, 23, 229-235
- [Smid, 1999] Smid, P.; *Industrial Press*; CNC programming handbook (2nd edition), **2003**, chapter 26, ISBN 9780831131586
- [Sutherland] <http://www.mfg.mtu.edu/marc/primers/milling/>
- [Vogler, 2004] Vogler, M. P.; DeVor, R. E.; Kapoor, S. G. *Journal of Manufacturing Science and Engineering* **2004**, 126, 685
- [Weule, 2001] Weule, H.; Hüntrup, V.; Tritschler, H. *Cirp Annals* **2001**, 50, 61-65
- [Yuan, 1996] Yuan, Z.; Zhou, M.; Dong, S. *Journal of Materials Processing Technology* **1996**, 62, 327-330

3.2 Hot Embossing

In hot embossing, a hot stamp presenting an inverse relief of the desired structures is pressed into a thermoplastic substrate. Stamp and polymer are usually heated above glass transition temperature of the polymer to allow a sufficient polymer flow. After cooling and demolding of the polymer from the stamp, the polymer presents the structures at the surface. A fast and repeatable replication of the stamp into polymer substrates makes hot embossing to a low cost, mass production strategy. Today, hot embossing is widely used for the fabrication of microfluidic systems [Qi, 2002; Pemg, 2009; Goral, 2011; Jena, 2011; Liedert, 2012]. However, the separation of stamp and polymer as well as the reutilization of the stamp causes limitations regarding materials and structure geometry. The main limitations are [Becker and Gärtner, 2000; Becker and Gärtner, 2008]:

- The stamp material has to be stable within the temperature and pressure range
- Features with undercuts are difficult to replicate since the stamp and the molded polymer need to be separated after embossing process
- Stamp and substrate have to be chemically inert to each other. A formation of chemical bonds between stamp and substrate during the molding step would prohibit separation.

Hot embossing can be realized in three different ways: cylinder to cylinder (often also referred as roll-to-roll embossing), cylinder against flat area and flat area against flat area embossing. In research, flat against flat area embossing is the most commonly used technique since it comprises advantages like easier fabrication of a stamp (large variety of processes are available for wafer as well as plane surface structuring) and the application of standard pressure-controlled presses with heated embosses (Figure 31) [Worgull, 2009].

3.2.1 The Hot Embossing Process

Commonly, the hot embossing process takes between 5 and 15 minutes and can be divided into four major steps [Becker and Gärtner, 2000; Becker and Gärtner, 2008, Worgull, 2009]:

(Pre-)Heating

The stamp is usually mounted to the upper, the polymer sample to the lower heating stage of the embossing press. Before the actual molding starts, both stamp and polymer are heated to molding temperature. The molding temperature is usually above glass transition temperature (T_g) of the polymer substrate. Heating is possible with an open or a closed mold. In case of a closed mold a touch force of only some hundred Newton will be applied. The low pressure ensures a gentle contact between mold and sample and allows heat transfer into the polymer sample from both sides. This causes a homogenous heat distribution within the polymer.

Isothermal Molding

At molding temperature the heating plates are moved towards each other (speed approximately 1 mm/min) until a predefined molding pressure is achieved (displacement-controlled process). The molding pressure as well as temperature is kept constant for a defined holding time (pressure-controlled process). Under optimal conditions, the polymer flows into small cavities as well as in the radial direction. To generate a constant pressure, the relative movement between the stamp and substrate has to be controlled and adjusted. Depending on the structure design, vacuum is required to avoid air and water entrapment in small cavities which would cause an incomplete filling. Water can be driven out of the polymer by applying heat and pressure. Typical embossing pressures are in the range of 0.5 - 2 kN/cm² [Becker and Gärtner, 2008].

Cooling

After a certain holding time, tool and substrate are cooled down to demolding temperature while the pressure is maintained. The demolding temperature needs to be below the glass transition temperature (T_g) of the polymer in order to achieve solidification and to avoid deformation of the features during separation. It is important to maintain the pressure during cooling in order to reduce shrinkage effects (see the demolding section).

Demolding

At the demolding temperature, the polymer with the desired features is separated from the stamp by a relative movement between stamp and polymer. Demolding is the most critical step of the entire embossing process since the highest forces act on the molded microstructures. Two sources of demolding forces influence the final quality of the molded features: a) the friction force caused by adhesion of the polymer to the stamp and b) thermal stress based on different thermal contraction behavior of stamp and polymer [Guo, 2007]. Free standing structures with high aspect ratios show especially high risk of damage [Worgull, 2004].

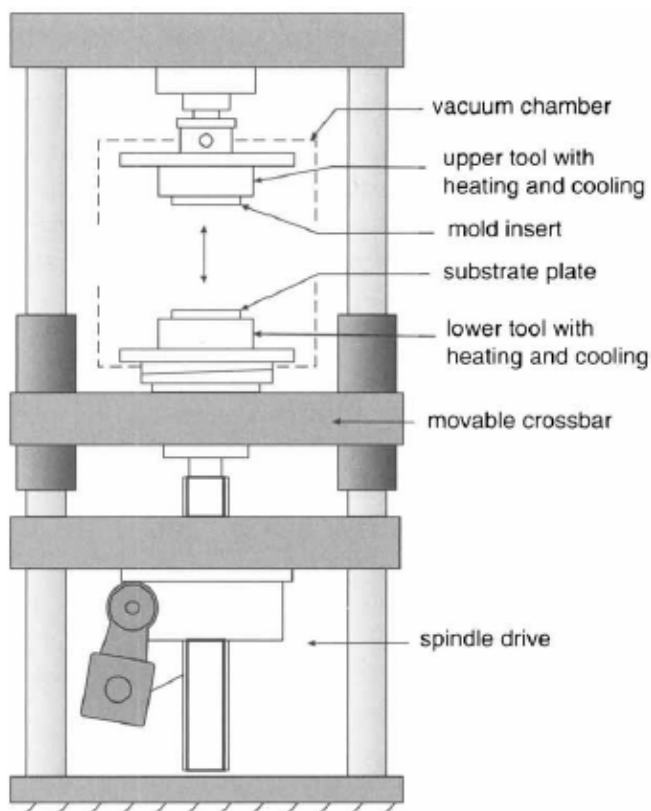


Figure 31: Hot embossing machine with main components which can be split into four groups: a frame with high stiffness, a tool with integrated heating and cooling unit, a microstructured mold insert, and a control unit as an interface to the user. [Worgull, 2009]

3.2.2 Optimization of the Hot Embossing Process

The previous chapter (chapter 3.2.1) described the fabrication of aluminum stamps with high surface quality as well as high feature precision. In the following chapter, the replication of microfluidic channels in TOPAS 5013 is presented in order to develop a basic hot embossing strategy. Embossing experiments on TOPAS/PEDOT assemblies (Chapters 5.3.2 and 5.3.3) are based on optimized process parameters determined in this chapter. The most important parameters of an embossing process are [Worgull, 2009]:

- molding temperature and heating rate
- touch force
- molding force and molding velocity
- holding time
- cooling time and cooling rate
- demolding temperature and demolding velocity

Experimental Parameters

The custom-made embossing press used for all embossing experiments did not allow control of all above mentioned parameters. The molding as well as demolding velocity could only be changed in the range from 1 mm/min to 10 mm/min. Worgull et al. [Worgull, 2009] suggested to perform embossing at velocities of around 1mm/min. Due to sufficient good results, this value was chosen without further analysis. The touch force could not be varied. The upper heating element was not assembled to the pressure frame. It was manually placed on top of the substrate and aligned before the embossing process was started. Finally, heating and cooling rates were pre-defined in the machine code. Molding temperature, molding force, holding time, and demolding temperature were investigated in order to find optimum process parameters for later fabrication of the electrochemical sensors.

Aluminum stamps, Ø50 mm in diameter, with inverse channel structures of 10 µm to 50 µm in height (10 µm steps) were fabricated by micromilling using a Ø1 mm, four flute flat end mill at a feed rate of 0.25 µm/tooth and a cut speed of 80 m/min. Before the embossing was started the stamp was positioned on an injection molded Ø50 mm, 2 mm thick TOPAS 5013 substrate. The stack was placed between the two heating elements of the embossing press. Since the upper heating element was lying on top of the substrate (without possibility to fix it to the upper emboss) a touch force of about 2 N was set for all embossing experiments. The applied heating rate of about 1°C/s was defined by the machine code. After achieving the molding temperature, stamp and sample were heated for 120 s before pressure was applied. The cooling rate was predefined to a rate of approximately 0.3°C/s. Demolding was realized by mechanical separation of stamp and replica using a scalpel after removing the stamp-

polymer assembly from the press (time between removal and separation approximately 3 s). The fulcrum was set beside the channel structures, so that horizontal forces were parallel to the channel direction.

100 μm wide and 20 μm high channels were analyzed for optimization process. After completion of the optimization, profiles of 10 to 50 μm high channels were measured to verify the successful replication of different channel heights for the optimized parameters.

Molding Pressure

To achieve a complete replication of microfluidic channels, the required molding pressure was investigated at 135°C, 143°C, and 150°C. The holding time was set to 600 s. For 143°C and 150°C, the initial molding pressure was set to 1 bar, for 135°C to 3 bar. For each following sample the molding pressure was successively increased until two replicas had the same profile indicating completed replication.

Profiles of the left sidewalls of replicated channels are presented in Figure 32. Figure 33 shows profiles of completely replicated channels for all three embossing temperatures and the corresponding magnification of the left channel sidewalls for a better visualization of the replication fidelity. Profiles of the left sidewalls (recorded from the top to the bottom) were chosen since they display a geometry which is much closer to reality than profiles of the right sidewalls (recoded from the bottom to the top (Chapter 3.1.3.1)).

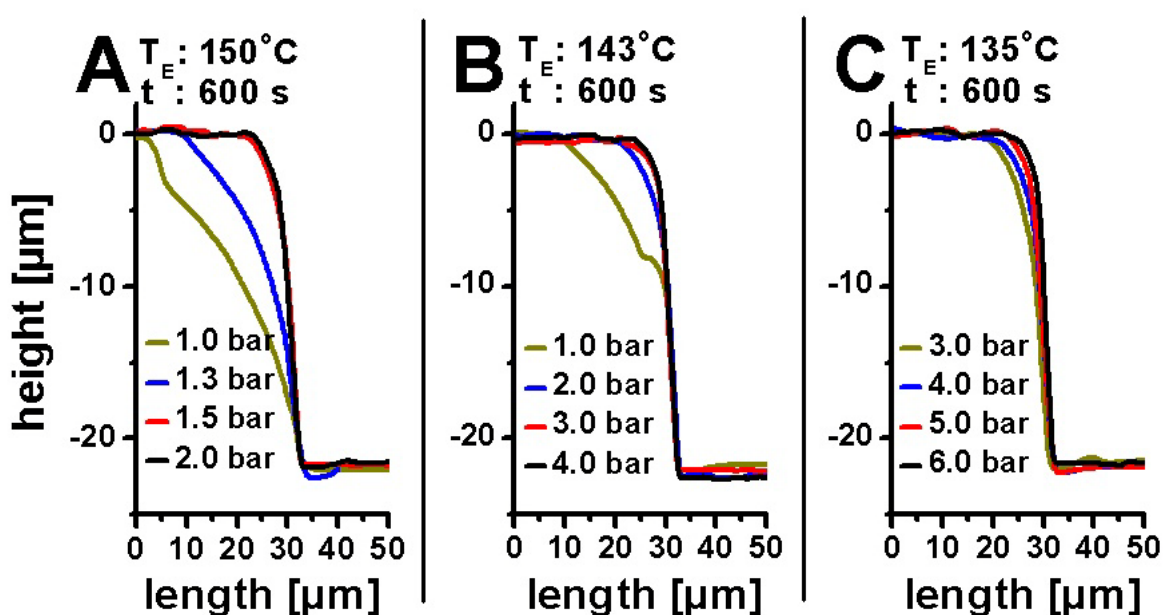


Figure 32: Sidewall profiles of 20 μm deep channels replicated in TOPAS 5013 at different molding pressures. Pressure dependency on replication fidelity for embossing temperatures (T_E) of A) 150°C, of B) 143°C, and of C) 135°C. All embossing processes were performed with holding times (t) of 600 s. (Note: vertical axis is expanded by factor of 1.5)

A pressure of at least 1.5 bar for a molding temperature of 150°C was necessary to achieve a complete replication of the microfluidic channel structure. The pressure had to be increased to 3.0 bar for a molding temperature of 143°C and further to 6.0 bar for a temperature of 135°C.

The high molding pressure of 6.0 bar at 135°C is caused by the fact that the embossing was realized at the glass transition temperature (T_g). Around T_g the polymer starts to soften and changes from a glassy into a visco-elastic state. The embossing experiment was therefore realized in the transition range between the two states. The higher the temperature the lower the viscosity of the polymer and the lower pressure is needed for a complete replication. A non-linear decrease of viscosity starting from T_g to $T_g + 50^\circ\text{C}$ was found in compression experiments with TOPAS 8007 by Jena et al. [Jena, 2011]. Due to the non-linear decrease of the polymer viscosity, a non-linear decrease of the necessary molding pressure to 1.5 bar at 150°C was determined in the experiments presented here.

Presented results show the possibility of complete replication with identical quality for molding processes at T_g and up to 15°C above T_g (Figure 33). In contrast, Jena et al. [Jena, 2011] were not able to achieve complete replication at temperatures around T_g . This difference could be caused by the use of different TOPAS grades as well as additives, the identities of which are usually proprietary information [Jena, 2011].

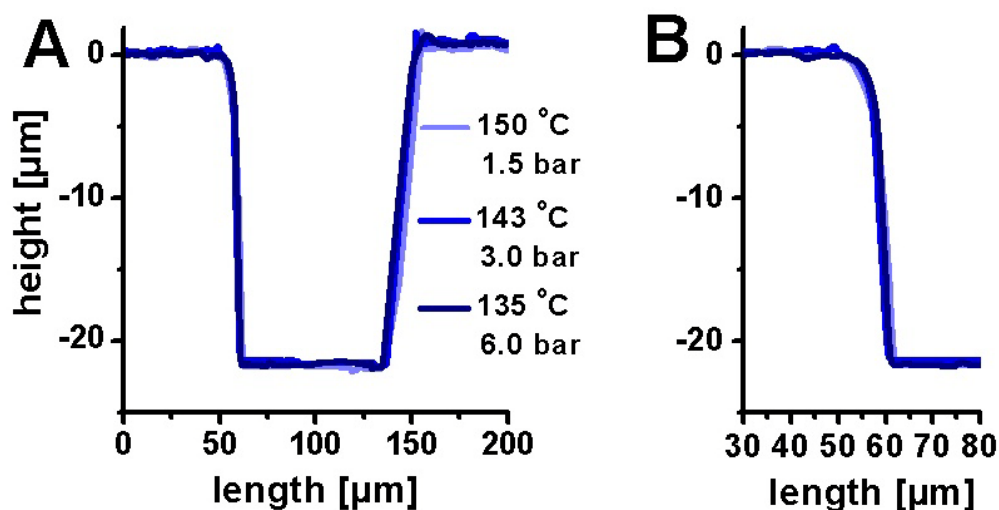


Figure 33: Overlay of channel profiles replicated in TOPAS 5013 at embossing temperatures and pressures of 150 °C and 1.5 bar (dark blue), 143 °C and 3.0 bar (blue) as well as 135 °C and 6.0 bar (light blue). A) presents the whole channel profile, B) a magnification of the left channel sidewall.

Holding Time

To shorten the embossing cycle the holding time required to achieve complete replication was analyzed for molding temperatures of 135°C, 143°C, and 150°C. The holding time was initially set to 60 s and increased in 60 s steps for each following replica until no change in the profiles was found. Time-dependent channel sidewall profiles for all three investigated molding temperatures are presented in Figure 34.

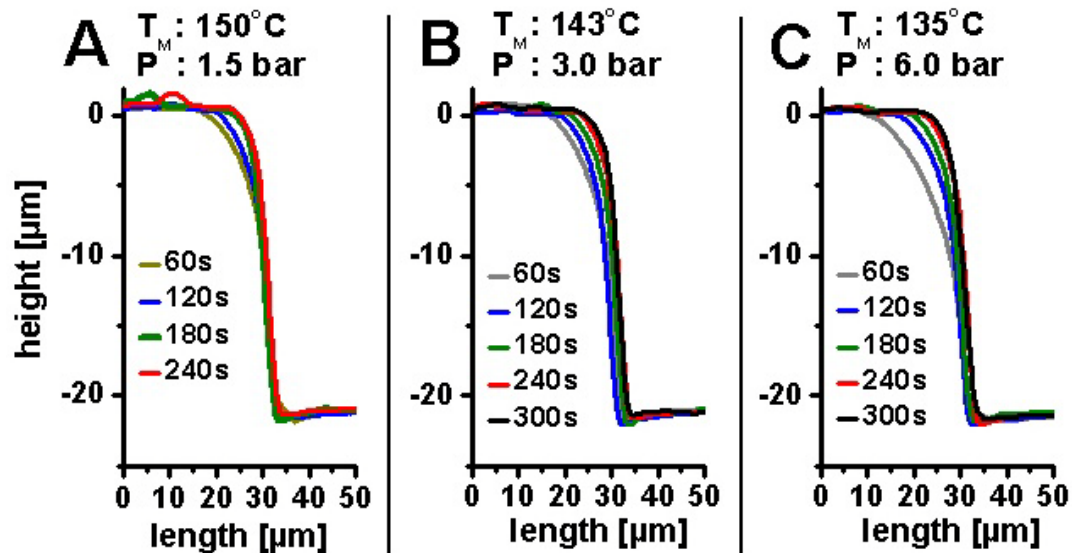


Figure 34: Sidewall profiles of 20 μm deep channels replicated in TOPAS 5013 presenting the holding time dependency for molding steps performed at A) 150°C and 1.5 bar, B) 143°C and 3.0 bar, and C) 135°C and 6.0 bar.

An increase of the holding time from 180 s to 240 s with a decrease of molding temperature from 150°C to 143°C was observed. No changes were found for a further decrease of the molding temperature to 135°C.

The increase of the holding time was probably required to overcome the increased elasticity of the polymer at lower molding temperatures.

An overlay of the profiles at minimum holding time for all three temperatures is presented in Figure 35 which demonstrates equal replication quality for all investigated temperatures.

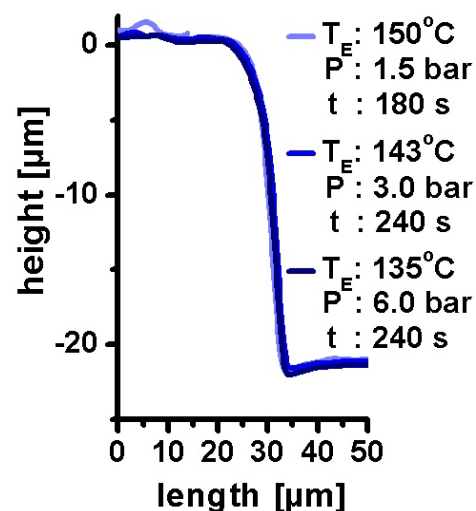


Figure 35: Sidewall profiles of 20 μm deep channels replicated in TOPAS 5013 at embossing temperatures (T_E), pressures (P), and holding times (t) of 150°C, 1.5 bar and 180 s (light blue), 143°C, 3.0 bar, and 240 s (blue) as well as 135°C, 6.0 bar and 300 s (dark blue).

The upper channel edge of all recorded channel profiles appears as rounded which could be caused by incomplete replication, an artifact of the profilometric analysis, or due to a suboptimal stamp profile. In order to investigate the latter case, the stamp was replicated in PDMS. After curing, the PDMS replica was separated from the stamp and cut across the channel structure. A micrograph of the cross section of the replicated channel structure is presented in Figure 36 A. The magnification (Figure 36 B) of the left channel sidewall shows clearly that the round edges presented in the sidewall profiles above, are caused by the stamp profile. This verifies that channels molded at optimized parameters were completely replicated.

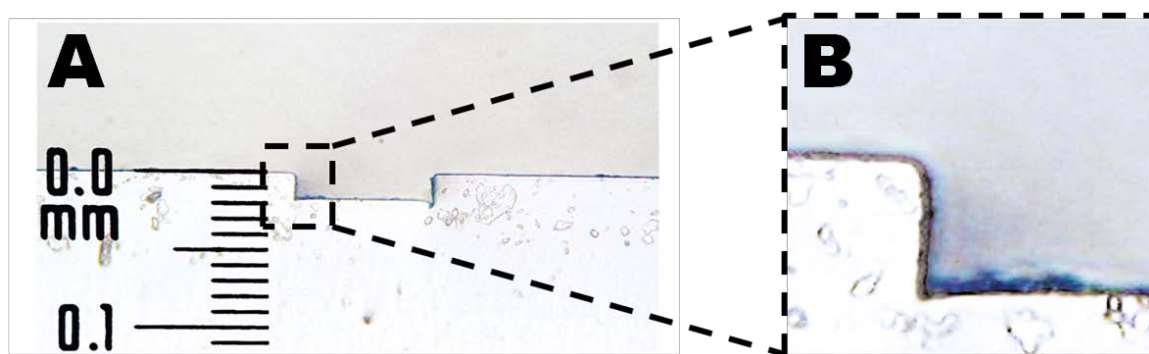


Figure 36: Micrograph of a PDMS replica made from an aluminum stamp, A) cross-section of a 100 μm wide and 20 μm high channel; B) magnification of the left channel sidewall.

Release Temperature

As discussed above the demolding is the most critical step in the hot embossing process. Unfortunately, an automatic controlled release was impossible with the used equipment. Therefore, the separation of the stamp and the polymer replica was realized manually using a scalpel. However, the release temperature was investigated in order to minimize the adhesion between stamp and polymer.

For the demolding, the stamp/polymer assembly was taken out of the molding press. The separation of stamp and polymer took place within 3 s during which the assembly was exposed to room temperature. In order to investigate the temperature drop within this time period, a temperature sensor was placed at the interface of stamp and polymer before the embossing process started. After removing the assembly from the press at 130°C, the temperature drop was recorded. The measured temperatures are shown in Figure 37.

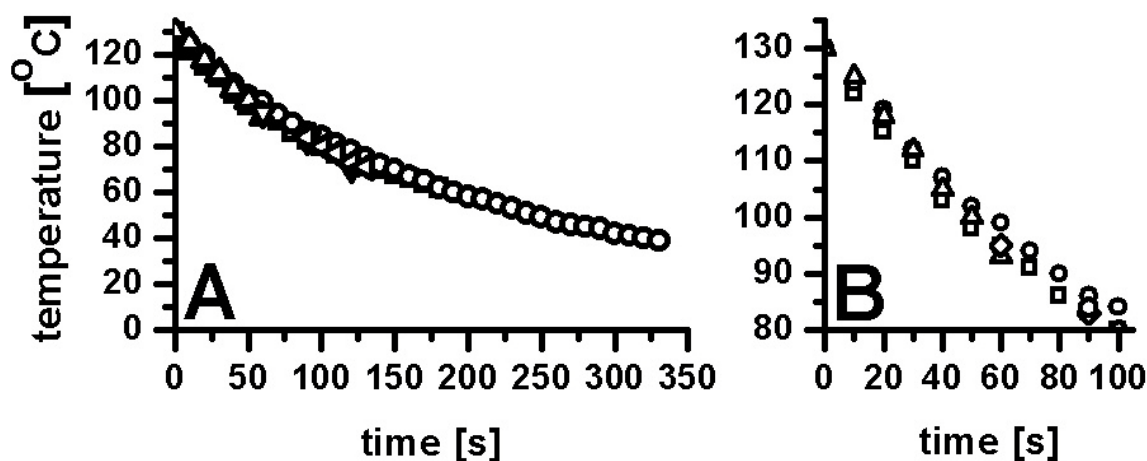


Figure 37: Temperature decrease at the stamp-polymer interface after removal from the press at 130°C (assembly exposed to room temperature): A) temperature decrease from 130°C down to 40°C, B) magnification for temperatures from 130°C to 80°C. The different symbols represent different measurements.

From Figure 37 B, a drop of approximately 0.5°C/s at higher temperatures ($T \geq 80^\circ\text{C}$) was estimated. The separation of stamp and polymer was realized within 3 s. This means that for the following investigation of the release temperature, the assembly had to be removed from the embossing press 2°C above the predetermined release temperature. For lower temperatures ($T < 80^\circ\text{C}$) the assembly was removed 1°C above release temperature.

Profiles of molded microfluidic channels, released at different temperatures are presented in Figure 38. Release-temperatures from 40°C to 120°C ($T_{g\text{ TOPAS } 5013} \sim 135^\circ\text{C}$) were investigated. No significant differences in the replication quality were found within the analyzed range.

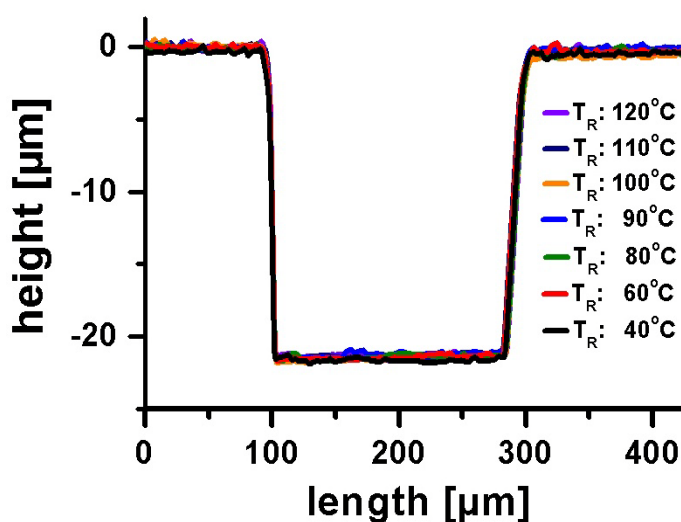


Figure 38: Profiles of 200µm wide and 20 µm deep channels replicated in TOPAS 5013 and manually released at temperatures between 40°C and 120°C.

Summary

The optimization of the molding process resulted in defined process parameters which were applied for all following hot embossing experiments (unless otherwise stated). For embossing processes at 150°C at least 1.5 bar for 180 s had to be applied in order to achieve complete replication of channel structures. For molding processes at 143°C at least 3 bar for 240 s and at 135°C at least 6 bar for 240 s were required. The investigation of the release temperature between 40°C and 120°C showed no significant influence on the replication quality. In order to keep the cycle time short a release temperature of 120°C was chosen for following experiments.

Molding of Channels with Different Heights

The optimization process was based on 20 μm high channels. To demonstrate that the optimized parameter are equally valid for channels of various dimensions, 300 μm wide and 10 μm to 40 μm high channels were replicated in TOPAS 5013. Recorded profiles of the replicas showed identical replication fidelity and demonstrated the applicability of the optimized process parameters for different channel dimensions (Figure 39).

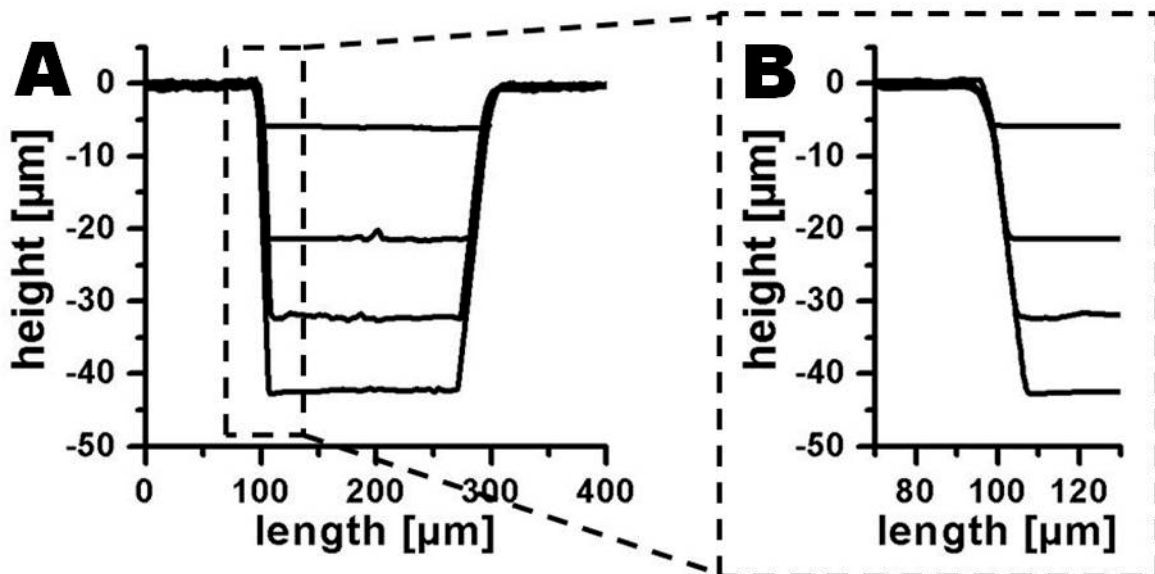


Figure 39: Profiles of 300 μm wide and 10 μm to 40 μm high channels replicated in TOPAS 5013, A) presents the entire channel profiles and B) a magnification of the left channel sidewall.

3.2.3 References

- [Becker and Gärtner, 2000] Becker, H.; Gärtner, C. *Electrophoresis* **2000**, *21*, 12-26
- [Becker and Gärtner, 2008] Becker, H.; Gärtner, C. *Analytical and bioanalytical chemistry* **2008**, *390*, 89-111
- [Goral, 2011] Goral, V. N.; Hsieh, Y.-C.; Petzold, O. N.; Faris, R. a; Yuen, P. K. *Journal of Micromechanics and Microengineering* **2011**, *21*, 017002
- [Guo, 2007] Guo, Y.; Liu, G.; Zhu, X.; Tian, Y. *Microsystem Technologies* **2007**, *13*, 411-415
- [Jena, 2011] Jena, R. K.; Chester, S. a.; Srivastava, V.; Yue, C. Y.; Anand, L.; Lam, Y. C. *Sensors and Actuators B: Chemical* **2011**, *155*, 93-105
- [Liedert, 2012] Liedert, R.; Amundsen, L. K.; Hokkanen, A.; Mäki, M.; Aittakorpi, A.; Pakanen, M.; Scherer, J. R.; Mathies, R. a; Kurkinen, M.; Uusitalo, S.; Hakalahti, L.; Nevanen, T. K.; Siitari, H.; Söderlund, H. *Lab on a chip* **2012**, *12*, 333-339
- [Peng, 2009] Peng, B.-Y.; Wu, C.-W.; Shen, Y.-K.; Lin, Y. *Polymers for Advanced Technologies* **2009**, *21*, 457-466
- [Qi, 2002] Qi, S.; Liu, X.; Ford, S.; Barrows, J.; Thomas, G.; Kelly, K.; McCandless, A.; Lian, K.; Goettert, J.; Soper, S. a *Lab on a chip* **2002**, *2*, 88-95
- [Worgull, 2004] Worgull, M.; Hecke, M. *Microsystem Technologies* **2004**, 432-437
- [Worgull, 2009] Worgull, M.; Elsevier Inc.; Hot Embossing - Theory and Technology of Microreplication; **2009**, ISBN: 978-08155-1579-1

3.3 Bonding of Microfluidic Channels

After the fabrication of microfluidic channels, open channel structures need to be sealed for the final application. The bonding method needs to be chosen carefully, since deformation and blocking of the microfluidic structures can easily occur.

A wide range of different techniques has been developed to seal polymeric microfluidic systems. They can be divided into two main groups: indirect and direct bonding techniques [Tsao, 2009].

3.3.1 Indirect Bonding Techniques – “Adhesive Bonding”

Adhesives are widely used to seal microfluidic systems. A large variety of adhesives is commercially available and has been successfully applied to seal microfluidic systems. One of the simplest is the application of glue, epoxies or acrylates [Tsao, 2009]. Polydimethylsiloxane (PDMS) films or PDMS based adhesives have also been used to bond two polymer substrates together. For high throughput application the lamination process is often used. Hereby a polymer foil is modified with a thin adhesive layer. The adhesive is activated by heat, pressure or both together which are applied during the lamination process [Becker and Gärtner, 2008].

However, for all indirect bonding techniques it is important to use adhesives with a high viscosity in order to prevent a blocking of the channel during bonding process. To reduce the risk that adhesives penetrate the structures, support structures can be used which guide the flow of the adhesive [Becker and Gärtner, 2008].

3.3.2 Direct Bonding Techniques

Direct bonding techniques are processes where a stable bond is achieved without introduction of additional material at the interfacial bonding area. This group involves e.g. plasma assisted bonding, solvent assistant bonding, localized welding techniques, and thermal bonding.

Plasma Assisted Bonding

The exposure of polymer samples to ultraviolet radiation or plasma (e.g. oxygen or argon) leads to breakage of polymer chains, development of radicals or introduction of new functional groups at the polymer surface. The new surface properties and functional groups support the bonding process and lead to strong interfacial bonds.

Solvent Assisted Bonding

The application of solvent at the interface of two polymer samples leads to a solvation of the polymer surfaces. The polymer chains of both samples become more mobile and entangle easier with each other. The polymer solidifies upon evaporation of the solvent, resulting in exceptionally strong bonds [Becker and Gärtner, 2008; Tsao, 2009].

Local Welding Assisted Bonding

Melting of the polymer and therefore an increased polymer chain interaction at the interface can be achieved by localized welding techniques like ultrasonic or laser welding. During ultrasonic welding an ultrasonic actuated mechanical movement is applied at the interface to induce local heating. Laser welding is based on the transmission of light (typically infrared) through one of the two polymer samples and the adsorption of the energy close to the interface of the second polymer sample. The main disadvantage of this technique is the necessary application of two different polymer types: a transparent and a non-transparent polymer towards the applied light.

Thermal Bonding

The simplest procedure to bond two thermoplastic polymer parts together without any surface modification or introduction of additional material is thermal bonding. Two polymer samples are heated to a temperature close to the glass transition temperature. The application of pressure increases the contact forces and allows an entanglement of polymer chains across the interface. After cooling, bonding strengths similar to the cohesive strength of the bulk material can be obtained. [Tsao, 2009].

Due to the absence of additional surface modifications, the sealed microfluidic channels possess homogenous surface properties. Furthermore, high bonding strength, the simplicity of the process, and the application of cheap equipment, like a controlled heated press, made thermal bonding the most common method for bonding of microfluidic systems [Brown, 2006; Tsao, 2009].

However, the process parameter range for the applied combination of temperature and pressure is relatively small. Insufficient applied temperature or pressure lead to incomplete bonds. Too high temperatures and pressures cause structural deformation of the microfluidic system. Thus, an optimization of the process parameters needs to be done for every design.

Due to the specificity of the bonding parameter on the design, the applied bonding methods and necessary optimization of parameter are described in the chapters of the corresponding fluidic devices.

3.3.3 References

- [Becker and Gärtner, 2008] Becker, H.; Gärtner, C. *Analytical and bioanalytical chemistry* **2008**, *390*, 89-111
- [Brown, 2006] Brown, L.; Koerner, T.; Horton, J. H.; Oleschuk, R. D. *Lab on a chip* **2006**, *6*, 66-73
- [Tsao, 2009] Tsao, C.-W.; DeVoe, D. L. *Microfluidics and Nanofluidics* **2009**, *6*, 1-16

Chapter 4

Conducting Polymers in Electrochemical Biosensors

4.1 Electrochemical Biosensors

The integration of electrodes into a microfluidic system allows the fabrication of analytical electrochemical systems. A modification of the electrodes with a recognition element introduces specificity to the system and allows the construction of an electrochemical sensor. Modification of the electrode with biological recognition elements, e.g. antibodies, enzymes, or cells transforms an electrochemical sensor into an electrochemical biosensor.

Generally, a biosensor can be defined as a device that consists of a biological recognition element and a transducer. In case of an electrochemical biosensor the biological recognition event (interaction between recognition element and analyte) causes physical or chemical changes which the transducer (electrode) converts into an electrical signal [Vo-Dinh, 2000, Gerard, 2002]. Thus, electrochemical biosensors combine the selectivity provided by the biological recognition element with the sensitivity of electrochemical measurement [Vo-Dinh, 2000, Rozlosnik, 2009]

4.1.1 The Biological Recognition Element

The biological recognition element (from now on referred to as biomolecule) is commonly immobilized directly at the electrode which ensures a parameter change directly at the electrode / analyte interface and therefore a fast and sensitive detection. The immobilization procedure needs to ensure an efficient and stable immobilization of the biomolecule on the transducer surface; a complete retention of its biological properties; and the accessibility for the analyte. Biocompatibility and chemical inertness of the host structure are important as well [Cosnier, 2003]. Electrode modifications are mainly achieved by adsorption, physical entrapment, or covalent binding of the biomolecules to the electrode. Reported immobilization techniques are summarized by Vo-Dinh et al. [Vo-Dinh, 2000] and Sarma et al. [Sarma, 2009] as well as by Gerard et al. [Gerard, 2002], Cosnier et al. [Cosnier, 2003;], and Ahuja et al. [Ahuja, 2007] with focus on biosensors related to conducting polymers.

Among various immobilization techniques the electrochemical entrapment of biomolecules is the most extensively used strategy for an electrode modification [Guimard, 2007]. Hereby an electro-polymerizable monomer is mixed together with the biomolecule in a single aqueous solution (buffer). Subsequently a polymer film is deposited using either potentiometry or galvanometry [Gerard, 2002, Guimard_2007]. The biomolecules in the vicinity of the electrode surface will be immobilized by incorporation into the growing polymer film [Cosnier, 2003]. Besides the high control of the process [Gerard, 2002; Cosnier, 2003], this

reagentless electrochemical approach is easily applicable to a wide range of biological macromolecules [Cosnier, 2003]. Reviews about advantages, disadvantages as well as biosensorial applications are presented by Cosnier et al. [Cosnier, 2003] and Ahuja, 2007 [Ahuja, 2007].

4.1.2 Glucose Selective Electrodes

A wide range of redox enzymes have been immobilized at electrodes in order to construct biosensors. Glucose oxidase is the most commonly used enzyme due to its importance for blood sugar detection [Sarma, 2009]. Amperometric glucose biosensors based on a glucose oxidase modified electrodes played a leading role in the development of blood sugar analyze systems. Furthermore they are expected to be a key feature for the development of continuous glucose monitoring [Wang, 2008].

The simplest detection principle of glucose relies on the detection of hydrogen peroxide which is a side product of the biocatalytical oxidation of glucose to gluconolactone [Wang, 2008]. The hydrogen peroxide can be detected directly at a platinum electrode, polarized at +0.6 V (versus Ag/AgCl). However, the amperometric detection of hydrogen peroxide at +0.6 V in biological samples will be interfered with other present redox active species like ascorbic and uric acids as well as some drugs like acetaminophen [Wang, 2008].

Permselective coatings have been applied to enzyme electrodes in order to minimize the accessibility of the electrodes for interfering molecules. One type of coatings are electropolymerized films which reduced interference successfully [Palmisano, 1993]. Another possibility to avoid interference is to reduce the detection potential to a range where interfering substances are not detectable e.g. by using prussian blue modified electrodes. Due to a very strong and stable electrocatalytic activity of prussian blue, the detection potential can be reduced to a range between 0 and -0.1V (versus Ag/AgCl) [Karyakin, 1996; Wang, 2008]

4.1.3 Integration of Electrodes into Polymer Fluidic Systems

The majority of amperometric glucose biosensors are based on noble metal electrodes [Sarma, 2009]. However, the integration of a metal electrode into a thermoplastic microfluidic system causes problems due to a weak adhesion of the metal to the polymer [Kääriäinen, 2009, Huang, 2011]. Even though the adhesion strength can be increased by pre-treatment of the polymer e.g. by oxygen plasma or by application of an adhesion promoter, most thermoplastic polymers are not compatible with the common photolithographic techniques used for electrode structuring [Becker and Gärtner, 2008]. TOPAS overcomes the latter problem and also shows acceptable adhesion to gold [Lee, 2005; Illa, 2010]. Still, expensive cleanroom facilities are necessary to structure the electrodes.

Conducting polymers are excellent candidates for replacing electrodes in polymer-based systems due to their electrical similarity to metals and inorganic semiconductors. They also possess attractive properties such as simplicity of synthesis and flexibility of processing [Rozlosnik, 2009]. Furthermore photolithography for electrode structuring can be avoided. Reactive ion etching [Kiilerich-Pedersen, 2011] and wet chemistry [Hansen, 2007] were successfully applied to structure conducting polymer microelectrodes in previously spin coated PEDOT films.

4.2 Spin Coating of PEDOT

Before definition of electrodes in a PEDOT layer, the reproducible synthesis of a homogeneous layer needs to be ensured. Spin coating allows the application of thin homogeneous layers on top of a carrier substrate with a high control of the resulting layer thicknesses. For spin coating the substrate is placed in a spin coater on a rotating chuck and is fixed by applying vacuum during spinning.

The general spin coating process can be divided into 4 steps [CEE; Birnie, 2005]:

- Fluid is carefully deposited in the center of the substrate using a pipette or nozzle. This can be done on a static (static dispense) or slow rotating (dynamic dispense, ~500 rpm) substrate. Dynamic dispense has the advantage that a smaller volume of fluid is required to cover the substrate and is often used if the surface has poor wetting abilities.
- The substrate accelerates to the final rotational speed. Centrifugal forces cause a radial outwards flow of the fluid to the edge. Twisting forces caused by acceleration enhances the dispersal of the fluid on the whole surface. Excess fluid may be ejected from the edge of the substrate.
- At a constant spinning speed the remaining fluid thins out gradually from the center. Solvent evaporation gradually increases the viscosity until finally a stable film is formed.
- Immediately after deceleration the wafer is usually placed onto a hot plate to evaporate remaining solvents and to solidify the layer.

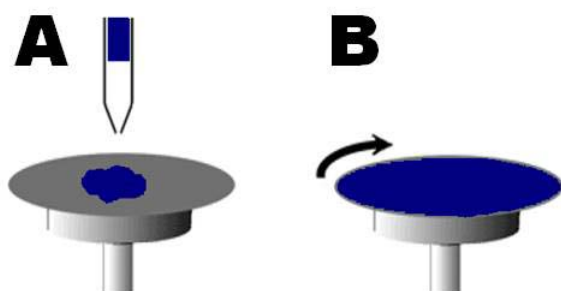


Figure 40: Illustration of spin coating process (static dispense). A) Application of fluid in the center of a substrate using a pipette or nozzle. B) Substrate rotates and fluid is homogeneously distributed over the entire surface. [picture adapted from CEE]

The final layer thickness is mainly influenced by two parameters:

a) Viscosity of the fluid:

The higher the viscosity, the larger the resulting layer thickness for a given rotational speed. Since the concentration of the solvent influences the viscosity of the fluid, a solvent with an adequate vapor pressure should be used to ensure formation of a homogenous layer.

b) Rotational speed:

The higher the rotational speed, the thinner the resulting layer thickness for a fluid with a given viscosity. Common speeds are between 500 rpm and 5000 rpm [CEE].

The influence of rotational speed on the final layer thickness is commonly presented as calibration curve of layer thickness versus spin speed for a certain time duration [Krishnan and Sarma, 2008].

4.2.1 PEDOT Single-Layer Synthesis

All of the developed electrochemical systems (Chapter 5) are based on thin PEDOT layers. To ensure reproducibility of the fabricated electrochemical systems, the reproducibility of the PEDOT layer thickness needed to be guaranteed. Especially for the drilled tubular (Chapter 5.2) as well as embossed (Chapter 5.3) electrodes, a homogeneous as well as reproducible PEDOT application is necessary in order to compare obtained results during the fabrication process as well as electrochemical detection.

The optimization of the spin coating process included the analysis of different substrate cleaning procedures and the influence of the spin speed, the time and the applied volume of the polymerization solution. Finally, the synthesis of PEDOT multilayers was investigated in order to increase the final film thickness

Experimental Parameters

Injection molded Ø50 mm TOPAS 5013 discs (Topas Advanced Polymers) were cleaned with a tissue soaked with solvent (ethanol unless otherwise stated). The substrates were placed into the spin coater and flushed in a nitrogen stream to remove residual dust particles from air or tissue. Immediately afterwards 0.7 ml of a solution (polymerization solution) containing 2170 µl CLEVIOS™ C-B50 (H.C. Starck), 670 µl ultra-pure water (≥18 MΩ cm), 50 µl pyridine (Fluka, 99%), and 80 µl CLEVIOS™ M V2 (H.C. Starck, >98%) was applied in the center of the substrates and the spin coating process was started. Spin coating was realized at 1000 rpm (acceleration = 1000 rpm/s) for 60 s. For substrate cleaning optimization also untreated wafers were spin coated to analyze the effect of the cleaning procedures. After spin coating, the substrates were baked at 65°C for 15 min to increase the polymerization rate and to evaporate remaining solvent. Polymerized PEDOT films were washed with deionized water and dried in a nitrogen stream.

For multilayer synthesis the volume of the polymerization solution and the spin coating time were reduced to 500 µl and 40 s, respectively.

The most important criteria concerned the coverage of the entire substrate surface, the homogeneity, and the final thickness of the synthesized PEDOT layers. The homogeneity was analyzed by measuring the PEDOT thickness at five different spots along the median after removal of half of the PEDOT layer with an adhesive tape.

Substrate Cleaning

For synthesis of a continuous and homogenous PEDOT layer, it was necessary to remove dust particles as well as other contaminations (dirt, fat from fingerprints, lubricants, etc.) from the wafer surfaces. Therefore, TOPAS 5013 wafers were cleaned either with acetone, isopropanol, or ethanol before spin coating. The synthesized PEDOT layers were characterized with respect to complete coverage of the substrate surface, homogeneity and layer thickness.

Incomplete covered surface areas were observed for untreated as well as acetone and isopropanol cleaned substrates (Figure 41). Ethanol cleaning of the wafer surface yielded always in a complete PEDOT coverage. The ethanol treatment seems to increase the wettability of wafer surface and favored polymerization solution distribution.

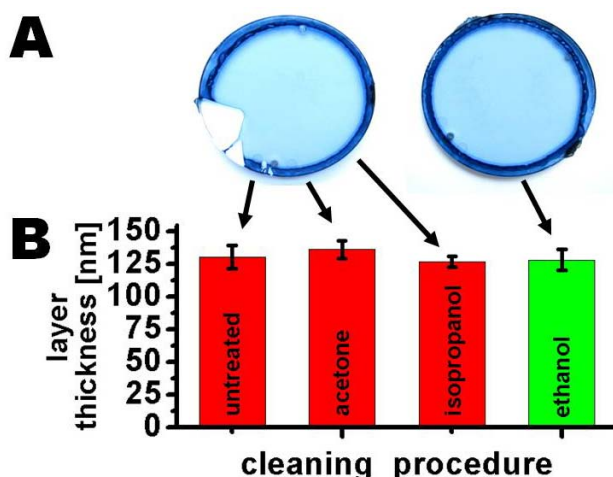


Figure 41 A) Photographs of PEDOT covered TOPAS 5013 wafers. The wafer to the left is an example for an incomplete PEDOT covered wafer surface as observed for untreated as well as for acetone and isopropanol cleaned surfaces. The wafer to the right, cleaned with ethanol shows a complete surface coverage. B) PEDOT layer thicknesses for untreated, and acetone, isopropanol, as well as ethanol cleaned surfaces (spin coating parameter: 1000 rpm, 1000 rpm/s, 60 s, 0.7 ml; error bars: standard deviation of three independent samples)

PEDOT layer thicknesses were analyzed on three independent samples for each cleaning procedure. Thicknesses of 130 ± 9 nm for untreated, 133 ± 7 nm for acetone, 126 ± 4 nm for isopropanol, and 128 ± 8 nm for ethanol cleaned TOPAS substrates were recorded. Hence, apart from a slightly better reproducibility of PEDOT syntheses on isopropanol cleaned surfaces, no differences in the layer thicknesses were found.

A cleaning procedure based only on ethanol was sufficient to guarantee a complete coverage of the surface with a homogenous PEDOT layer. Therefore, all further TOPAS substrates were cleaned with ethanol before a PEDOT synthesis.

Spin Time

The influence of the spin time within 60 s was investigated. TOPAS samples were cleaned with ethanol and flushed with nitrogen before the spin coating was started. Independent samples were spin coated for time intervals from 10 s to 60 s (10 s steps).

An influence of spin time on the PEDOT layer thickness was found for a process time below 20 s. A spin time of 10 s resulted in a thickness of 220 nm while 20 s to 60 s showed a uniform thickness of 192 ± 7 nm (Figure 42).

The spinning process does not necessarily allow all solvent to evaporate during spinning. Excess of polymerization solution accumulated at the rim was still liquid using spin durations of less than 40 s. A flow of the polymerization solution towards the center was observed after deceleration, resulting in reduced homogeneous PEDOT areas at the center. The diameters of the homogenous PEDOT areas increased non-linear from 34 mm for 10 s to 45 mm for 40 s. Spin times up to 60 s resulted in a minor increase of the homogenous area to 46 mm (Figure 43). Thus, a spin time of minimum 40 s was required to minimize the flow of the polymerization solution. The reduced flow is caused by a sufficient solvent evaporation and therefore an increased viscosity of the polymerization solution.

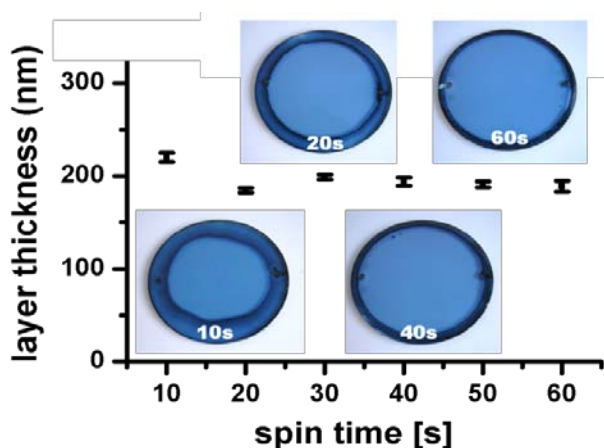


Figure 42: Influence of spin time on PEDOT layer thickness. Inserts. Photographs of synthesized PEDOT layers on Ø50 mm TOPAS 5013 discs with spin times of 10 s, 20 s, 40 s, and 60 s (parameter: 1000 rpm, 1000 rpm/s, 0.7 ml)

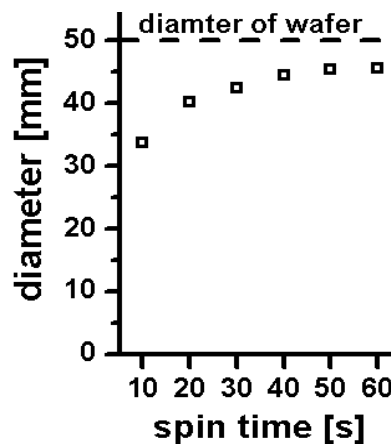


Figure 43: Influence of spin time on the diameter of the homogeneous PEDOT area (bright blue area in the center of the PEDOT layer, see inserts in Figure 42).

Volume

The impact of the applied volume on the final PEDOT layer is limited to the degree of surface coverage. To minimize the applied volume of the polymerization solution, TOPAS wafers were cleaned and spin coated with 400 µm up to 900 µl of the polymerization solution.

Complete coverage of the TOPAS wafers was found for volumes of more than 500 µl. For smaller volumes insufficient coverage of the TOPAS substrates were observed (Figure 44).

In the analyzed volume range no significant influence on the layer thickness or the homogeneity was observed. A small increase in layer thickness with increasing volume, reaching a maximum at 700 µl, followed by small decrease was observed. Changes in layer thickness are about 15 nm (185 nm for 400 µl, 200 nm for 700 µl, and 184 nm for 900 µl) (Figure 44). The experiment was repeated twice with similar results. However, no investigations have been done to analyze these observations.

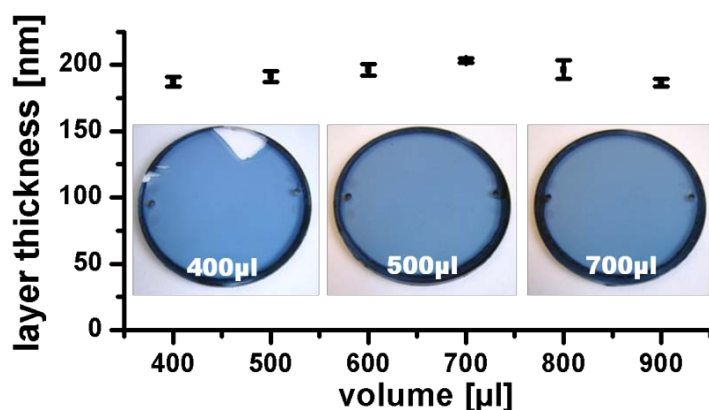


Figure 44: Influence of applied volume of polymerization solution on PEDOT layer thickness. Inserts: Photographs of synthesized PEDOT films on Ø50 mm TOPAS discs using polymerization solution volumes of 400 µl, 500 µl, and 700 µl. (spin coating parameter: 1000 rpm, 1000 rpm/s, 60 s)

Spin Speed

The spin speed is the crucial parameter in the spin coating processes and mainly defines the final layer thickness. Ethanol cleaned TOPAS wafer were spin coated with the polymerization solution at different spin speeds ranging from 250 to 2000 rpm (in 250 rpm steps).

An increase in spin speed caused a non-linear decrease of the layer thickness from 432 ± 17 nm at 250 rpm down to 128 ± 6 nm at 2000 rpm (measured in the center of the wafer on the three independent samples)(Figure 45). Besides a high thickness deviation of layers spin coated at 250 rpm, the homogeneous PEDOT area in the center of these wafers was only 13.5 ± 2.5 cm in diameter and therefore insufficient for further processing.

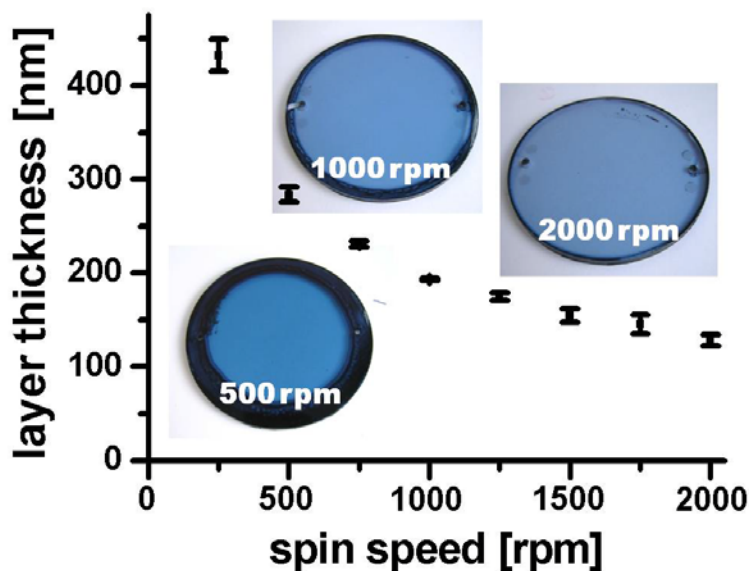


Figure 45: Influence of spin speed on PEDOT layer thickness. Inserts: photographs of synthesized PEDOT layers on Ø50 mm TOPAS discs spin coated at 500 rpm, 1000 rpm, and 2000 rpm (spin coating parameter: 60 s, 1000 rpm/s, 700 µl)

Optimized Spin Coating Parameter for Single PEDOT Layers

In following experiments, PEDOT is spin coated on TOPAS according to the described process: Ethanol cleaned TOPAS substrates are placed into the spin coater and flushed in a nitrogen stream. Immediately afterwards 0.5 ml of the polymerization solution is applied to the center of the substrates. The spin coating is performed for at a spin speed according to the final layer thickness for 40 s. A baking step at 65°C for 15 min after the spin coating increases the polymerization rate and evaporates remaining solvent. Polymerized PEDOT films are washed with deionized water and dried in a nitrogen stream

4.2.2 PEDOT Multilayer Synthesis

For the prototyping of microelectrode arrays (Chapter 5.1) and for PEDOT deformability studies (Chapter 5.3.3), increased PEDOT layer thicknesses were required. This can be achieved by spin coating several PEDOT layers on top of each other forming a stack of PEDOT layers. Such a method would allow layer thicknesses up to several micrometers, which would be impossible to achieve in sufficient quality using single synthesis.

Multilayer Synthesis without Washing Steps

The PEDOT layer thickness was increased by repeated spin coating of the polymerization solution directly on top of the previous layer. The PEDOT film was baked after each after each spin coating step. No washing step or other treatment was done between two layers.

The analysis of the PEDOT thickness showed a linear increase for each applied layer from 128 ± 10 nm for a single layer, to 305 ± 25 nm for a double layer and finally to 470 ± 45 nm for a triple layer. The high inhomogeneity of triple PEDOT layers (± 45 nm) was caused by an initiating crystallization. Crystals of up to $\text{Ø}50 \mu\text{m}$ were observed during imaging with an optical microscope (Figure 46 A). The crystallization is most probably based on an increasing accumulation of the oxidant as well as an excess of tosylate after each synthesis step. Therefore, only few very small crystals ($\text{Ø} < 1 \mu\text{m}$) were observed in a double layer while an increased amount of large crystals ($\text{Ø}30\text{-}50 \mu\text{m}$) in a triple layer. An attempt to remove the crystals by extensive post-washing with water at 50°C for 60 min was unsuccessful. All crystals remained in the film (Figure 46 B).

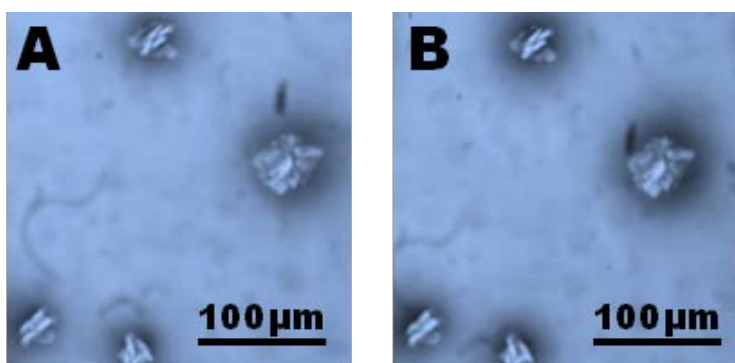


Figure 46: Optical microscope images of a PEDOT triple layer synthesized without washing steps in between the layer depositions after A) a final washing step with deionized water and B) after a further washing step for 60 min in 50°C water

Multilayer Synthesis with Washing Steps

A stack of PEDOT layers was synthesized by introducing washing steps with deionized water in between each layer synthesis. A micrograph of a PEDOT triple layer is presented in Figure 47. No crystals were observed in any of the multilayers. The washing steps removed the synthesis products from the PEDOT films and avoided crystallization within the film.

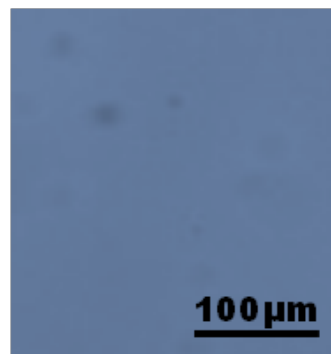


Figure 47: PEDOT triple layer synthesized with washing steps after each layer deposition.

A calibration curve for the layer thicknesses at spin speeds from 500 rpm to 2000 rpm for up to three layers was recorded (Figure 48). A linear increase in thickness was observed for all analyzed spin speeds (Figure 49).

The deviation between different samples was found to be ≤ 7 nm for single, ≤ 8 nm for double (except for 2000 rpm with ± 12 nm) and ≤ 15 nm for triple PEDOT layers, measured at the wafer centers. All PEDOT layers showed a thickness variation across the wafer of 10 nm independent of spin speed or layer thickness.

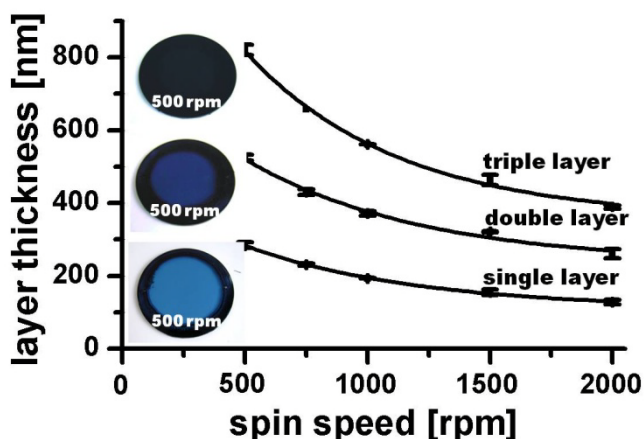


Figure 48: PEDOT layer thicknesses after synthesis of a single, double, and triple layer dependent on spin speed. PEDOT multilayers were synthesized with washing steps after each layer deposition. Inserts: photographs of single, double, and triple PEDOT layer on a Ø50 mm TOPAS 5013 wafer synthesized at 500 rpm (spin parameter: 0.5 ml, 1000 rpm/s, 40 s)

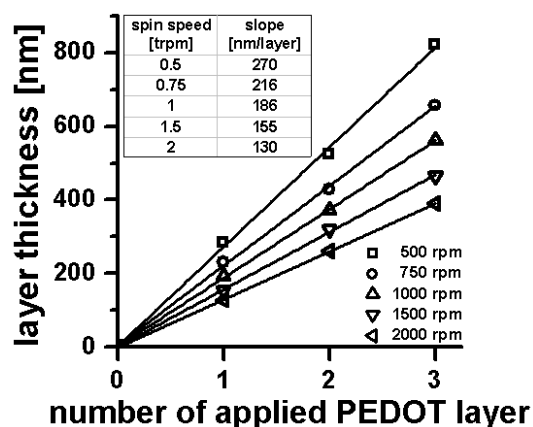


Figure 49: PEDOT layer thicknesses for different applied spin speeds dependent on the amount of applied synthesis steps (PEDOT layer). Inserted table: calculated slopes of thickness increase for corresponding spin speeds.

4.3 Hydrogen Peroxide Detection on Prussian Blue modified PEDOT Layers

A hydrogen peroxide sensitive electrode is the basis for the construction of a simple glucose sensor. The preferred reduction of hydrogen peroxide was demonstrated at electrodes modified with a deposited prussian blue layer [Karyakin, 1996] (Figure 50). However, the preparation of each single electrode is a disadvantage for a sensor mass fabrication. It would be an important improvement to structure the electrodes directly in a hydrogen peroxide sensitive material. The addition of commercially available prussian blue to the PEDOT polymerization solution before spin coating for example would allow a synthesis of hydrogen peroxide sensitive PEDOT films.

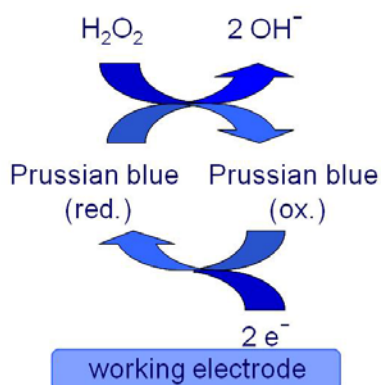


Figure 50: Reaction scheme for a hydrogen peroxide reduction at a prussian blue modified electrode in neutral media: Prussian blue mediates the reduction of hydrogen peroxide. At an adequate electrode potential the prussian blue can be renewed through reduction. The resulting reduction current is measured and used as sensor signal [Karyakin, 1999].

Prussian blue modified PEDOT layers were synthesized and used as working electrodes after integration into a simple electrochemical microfluidic test system. The sensitivity to hydrogen peroxide was investigated by amperometric detection and compared to unmodified PEDOT electrodes. The results of these initial experiments defined the electrochemical parameter for following fabricated systems.

Experimental Parameters

PEDOT layers were synthesized by spin coating 0.5 ml of a solution containing 2170 μ l CLEVIOS™ C-B50 (H.C. Starck), 670 μ l ultra-pure water ($\approx 18 M\Omega \cdot cm$), 50 μ l pyridine (Fluka, 99%), and 80 μ l CLEVIOS™ M V2 (H.C. Starck, >98%) on a $\varnothing 50$ mm TOPAS 5013 wafer at 500 rpm for 40 s. For prussian blue modified PEDOT films, 50 mg prussian blue (soluble, Fluka) were added to the solution. To speed up the polymerization and evaporate remaining solvents all substrates were baked for 5 min at $65^\circ C$. Finally the substrates were washed with deionized water and dried under a nitrogen stream. .

For bonding of the PEDOT coated wafer to an injection molded TOPAS multi-well system [Andresen, 2010], the overall PEDOT except 4 rectangular areas were removed using adhesive tape. Thermal bonding was realized at 130°C with 5 bar for 300 s.

Electrochemical experiments were carried out in freshly prepared 0.1 M potassium chloride (KCl) solution using an Ag|AgCl reference electrode placed at the inlet of the system. Cyclic voltammograms were recorded in a potential range from -0.9 V to +0.9 V at a scanrate of 50 mV/s. Amperometric measurements were done at 0 mV versus. Ag|AgCl and at a flow rate of 150 µl/min.

Preparation of the Electrochemical System

After synthesis of the PEDOT layers the areas, later used as working electrodes, were defined and separated. Four electrochemical systems were placed on each Ø50 mm TOPAS wafer. The PEDOT layer around four rectangular areas was removed (Figure 51 A). The remaining PEDOT areas (16 mm x 6 mm) were sufficient large to cover two neighboring wells of the TOPAS multi-well system used as cover (Figure 51 B). One well was later used as electrochemical cell, the other for electrical access to the PEDOT layer (Figure 51 C).

Besides a separation of the four conducting polymer areas, the removal of the PEDOT was necessary to increase the bonding strength during thermal bonding of the PEDOT carrier and the multi-well system. The fluidic system was defined by milling a channel at the bottom of the multi-well plate. The channel, 1 mm wide and 0.7 mm deep, was placed covering one well with and one without PEDOT access forming the fluidic system (Figure 51 C).

For electrochemical experiments, a Ag|AgCl reference electrode together with a platinum wire as counter electrode were inserted into the well with PEDOT access and connection to the fluidic channel (inlet) (center well in Figure 51 B and 51 C). The PEDOT inside this well was used as working electrode. Electrical access was achieved by contacting the PEDOT layer in the neighboring well through a spring loaded metal pin (well to the left in Figure 51 B and 51 C). A pump was connected to the fluidic channel, which pulled the analyte solution through the system (well to the right in Figure 51 B and 51 C).

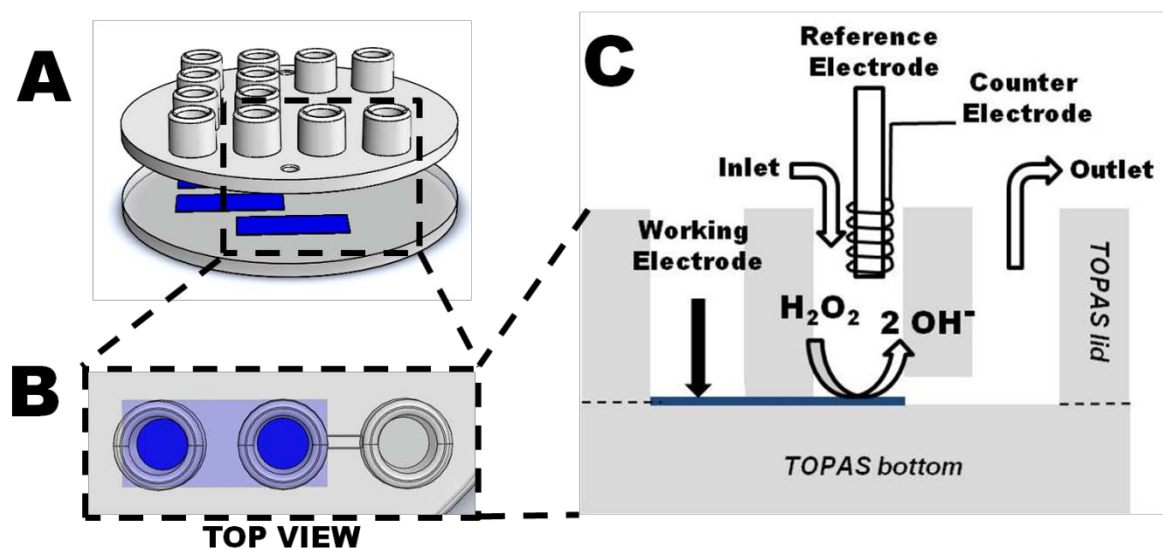


Figure 51: Fabrication process: A) Flat Ø50mm TOPAS with four rectangular PEDOT areas aligned and thermally bonded to a TOPAS multi-well systems. B) Alignment of PEDOT areas to cover wells. A fluidic channel milled into the TOPAS multi-well system connected a PEDOT covered and a non-covered well (indicated between the center and the right well) C) The electrochemical analysis proceeded by immersion of a counter and reference electrode into the PEDOT covered well with access to the fluidic channel (center well). The PEDOT layer was used as working electrode and electrically contacted by a spring loaded metal pin inserted into the well without fluidic access (well to the left)

A photograph of a final wafer with four electrochemical systems is presented in Figure 52 A. The bonding quality was analyzed by the injection of red ink into the wells. Red ink was injected into the channel through the inlet to ensure that a thermal deformation did not block the channel.

Figure 52 B presents a magnification of one electrochemical system after the injection of red ink. As seen, no red ink penetrated the interstice between the two bonded TOPAS parts. The channel between the two lower wells is highlighted by the red ink which demonstrates the operational functionality of the channel.

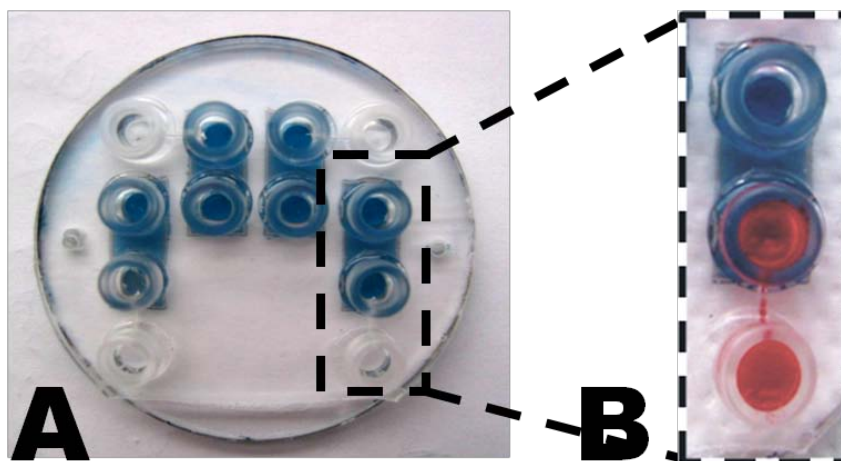


Figure 52: Thermally bonded TOPAS chip with four electrochemical systems (A) and a magnification of one system after injection of red ink to analyze the bonding quality (B).

Electrochemical Evaluation of the PEDOT/Prussian Blue Electrodes

Cyclic voltammograms were recorded at PEDOT and prussian blue modified PEDOT electrodes. The electrode area of 12.5 mm² was defined by the diameter of the well (Ø4 mm). A scan of a PEDOT as well as a Prussian blue modified working electrode is presented in Figure 53. A comparison of both tracks shows two significant redox-peaks for the prussian blue modified PEDOT electrode. The oxidation peaks of three independent prussian blue modified electrodes were determined at 395 ± 15 mV versus Ag|AgCl. The reduction peaks, important for the detection of hydrogen peroxide, were observed at -3 ± 4 mV versus Ag|AgCl.

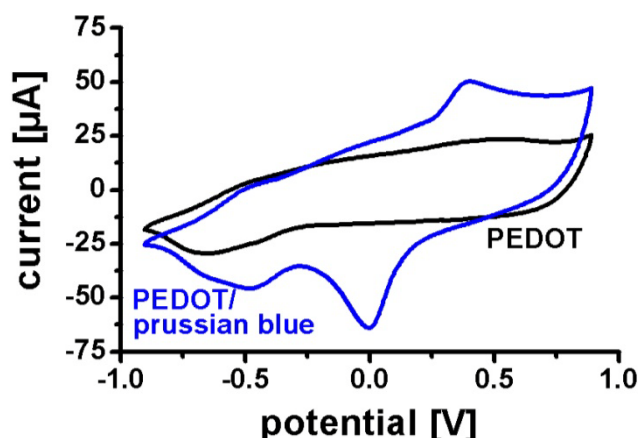


Figure 53: Cyclic voltammograms of a PEDOT (black) and a prussian blue modified PEDOT (blue) working electrode recorded in 0.1 M KCl solution at 50 mV/s using a platinum counter electrode and a Ag|AgCl reference electrode.

Due to the electrocatalytic activity of prussian blue for hydrogen peroxide reduction, the reduction potential of prussian blue (approximately 0 mV versus Ag/AgCl) was used for a following amperometric detection of different hydrogen peroxide concentrations.

Amperometric Detection of Hydrogen Peroxide

The amperometric responses of the synthesized PEDOT working electrodes to hydrogen peroxide were recorded under constant flow conditions (Figure 54 A). After establishment of a stable signal for potassium chloride, four different concentrations of hydrogen peroxide diluted in potassium chloride were subsequently injected for 200 s. Afterwards the system was rinsed with potassium chloride.

Injection of hydrogen peroxide had no significant influence on the detected current using a PEDOT working electrode (Figure 54 A, black trace), polarized at 0 V. The current was stable over the entire experiment. The prussian blue modified electrode showed an increased reduction current after injections of hydrogen peroxide (Figure 54 A, blue trace). A linear increase of the current from 0.2 μA for 1.3 mM to 7.9 μA for 43 mM hydrogen peroxide was recorded (Figure 54 B). The signal returned to the initial base current after re-injection of potassium chloride, indicating establishment of similar electrode conditions as in the beginning of the amperometric detection.

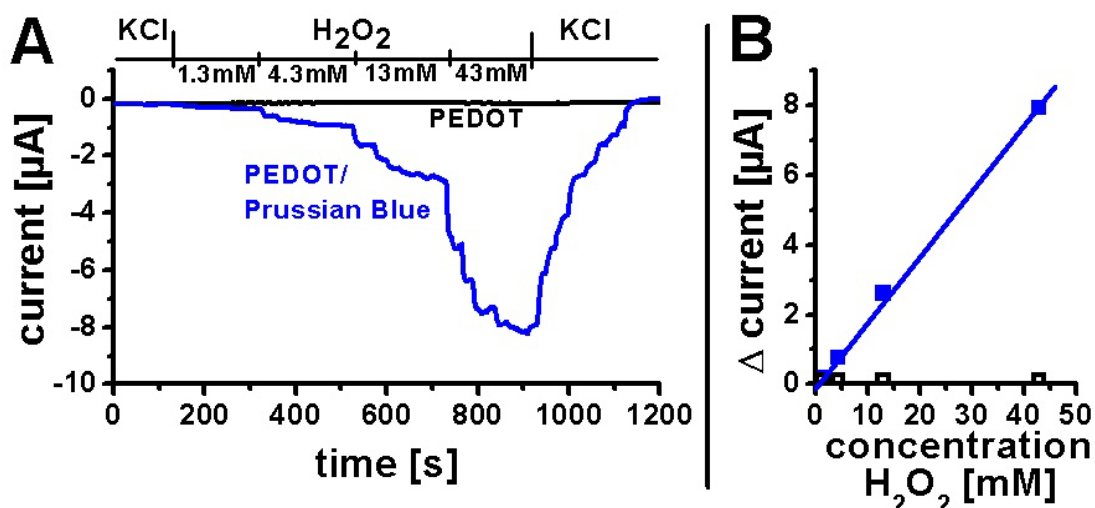


Figure 54: A) Amperometric response of a PEDOT (black) and a prussian blue modified PEDOT (blue) working electrode, polarized at 0 V versus a Ag/AgCl reference electrode, using a flow rate of 150 $\mu\text{l}/\text{min}$ and a platinum wire as counter electrode, to injections of hydrogen peroxide and B) the corresponding absolute current changes for a PEDOT electrode (black, open symbols) and a prussian blue modified PEDOT electrode (blue, closed symbols)

References

The recorded amperometric response to hydrogen peroxide demonstrates the functionality of the fabricated electrodes at a potential in the range as suggested in literature for an almost interference free detection of hydrogen peroxide [Karyakin, 1996]. Thus, hydrogen peroxide sensitive PEDOT layers can be easily fabricated by adding commercially available prussian blue to the polymerization solution before spin coating. The fabricated electrode showed a sensitivity of 0.19 $\mu\text{A}/\text{mM}$ hydrogen peroxide.

4.4 References

- [Ahuja, 2007] Ahuja, T.; Mir, I. A.; Kumar, D.; Rajesh *Biomaterials* **2007**, 28, 791-805
- [Andresen, 2010] Andresen, K. Ø.; Hansen, M.; Matschuk, M.; Jepsen, S. T.; Sørensen, H. S.; Utko, P.; Selmeczi, D.; Hansen, T. S.; Larsen, N. B.; Rozlosnik, N.; Taboryski, R. *Journal of Micromechanics and Microengineering* **2010**, 20, 055010
- [Becker and Gärtner, 2008] Becker, H.; Gärtner, C. *Analytical and bioanalytical chemistry* **2008**, 390, 89-111
- [Birnie, 2005] <http://www.coatings.rutgers.edu/KeyStages.htm>
- [CEE] CEE-Cost Effective Equipment;
<http://www.brewerscience.com/products/cee-benchtop-products/cee-technical-information/spin-coater-theory/#scept1>
- [Cosnier, 2003] Cosnier, S. *Analytical and bioanalytical chemistry* **2003**, 377, 507-20
- [Gerard, 2002] Gerard, M.; Chaubey, A.; Malhotra, B. D. *Biosensors & bioelectronics* **2002**, 17, 345-59
- [Guimard, 2007] Guimard, N. K.; Gomez, N.; Schmidt, C. E. *Biomedical Engineering* **2007**, 32, 876-921

Chapter 4: Conducting Polymers in Electrochemical Biosensors

- [Hansen, 2006] Hansen, T. S.; West, K.; Hassager, O.; Larsen, N. B. *Synthetic Metals* **2006**, *156*, 1203-1207
- [Hansen, 2007] Hansen, T. S.; West, K.; Hassager, O.; Larsen, N. B. *Advanced Materials* **2007**, *19*, 3261-3265
- [Huang, 2011] Huang, Z. H.; Handara, V. A. **2011**, *12*, 33-36
- [Illa, 2010] Illa, X.; Ordeig, O.; Snakenborg, D.; Romano-Rodríguez, A.; Compton, R. G.; Kutter, J. P. *Lab on a chip* **2010**, *10*, 1254-61
- [Karyakin, 1996] Karyakin, A. A.; Karyakina, E. E.; Gorton, L. *Talanta* **1996**, *43*, 1597-1606
- [Karyakin, 1999] Karyakin, A. A.; Karyakina, E. E.; Gorton, L. *Electrochemistry Communications* **1999**, *1*, 78-82
- [Kiilerich-Pedersen, 2011] Kiilerich-Pedersen, K.; Poulsen, C. R.; Jain, T.; Rozlosnik, N. *Biosensors and Bioelectronics* **2011**, *28*, 386-392
- [Krishnan and Sarma; 2008] Krishnan, S. and Sarma, S.; *Transactions of the North American Manufacturing Research Institute of SME* **2008**, *36*: 33-39
- [Kääriäinen, 2009] Kääriäinen, T. O.; Cameron, D. C.; Tanttari, M. *Plasma Processes and Polymers* **2009**, *6*, 631-641
- [Lee, 2005] Lee, D.-S.; Yang, H.; Chung, K.; Park, S.; Pyo, H.; Choi, C. *The 13th International Conference on Solid-State Sensors, Actuators and Microsystems, 2005. Digest of Technical Papers. TRANSDUCERS '05*. **2005**, *2*, 1284-1287
- [Mannerbro, 2008] Mannerbro, R.; Ranlof, M.; Robinson, N.; Forchheimer, R. *Synthetic Metals* **2008**, *158*, 556-560

References

- [Palmisano, 1993] Palmisano, F. *Biosensors and Bioelectronics* **1993**, 8, 393-399
- [Rozlosnik, 2009] Rozlosnik, N. *Analytical and bioanalytical chemistry* **2009**, 395, 637-45
- [Sarma, 2009] Sarma, A. K.; Vatsyayan, P.; Goswami, P.; Minter, S. D. *Biosensors & bioelectronics* **2009**, 24, 2313-22
- [Setti, 2007] Setti, L.; Fraleoni Morgera, A.; Mencarelli, I.; Filippini, A.; Ballarin, B.; Di Biase, M. *Sensors and Actuators B: Chemical* **2007**, 126, 252-257
- [Vo-Dinh, 2000] Vo-Dinh, T.; Cullum, B. *Fresenius' journal of analytical chemistry* **2000**, 366, 540-551
- [Wang, 2008] Wang, J. *Chemical reviews* **2008**, 108, 814-25

Chapter 5

Fabrication of All-Polymer Electrochemical Sensors

5.1 Fast Prototyping of Conducting Polymer Microelectrodes using Resistance-Controlled High Precision Drilling

5.1.1 Introduction

The availability of stable and processable highly conducting polymers has recently enabled the fabrication of low-cost all-polymer chips for electrochemical analysis with integrated polymer microelectrodes.

Microelectrodes are increasingly preferred over macroelectrodes due to a faster response time and better signal-to-noise ratios [Heinze, 1993; Stulik, 2000]. In contrary, the low currents associated with individual microelectrodes due to the small electrode dimension are a disadvantage. Arranging microelectrodes in arrays increases the signal while retaining the electrochemical advantages of a single electrode. This, however, is only valid for an appropriate array design. Electrodes arranged too closely might interfere with each other, e.g. due to overlapping diffusion radii [Stulik, 2000]. A number of simulation tools are available for the analysis of array configurations in order to avoid interference between two neighboring electrodes.

Fast prototyping strategies are necessary to confirm simulated results with real systems before an electrode array design can be mass produced for a practical applications, in particular when using conducting polymer electrodes where the electrode material itself can contribute to the measurement [Heinze, 2010].

This chapter describes a fast prototyping strategy to fabricate arrays of circular polymer microelectrodes using a desktop milling machine. Microelectrodes were fabricated by drilling through an insulating layer of TOPAS 5013 to an underlying layer of PEDOT. Single electrodes and 3 x 3 electrode arrays with electrode diameters down to 30 μm were reproducibly fabricated. Electrochemical functionality was demonstrated by recording the amperometrical response to potassium ferrocyanide after integration of the electrodes into an electrochemical cell. Finally, experimental results were verified against a finite element modeling of the microelectrode arrays.

5.1.2 Fabrication of Circular-Electrodes

Microelectrodes were fabricated by stepwise drilling through an electrically insulating TOPAS layer, about $7.5\ \mu\text{m}$ in thickness, to an electrically conducting, $3.5\ \mu\text{m}$ thick PEDOT layer below (Figure 55). The process proceeded in steps of approximately $0.5\ \mu\text{m}$ using a desktop computer controlled milling machine (Mini-Mill/3PRO, Minitex). To avoid unnecessary heating, the drilling process was realized at the lowest possible rotation speed of 500 rpm. To achieve planar electrode surfaces, flat-end milling tools with $30\ \mu\text{m}$ or $100\ \mu\text{m}$ in diameter were used for the drilling process.

The end-point of the drilling process was determined by a sharp decrease in electrical resistance from infinity ($> 40\ \text{M}\Omega$) to approximately $20\ \text{k}\Omega$ upon physical contact between the rotating tool and the PEDOT layer. After contact, one additional drilling step of approximately $0.5\ \mu\text{m}$ was performed to ensure complete removal of the TOPAS coating above the electrode area.

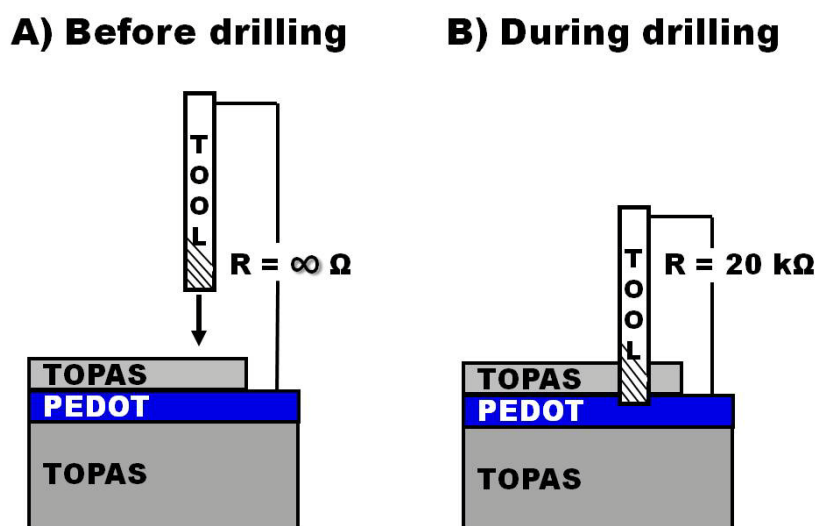


Figure 55: The resistance-controlled drilling process: Drilling proceeded through the insulating cover layer until physical contact between tool and conducting polymer. The contact was detected by a drop of the electrical resistance from infinity to approximately $20\ \text{k}\Omega$.

Characterization of Single Electrodes

Geometry and dimensions of the electrodes were evaluated by SEM. Analyzed electrodes had a circular shape of $94.8 \pm 0.6 \mu\text{m}$ and $32.2 \pm 0.5 \mu\text{m}$ in diameter for $\text{Ø}100 \mu\text{m}$ and $\text{Ø}30 \mu\text{m}$ electrodes, respectively (Figure 56). Circular shape of the holes clarifies that tool and holder were well aligned and the tool was drilling balanced. Misaligned or imbalanced tools would have caused elliptical shape of the holes.

The machined surface appears to be very rough. However, a good accordance between experimental results and results obtained from a finite element model (Chapter 5.1.4) led to the conclusion that the obtained surface roughness did not strongly influence the predetermined electrode area.

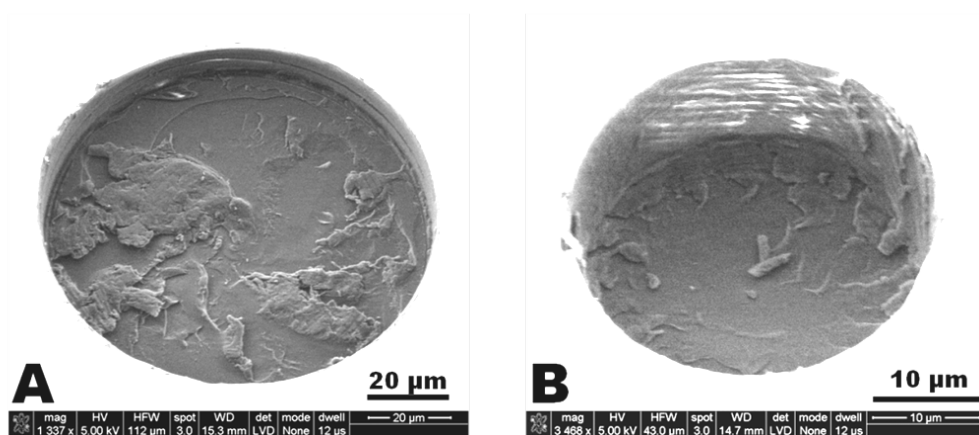


Figure 56: SEM image of a single A) $\text{Ø}100 \mu\text{m}$ and B) $\text{Ø}30 \mu\text{m}$ PEDOT electrode at the bottom of a drilled hole (30° tilted). The insulating TOPAS surface appears as bright, due to electrostatic charging of the non-conducting TOPAS layer during imaging.

The complete removal of the insulating TOPAS layer at the electrode area was verified by SEM. Grounding of the PEDOT layer prevented excessive electrostatic charging of the electrode surfaces during imaging and allowed therefore a clear differentiation compared to charged TOPAS residues. TOPAS residues appeared as charged areas (bright) on the conductive electrode surface (grey) as observed for a single electrode presented in Figure 57.

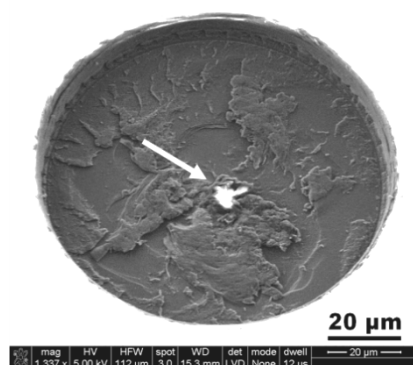


Figure 57: SEM image of a Ø100 µm PEDOT electrode at the bottom of a drilled hole (30° tilted). The inserted arrow highlights TOPAS residues from the insulating layer at the electrode area.

Fabrication of Microelectrode Arrays

Arrays of Ø30 µm and Ø100 µm electrodes, respectively, were produced with center-to-center spacings of either 130 µm or 300 µm. The microelectrodes were fabricated using resistance-controlled microdrilling as described above. The control software of the milling machine was employed to control spacing and separation of the multiple electrode arrays on each TOPAS/PEDOT-coated substrate. Milling of a single 3 x 3 array typically lasted about 10 minutes.

Optical dark-field micrographs of fabricated Ø100 µm electrode arrays with center-to-center spacing of 130 µm and 300 µm are presented in Figure 58 A and 58 B, respectively. Corresponding electrode arrays of Ø30 µm electrodes are presented in Figure 58 C and 58 D. For Ø100 µm electrodes a center-to-center spacing of 130 µm corresponds to an edge-to-edge separation of 30 µm. A reduction of the spacing below 30 µm resulted in a deformation of the insulating TOPAS layer in between caused by too high friction during the drilling process. Thus an edge-to-edge separation of 30 µm was the minimum possible electrode distance at which electrodes could be fabricated routinely.

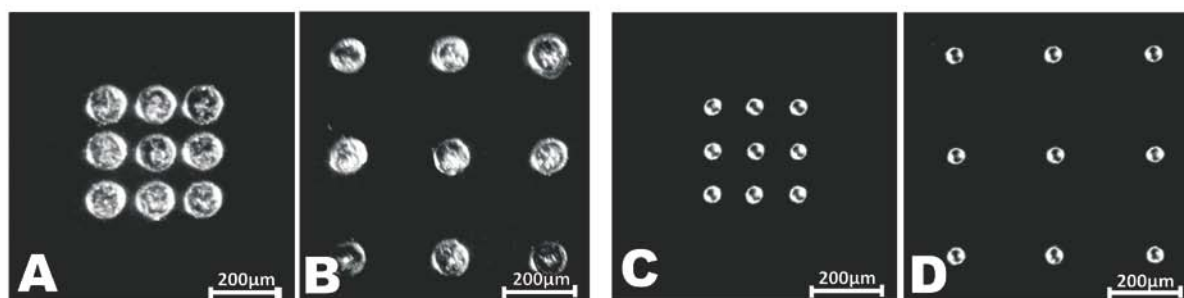


Figure 58: Dark-field micrographs of fabricated 3 x 3 microelectrode arrays with Ø100 µm (A + B) and Ø30 µm (C + D) electrodes arranged with center-to-center spacings of 130 µm (A + C) and 300 µm (B + D).

5.1.3 Bonding

The fabricated microelectrode arrays were bonded to an injection molded TOPAS multi-well system [Andresen, 2010] using silicone based adhesive tapes. After alignment of both parts a pressure of 2.5 bar for 600 s at 50°C was applied to achieve a stable bond. As discussed later, each well was used as single electrochemical cell after immersion of a reference electrode and a counter electrode (Figure 59).

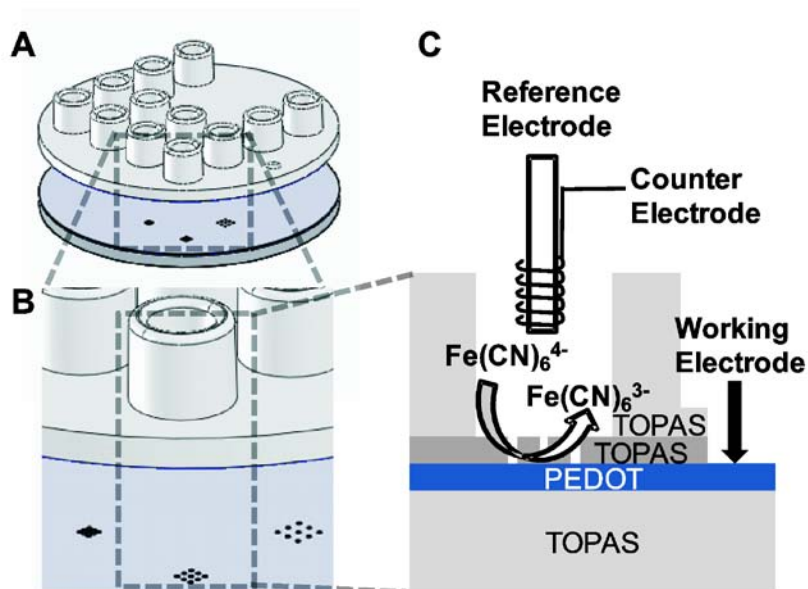


Figure 59: Bonding process: Multiple microelectrode arrays with different spacings were bonded to an injection molded TOPAS multi-well system (A). The following electrochemical analysis proceeded by immersion of a platinum wire as counter electrode and a Ag|AgCl reference electrode into the well while contacting the PEDOT layer as working electrode (B + C).

5.1.4 Finite Element Modelling of Electrode Arrays

The four microelectrode arrays were modeled in a 3D solution environment using the finite modeling package COMSOL 4 (COMSOL AB, Stockholm). The electrodes were modeled as perfect sinks of the solute at an otherwise mass transport insulated “floor” of a $2 \times 2 \times 2 \text{ mm}^3$ simulation box. The solute concentration at the four side walls and at the ceiling was fixed to be at the initial concentration. The experimental conditions were mimicked by modeling the $\text{Ø}100 \text{ }\mu\text{m}$ electrodes using 1 mM solute and the $\text{Ø}30 \text{ }\mu\text{m}$ electrodes using 5 mM solute (diffusion constant of $8 \times 10^{-10} \text{ m}^2/\text{s}$ [Kakihana, 1981]). Time dependent conditions up to 90 s were investigated. The molar flux across the microelectrodes was converted to a current given that one electron is transferred for the reaction of each ferrocyanide ion.

The resulting solute concentration of the redox active species after 90 seconds of analysis is shown in Figure 60. Both sets of $30 \text{ }\mu\text{m}$ electrodes behave largely as independent electrodes with hemispherical concentration gradient profiles. In contrast, the closely spaced $100 \text{ }\mu\text{m}$ electrodes (center-to-center distance $130 \text{ }\mu\text{m}$) develop an almost planar diffusion profile above the center electrode. The resulting reduced redox kinetics mainly affect the center electrode of this 3×3 array, i.e. one out of 9 electrodes. In square arrays containing more electrodes, the fraction of electrodes affected will obviously be higher. Increasing the electrode spacing to $300 \text{ }\mu\text{m}$ reduces the effect, with each electrode largely acting as an individual $\text{Ø}100 \text{ }\mu\text{m}$ electrode.



Figure 60: Finite element modelling of the redox active species concentration for $\text{Ø}100 \text{ }\mu\text{m}$ (A + B) as well as $\text{Ø}30 \text{ }\mu\text{m}$ (C + D) electrode arrays with $130 \text{ }\mu\text{m}$ (A + C) and $300 \text{ }\mu\text{m}$ (B + D) center-to-center spacings, after running amperometric measurements for 90 s . The graphs are presented as cross-sectional views through the three center electrodes of each array (dark red: initial concentration; black: zero concentration).

Modeling of the electrochemical kinetics shows a much slower approach to steady state for $\text{Ø}100\ \mu\text{m}$ electrodes (Figure 61 A) than for the $\text{Ø}30\ \mu\text{m}$ electrodes (Figure 61 B). For both electrode dimensions (Figure 61), a spacing of $130\ \mu\text{m}$ (trace “b”) is observed to yield a significantly smaller current at all time points compared to a spacing of $300\ \mu\text{m}$ (trace “c”). Steady state currents (after 90 s) for the dense arrangements (center-to-center spacing of $130\ \mu\text{m}$) of $66\ \text{nA}$ and $112\ \text{nA}$ were calculated for $\text{Ø}100\ \mu\text{m}$ and $\text{Ø}30\ \mu\text{m}$ electrode arrays, respectively. Significantly higher currents of $102\ \text{nA}$ and $126\ \text{nA}$ for $\text{Ø}100\ \mu\text{m}$ and $\text{Ø}30\ \mu\text{m}$ electrodes, respectively, were predicted for widely spread arranged arrays (center-to-center spacing of $300\ \mu\text{m}$).

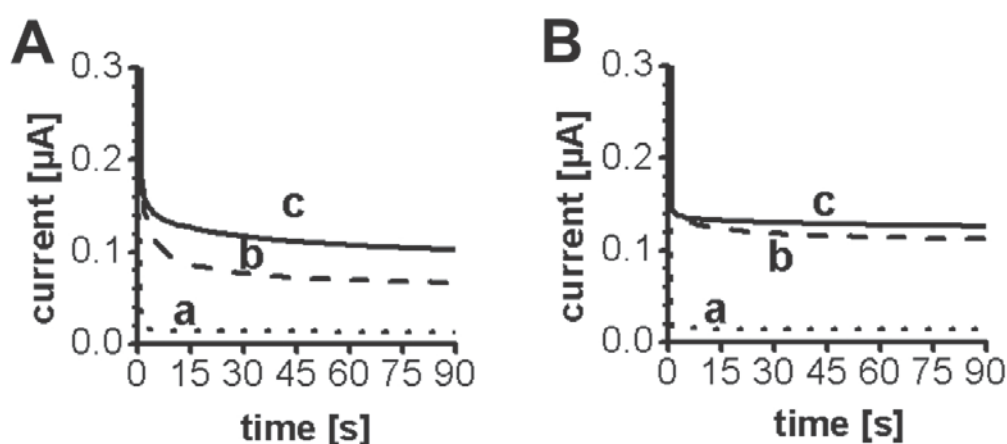


Figure 61: Comparison of simulated amperometric results for $\text{Ø}100\ \mu\text{m}$ (A) and $\text{Ø}30\ \mu\text{m}$ (B) electrodes. In both diagrams the trace “a” represents a single electrode, while traces “b” and “c” represent 3×3 arrays with spacings of $130\ \mu\text{m}$ and $300\ \mu\text{m}$, respectively.

5.1.5 Electrochemical Analysis of Microelectrodes

Experimental Parameters

For electrochemical analysis a Ag|AgCl|3M NaCl reference electrode and a platinum counter electrode were integrated into the cavity above the corresponding electrode array. Electrical access of the PEDOT electrodes was achieved by connecting the overall PEDOT layer via the non-isolated area (Figure 59). Electrochemical experiments were carried out in freshly prepared aqueous solutions of 0.1 M KCl (Sigma-Aldrich, >99%) containing potassium ferri-/ferrocyanide (Sigma-Aldrich). Analysis of $\text{\O}100\ \mu\text{m}$ electrodes used an initial ferri-/ferrocyanide concentration of 1 mM (of each species), while 5 mM (of each species) was used on $\text{\O}30\ \mu\text{m}$ electrodes to increase the signal intensity. To avoid bubbles on the electrodes, cells were rinsed with an aqueous solution having low surface tension (40 wt% ethanol/water [Vazquez, 1995]) followed by rinsing three times with Millipore water ($\leq 18\ \text{M}\Omega\text{cm}$) before injecting KCl solution

Amperometric Response to Potassium Ferrocyanide: Steady State Current

The amperometric response of the electrode arrays to potassium ferrocyanide within the first 90 s was recorded. The experimental results display a similar trend as predicted by the finite element analysis: The dense arrangement of $\text{\O}100\ \mu\text{m}$ electrodes (center-to-center spacing of $130\ \mu\text{m}$) caused a reduced steady state current of $77 \pm 22\ \text{nA}$ (simulation: 66 nA) compared to $105 \pm 8\ \text{nA}$ (simulation 102 nA) for largely independently acting electrodes with a $300\ \mu\text{m}$ spacing (Figure 62 A).

This is in agreement with the planar diffusion field above a dense arrangement of $\text{\O}100\ \mu\text{m}$ electrodes (center-to-center spacing of $130\ \mu\text{m}$), presented in Figure 60. Overlapping diffusion radii of the single electrodes caused a reduced amperometric current for the whole array arrangement. An increased center-to-center spacing of $300\ \mu\text{m}$ resulted in largely independent acting electrodes and therefore in higher steady state currents.

Interference of the diffusion radii of the electrodes was also found for $\text{\O}30\ \mu\text{m}$ electrode arrays. Steady state currents of $97 \pm 17\ \text{nA}$ (simulation 112 nA) and $128 \pm 10\ \text{nA}$ (simulation: 126 nA) for arrays with spacings of $130\ \mu\text{m}$ and $300\ \mu\text{m}$, respectively, were recorded (Figure 62 B).

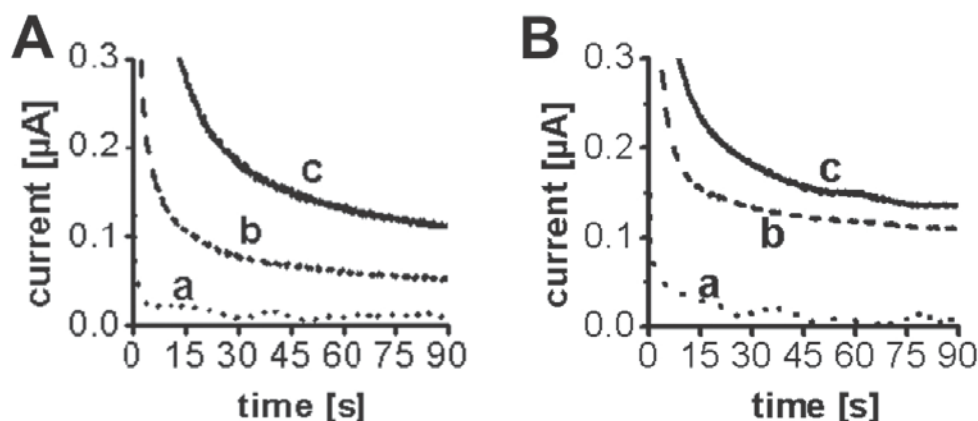


Figure 62: Comparison of experimental amperometric results for $\text{Ø}100\ \mu\text{m}$ (A) and $\text{Ø}30\ \mu\text{m}$ (B) electrodes. In both diagrams the trace “a” represents a single electrode, while traces “b” and “c” represent 3×3 arrays with spacings of $130\ \mu\text{m}$ and $300\ \mu\text{m}$, respectively.

Amperometric Response to Potassium Ferrocyanide: Kinetics

The experimentally determined rate of approach to steady state is much slower than the modeled kinetics, even for single electrodes (Figure 61 and 62, traces “a”). This discrepancy in time can be attributed to the electrochemical activity of the PEDOT electrodes themselves: The potential step applied to initiate the amperometric measurement results in partial oxidation of the PEDOT layer to establish a new equilibrium condition [Heinze, 2010]. The latter process may last several minutes and will be overlaid on the response from the redox active species in solution.

The amperometric contribution of potassium ferrocyanide can be extracted by forming the difference between recorded time dependent currents for pure potassium chloride and ferrocyanide. The resulting current for the dissolved redox active species approaches steady state within a few seconds, as expected from modeling (Figure 63, trace “d”).

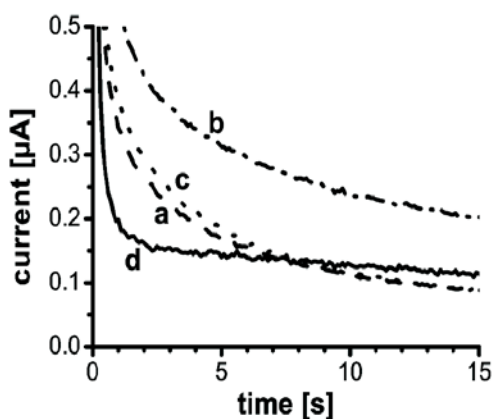


Figure 63: Amperometric measurements on a 3×3 array of $\text{Ø}100\ \mu\text{m}$ microelectrodes with a spacing of $300\ \mu\text{m}$. Traces (a) through (c) are measured sequentially using (a) $0.1\ \text{M}$ potassium chloride solution, (b) $1\ \text{mM}$ ferro/ferricyanide in $0.1\ \text{M}$ potassium chloride, and (c) $0.1\ \text{M}$ potassium chloride. Trace (d) is the calculated difference of (a) and (b).

Analysis of the extracted current contribution after 15 s resulted in a steady state current for Ø100 µm electrode arrays of 72 ± 2 nA as well as 104 ± 11 nA with spacings of 130 µm and 300 µm, respectively. This is in good agreement with 66 nA and 102 nA predicted by the simulation of the small and large spaced arrays, respectively. The same tendency was found for Ø30 µm electrode arrays. Currents of 113 nA and 140 ± 14 nA were calculated for arrays with spacings of 130 µm and 300 µm, respectively, and compared to predicted currents of 112 nA and 126 nA, respectively.

5.1.6 Summary

Resistance-controlled microdrilling through a protective insulating polymer layer is a successfully applied method for prototyping of microelectrode arrays in the conducting polymer PEDOT with minimum demonstrated electrode widths and separations of 30 µm. Multiple microelectrode arrays bonded to a polymer multi-well system were analyzed individually by amperometry, and the general trends at steady state agreed with results obtained from finite element modeling of such arrays. However, a significant discrepancy was observed for the kinetics of the manufactured electrodes, with much slower approach to steady state than predicted. Subtraction of the contribution from the PEDOT electrode led to excellent agreement of time scales and current levels between the models and the experiments. These results demonstrate that fast prototyping of real microelectrode arrays is of great importance for designing electrochemical analytical systems that use conducting polymer microelectrodes.

5.1.7 References

- [Andresen, 2010] Andresen, K. Ø.; Hansen, M.; Matschuk, M.; Jepsen, S. T.; Sørensen, H. S.; Utko, P.; Selmeczi, D.; Hansen, T. S.; Larsen, N. B.; Rozlosnik, N.; Taboryski, R. *Journal of Micromechanics and Microengineering* **2010**, *20*, 055010
- [Heinze, 1993] Heinze, J. *Angewandte Chemie International Edition in English* **1993**, *32*, 1268-1288
- [Heinze, 2010] Heinze, J.; Frontana-Urbe, B. a; Ludwigs, S. *Chemical reviews* **2010**, *110*, 4724-71
- [Kakihana, 1981] Kakihana, M.; Ikeuchi, H.; Sato, G. *Journal of Electroanalytical Chemistry* **1981**, *117*, 201-211
- [Stulik, 2000] Stulik, K.; Amatore, C.; Holub, K.; Marecek, V.; Kutner, W. *Pure and Applied Chemistry* **2000**, *72*, 1483-1492
- [Vazquez, 1995] Vazquez, G.; Alvarez, E.; Navaza, J. M. *Engineering* **1995**, *40*, 611-614

5.2 Fabrication of an All-Polymer Electrochemical Microfluidic System using a One-Step Microdrilling Procedure

5.2.1 Introduction

Microelectrodes are widely used as transducers in electrochemical sensors. The most common types are circular, ring, and band shaped microelectrodes [Heinze, 1993]. Tubular electrodes are a special type of band electrodes, as the length of electrodes is much larger than their width [Engblom, 1996]. In addition to the advantages of the common microelectrodes such as fast establishment of a steady-state signal, enhanced mass transport at the electrode boundary, and an increased signal-to-noise ratio [Stulik; 2000], tubular electrodes are well suited for integration into a microfluidic system. Since they are placed inside the channel sidewall, tubular electrodes do not disturb the flow of the analyte.

Even though the tubular electrodes have been known for a long time, a commercial mass fabrication of these electrodes was not successfully realized. The main reason for this is the lack of a reproducible fabrication method for this type of electrodes. The challenge of reproducible fabrication is reflected in the small amount of available publications. Over the years, only few research groups have published their fabrication methods but usually with unknown or inhomogeneous electrode dimensions. A deformation of the electrode material was observed during or after the fabrication and caused irregularities, independent of the fabrication method (e.g. drilling [Corti, 1994], laser ablation, or punching [Konash, 2009]) and electrode material (e.g. gold [Corti, 1994], carbon paste [Konash, 2009], platinum [Kovach, 1985]).

This chapter presents a fabrication method which allows a reproducible fabrication of tubular electrode arrays. The electrodes were fabricated by microdrilling through a conductive layer of PEDOT spin coated on a TOPAS foil and insulated by polystyrene (PS). Arrays of ten $\text{\O}100\ \mu\text{m}$ tubular electrodes were fabricated with an average electrode height of $370 \pm 60\ \text{nm}$. The electrochemical response of different arrays towards potassium ferrocyanide showed high consistency. Finally, the potential of these electrodes to act as a glucose sensor was demonstrated by the detection of hydrogen peroxide as a side product of the enzyme catalyzed oxidation of glucose.

5.2.2 Fabrication Principle

Microelectrodes were fabricated by drilling through a TOPAS 5013 foil (\varnothing 6cm) which was coated from both sides with a layer of polystyrene (PS), followed by a layer of PEDOT. The PS layers between the TOPAS foil and the PEDOT layers were required to increase the adhesion between the TOPAS foil and the PEDOT. An additional PS layer electrically insulated the upper PEDOT layer. Drilling through the whole assembly resulted in a cylindrical drilling shaft with a tubular PEDOT electrode integrated in the shaft sidewall and a large planar electrode placed at the end of the shaft (Figure 64).

To determine the necessary drilling depth, resistance-controlled microdrilling (Chapter 5.1) was applied. A drop in the electrical resistance between the drill and the lower PEDOT layer from infinity to about 20 kOhm indicated a completed drilling through the entire assembly.

Advantageously, a complete electrochemical system was defined by a single drilling step. The drilling shaft acted as a microfluidic channel. The arrangement of the assembly allowed a simultaneous integration of a tubular working electrode and a large planar counter electrode during the fabrication process. Electrical access to the working electrode was realized by application of an insulating PS layer partly on the upper PEDOT layer.

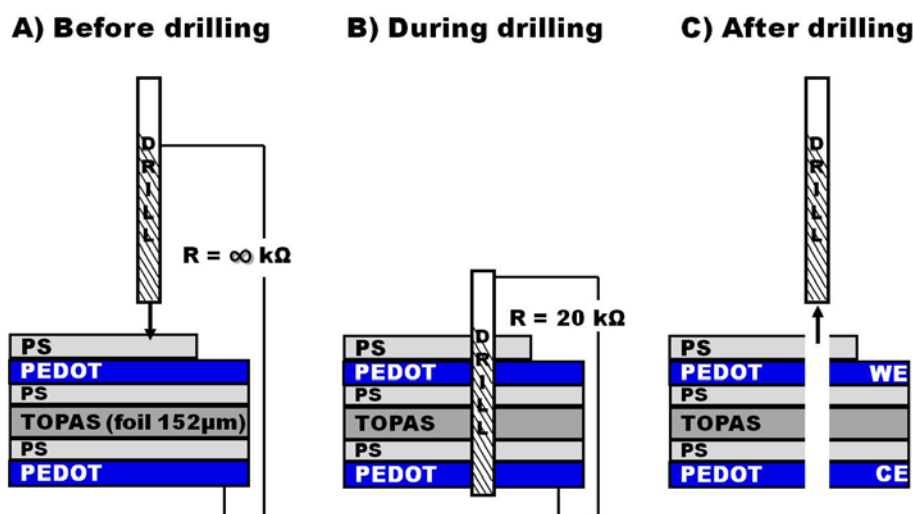


Figure 64: Fabrication process: A) Both sides of a TOPAS foil were spin coated with a layer of polystyrene and PEDOT. An additional a layer of polystyrene was applied on one side in order to electrically insulated the underlying PEDOT layer. B+C) Drilling a hole through the assembly resulted in a cylindrical shaft with a tubular PEDOT electrode in the sidewall as well as a planar PEDOT electrode at the end. Due to bending of the foil during the drilling process, monitoring of the electrical resistance between the drill and the lower PEDOT layer was necessary to guarantee a successful drilling of a through hole. The resistance dropped from infinity to approximately 20 kOhm upon physical contact between the drill and the lower PEDOT layer, indicating a complete through hole.

5.2.3 Design of Spin Coating Chuck

The described assembly of a coated TOPAS 5013 foil with a PS/PEDOT on one side and a PS/PEDOT/PS modification on the other side was fabricated by spin coating. Due to mechanical instability of the 150 μm thick TOPAS foil a mechanical support for the spin coating process was developed. Different chuck designs, all based on $\text{\O}58$ mm PMMA discs, were investigated.

Chuck with Four Center Holes for Vacuum Supply

A PMMA disc was modified with four circular arranged $\text{\O}0.5$ mm through holes at the disc center. The holes served as vacuum supply by transmitting the vacuum from the spin coater through the PMMA disc to the foil which was placed on top (see Figure 65, only without the channels).

The vacuum distributed through the holes was not sufficient to hold the foil in place during the spin coating. In most cases the foil detached making homogeneous coatings impossible.

Chuck with Four Vacuum Channels

The PMMA chuck design was modified by adding four vacuum channels to the four circular holes (Figure 65 A and 65 B). Thus, the vacuum was applied at four channels (arranged in a cross) across the foil.

The modification with the four vacuum channels increased the adhesion of the foil considerably. No foils detached during the spin coating process. However, the vacuum along the channels was too strong leading to inhomogeneous PEDOT coatings (Figure 65 C).

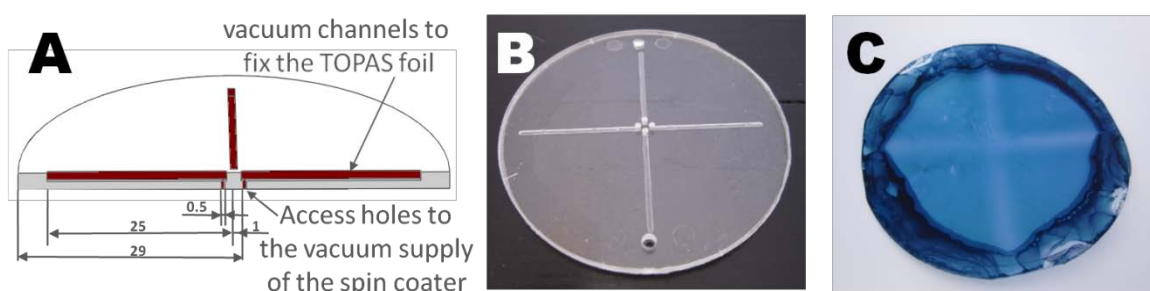


Figure 65: A) Sketch of the fabricated chuck with four open vacuum channels (red) to attach the TOPAS foil during spin coating, B) Photograph of the fabricated PMMA chuck, and C) coated TOPAS foil with polymerized PEDOT film. Chuck marks are visible as bright blue lines across the foil.

Chuck with Four Straight and Four Circular Vacuum Channels

To distribute the vacuum more evenly and thereby reduce the influence of the vacuum, four additional circular channels were introduced to the chuck design. The circular channels were connected to the previous straight channels (Figure 66 A and 66 B).

The chuck marks in the synthesized PEDOT layer were significantly reduced but still visible. A magnification of a synthesized PEDOT film with chuck marks is presented in Figure 66 D.



Figure 66: A) Sketch of the fabricated chuck with four straight and four circular vacuum channels (red) to attach the TOPAS foil during spin coating, B) Photograph of the fabricated spin coating chuck, C) coated TOPAS foil with polymerized PEDOT film, and D) magnification of a part of the polymerized PEDOT layer. The magnification is presented in grayscale for a better visualization of the chuck marks (bright areas).

Chuck with a Circular Vacuum Support at the Rim

All chuck designs described so far resulted in inhomogeneous PEDOT layers. Therefore, a design was developed which applied vacuum only along the rim. Chuck marks at the rim should not disturb the electrode fabrication. The rim can be cut off if the foil diameter is larger than the diameter necessary for further processing.

The fabricated chuck consisted of two parts: a) a bottom part with four vacuum channels and b) a top part bonded to the bottom part with four through holes close to the rim and a 0.7 mm wide circular channel. The through holes established access to the underlying vacuum channels (bottom part). The vacuum was applied to the foil via the 0.7 mm wide channel along the rim (Figure 67).

This chuck design allowed the synthesis of homogeneous PEDOT coatings across the foil center. Before spin coating the center of the foil was flattened and pressed to the chuck using a roll. This was necessary to obtain a homogenous surface and to avoid a lifting of the foil center. A typical double sided coated foil is presented in Figure 67 C. Inhomogeneous areas were observed only at the rim, which were removed during further processing.

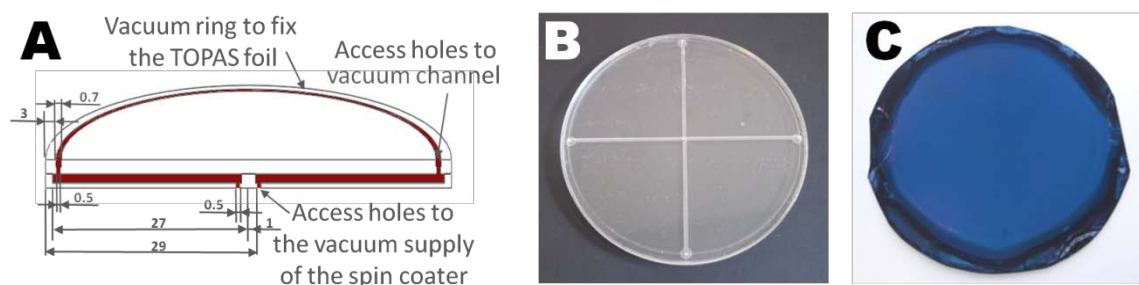


Figure 67: A) Sketch of the fabricated chuck with internal vacuum channels which guide the vacuum to the rim of the chuck (red). The foil was fixed at the rim through an open circular vacuum channel which was connected through holes with the internal vacuum channels. B) Photograph of the fabricated spin coating chuck, and C) double sided coated TOPAS foil with polymerized PEDOT film.

5.2.4 Coherence of the PEDOT/TOPAS Assembly

Through hole drilling performed on TOPAS foils spin coated with a layers of PEDOT and TOPAS (no PS as adhesion promoter) resulted in a delamination of the PEDOT layer during drilling. The delamination was visible in an optical microscope as grey zone around the drilled holes (Figure 68).

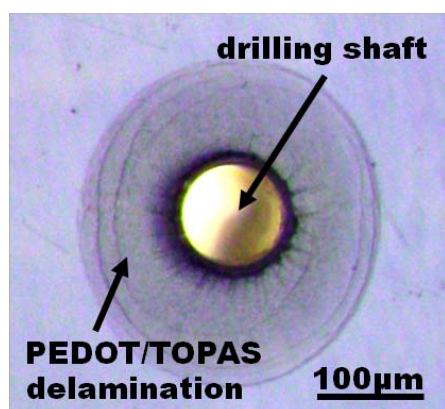


Figure 68: Micrograph of a hole drilled through a TOPAS foil/PEDOT/TOPAS assembly. The slightly grey elliptical area around the drilled hole indicates a delamination of the assembly.

Polystyrene as Adhesion Promoter between PEDOT and TOPAS

Attempts to remove spin coated PEDOT layers from a polystyrene (PS) bulk substrate using adhesive tape showed a high adhesion of PEDOT to PS. Therefore, spin coating of a PS layer before the PEDOT layer could increase the adhesion of the PEDOT to the foil. PS dissolved in toluene and tetrahydrofuran could cause a solvation of the TOPAS foil surface due to the presents of solvents resulting in an entanglement of PS and TOPAS chains before and during the solidification process. Thus, a spin coated PS layer on the TOPAS foil might be well suited as adhesion promoter between PEDOT and TOPAS.

Assemblies were prepared by spin coating a TOPAS foil initially with a layer of PS followed by a layer of PEDOT. PS also replaced TOPAS as insulating material on top of the PEDOT layer. The high fragility of PS foils prevented the replacement of the TOPAS as carrier material, even though it would have simplified the coating process.

Drilling of through holes into the PS assisted assemblies was realized without any visible delamination (Figure 69 A). The area around the holes was homogenous and free of artifacts. A thin dark ring around the hole is visible in the micrograph which indicates a deformation of the top material during the drilling process.

Remaining “lids” observed at the opposite end of the drilling shaft (Figure 69 B) could be removed with compressed nitrogen. However, for later fabricated systems the “lids” were kept, since their removal increased the risk of damaging the assembly.

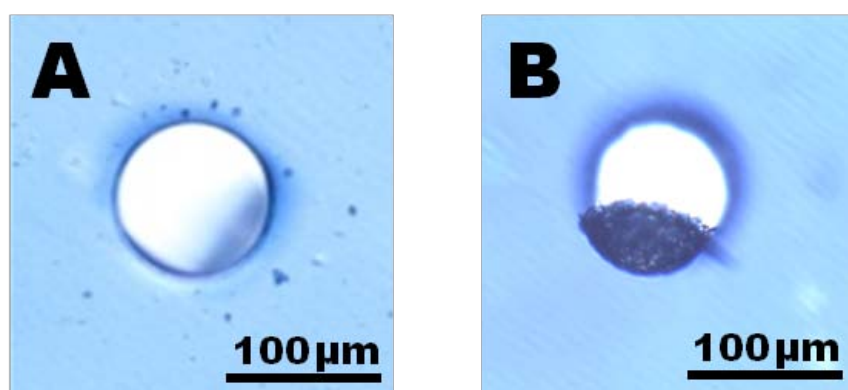


Figure 69: Micrographs of a drilled $\text{\O}100\ \mu\text{m}$ hole through a TOPAS foil/PS/PEDOT/PS assembly A) from the top and B) from the bottom. A remaining “lid” from the drilling process is visible.

5.2.4.1 Experimental Parameters – Layer Assembly Preparation

A PS layer was applied onto a ethanol-cleaned Ø6 cm round TOPAS foil (TOPAS 5013, Topas Advanced Polymers, thickness: 150 µm) by spin coating 1 ml of a 5 mg/ml PS solution, dissolved in 1:1 (vol.) tetrahydrofuran/toluene at 1000 rpm for 300 s (later reduced to 60 s) using an acceleration of 500 rpm/s. Immediately after the spin coating a layer of the conducting polymer poly(3,4-ethylenedioxythiophene) was synthesized on top of the PS layer by spin coating 0.9 ml of a freshly-prepared solution containing 2170 µl CLEVIOS™ C-B50 (H.C. Starck), 670 µl ultra-pure water (≥ 18 MΩcm), 50 µl pyridine (Fluka, 99%), and 80 µl CLEVIOS™ M V2 (H.C. Starck, >98%) at 500 rpm for 90 s with an acceleration of 500 rpm/s. Substrates were baked at 65°C for 15 min to increase the polymerization rate and to evaporate remaining solvents, washed with deionized water, and dried in a stream of nitrogen. The same procedure was repeated for the backside of the foil. The backside PEDOT layer was structured by laser ablation in order to separate rectangular PEDOT areas for electrode drilling. Finally, an additional PS layer (passivation layer) was applied on top of the structured PEDOT: 1 ml of a 0.1 g/ml PS solution dissolved in a 1:1 (vol.) tetrahydrofuran/toluene mixture was applied on one half of the foil (decentered) before spin coating started. During spin coating at 750 rpm for 60 s using an acceleration of 250 rpm/s the PS mixture got distributed only at a part of the foil while the other was left uncovered. The uncovered PEDOT area was used for electrical access to the electrodes.

The height of the insulating PS layer of about 26 µm was determined by using resistance-controlled microdrilling. Instead of using a drill, a flat-end mill was used to achieve a higher precision. A drill results in a conical bottom, which would make a precise PS thickness determination impossible. The resistance between the tool and the upper PEDOT layer was measured. The drilling process proceeded from the surface of the insulating PS layer down to the PEDOT layer. The drilling process was stopped at contact between tool and PEDOT layer (determined by a resistance drop). A profile of the resulting hole with the PEDOT layer at bottom is presented in Figure 70.

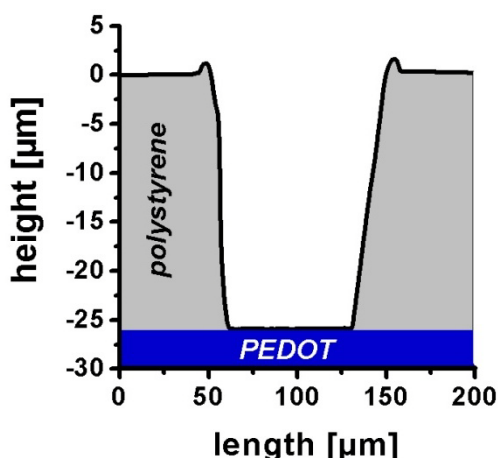


Figure 70: Profile of a drilling shaft through the insulating polystyrene (sidewalls) layer to the underlying PEDOT layer (bottom). The drilling was performed using resistance-controlled microdrilling.

5.2.5 Drilling of Electrode Arrays

Prepared layer assemblies, 6 cm in diameter, were bonded to an Ø5 cm multi-well system [Andresen, 2010] using silicone based adhesives tapes (Figure 71). The transfer was necessary to achieve better mechanical stability of the foils for drilling as well as for fluidic connection of the final electrochemical system. Inhomogeneous PEDOT areas at the rim were cut off to achieve a homogeneous bond and to ensure electrical disconnection of the PEDOT layers. PEDOT layers could have been connected during synthesis.

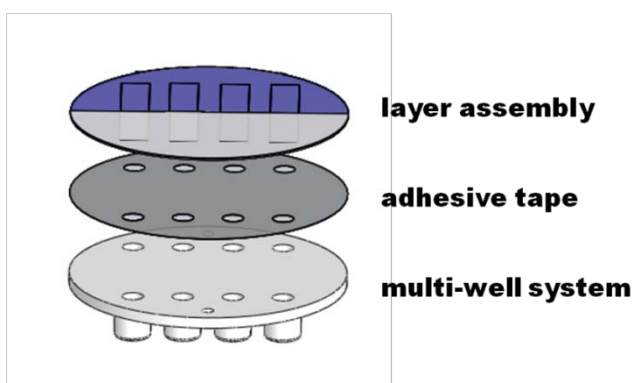


Figure 71: Spin coated TOPAS foils with a PS/PEDOT on one and a PS/PEDOT/PS modification at the opposite side were bonded to a multi well system using silicone based adhesive tapes.

Holes were drilled into the foils starting from the PS passivation layer into underlying wells using a Ø100 µm drill. The control software of the milling machine (Mini-Mill/3PRO from Minitech) was used to control the entire drilling process. Cutting speeds of 20 mm/min for the drilling process (downwards movements) and 50 mm/min for upwards and lateral movements were applied in order to fabricate an array of 10 electrodes within 20 s.

Arrays of Ø100 µm through holes with a center-to-center distance of 300 µm were fabricated at a feed rate of 0.8 µm/rev (Figure 72). No delamination around single holes was observed which demonstrates the stability of the assembly, even for drilling of electrode arrays.

Despite the mechanical support, foils were bending during drilling. Therefore, an initial drilling depth of 180 µm was not sufficient to drill through the entire assembly. Resistance-controlled microdrilling was applied to analyze the required drilling depth by monitoring the electrical resistance between the drill and the lower PEDOT layer (Figure 64). The lower PEDOT was reached at a drilling depth between 200 and 220 µm. Based on the tool geometry (angled face of the drilling tool, Chapter 3.1.1) additional 25 µm were applied to ensure a constant drilling shaft diameter.

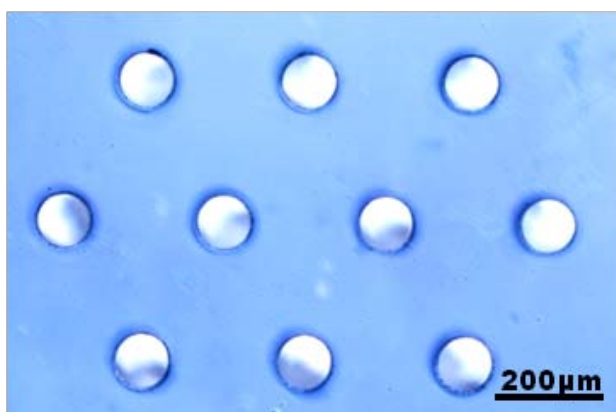


Figure 72: Micrograph of a fabricated array of ten Ø100 µm through holes using an automated drilling procedure. (drilling depth: 245 µm; feed rates: 0.8 µm/rev; cutting speed 20 mm/min; speed for lateral movements: 50 mm/min)

Electrode Characterization

To analyze the dimensions of the fabricated electrodes, the drilled holes were imaged with scanning electron microscopy (SEM). Images of the fabricated holes showed tubular electrodes as a dark ring at the upper end of the drilling shaft (Figure 73 A). A magnification of the area around the electrode shows distinctive areas inside the ring: a grey zone (a) around a deep black ring (b), surrounded by bright zones (c) (Figure 73 B).

Based on the fact that conductive material does less electrostatic charge during SEM imaging it can be assumed that the black ring (Figure 73 B, a) corresponds to the PEDOT layer. The grey zone around the black ring could indicate an accumulation of less conductive material, e.g. deformed PEDOT which smeared along the sidewalls during the drilling process (Figure 73 B, b). The bright area above and below the dark zone presents most likely pure non-conductive TOPAS which charged during imaging.

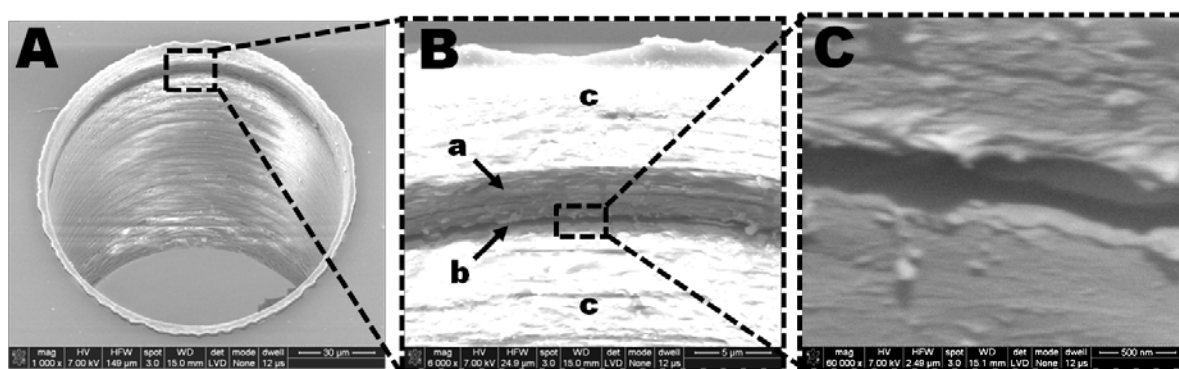


Figure 73: (A) SEM image of a drilling shaft with an integrated tubular PEDOT electrode. (B) Magnification of the area around the tubular electrode. (C) Magnification of the area around the PEDOT layer.

The deformation of the electrode material was also observed previously. Corti et al. described a deformation of a thin gold layer deposited on a cylindrical insulating material (Lucite) and covered with epoxy-resin, after drilling holes into it [Corti, 1994]. The gold layer smeared along the drilling shaft sidewall and therefore increased the effective electrode area. Konash et al. observed a smearing of a carbon paste along the surrounding material upon physical contact with a punching tool as well as after laser ablation [Konash, 2009].

The comparison to these observations shows considerable similarities. It was therefore assumed that the PEDOT becomes deformed during the drilling process. For sensor applications it is important to define the electro-active electrode area. Electrochemical deposition of silver dendrites from a 0.1 mM aqueous solution of AgNO_3 enabled a visualization of the electrode area (Figure 74 C). The electro-active area was calculated from the distance between the dendrite origins across the PEDOT ring. Measurements at different point of the ring were used to quantify the homogeneity of the electrodes.

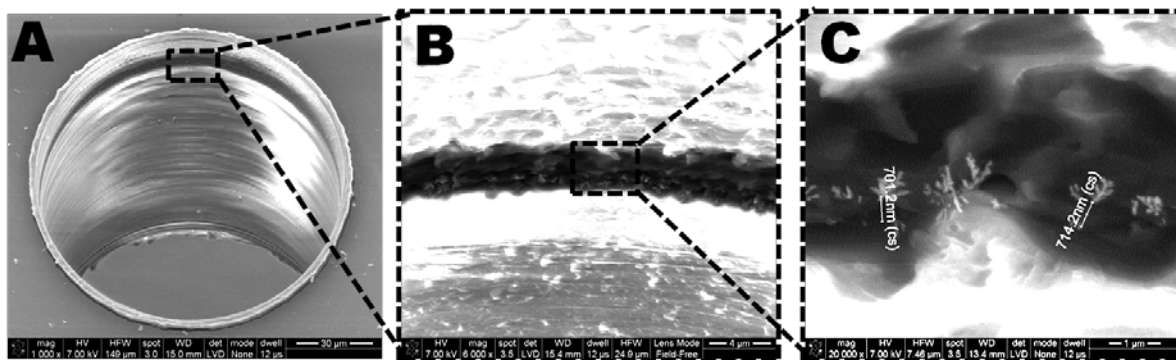


Figure 74: A) SEM image of a drilling shaft with an integrated tubular PEDOT electrode. B) Magnification of the area around the tubular electrode. C) Magnification of the electro-active PEDOT area which was made visible by deposition of silver dendrites from an aqueous solution. Note: “cs” indicates the tilt-compensation during the measurement.

Silver dendrites were only observed within a limited area of the black ring which was initially defined as highly conductive PEDOT material. Even if the mentioned grey zone around the black ring consists of deformed PEDOT, these areas were not electrochemical active. Thus they will not participate in electrode processes.

The analysis of the distance between the silver dendrite origins across the active PEDOT area, allows the determination of the electrode dimensions (Figure 74 C). An electrode thickness of 780 ± 84 nm was determined for the initial set of electrodes, fabricated with a feed rate of $0.8 \mu\text{m}/\text{rev}$. Considering an initially applied PEDOT layer of about 300 nm in thickness (Chapter 4.2), the determined electrode heights indicates significant PEDOT deformation during the drilling process.

5.2.6 Deformation of PEDOT during the Drilling Process

In order to minimize the observed PEDOT deformation during the fabrication, two process parameters were investigated:

- The influence of the drying state of the spin coated PS layer before application of the polymerization solution during the assembly preparation:

The integration of an intermediate PS-layer stabilized the assembly significantly (Chapter 5.2.4). For initially fabricated electrodes, the PS layer was spun for 300 s in order to evaporate the main part of solvents. Thus, the synthesis of the PEDOT layer proceeded on an almost dried PS film. A PEDOT synthesis on a non-dried PS film could cause an integration of flexible chains at the PS interface into the polymerizing PEDOT network. The resulting higher interaction between PEDOT and PS could result in a higher resistance towards the friction forces during the drilling process and therefore in less PEDOT deformation.

- The influence of the feed rate during the electrode fabrication:

Based on e.g. friction forces or increased heating, the probability of a PEDOT smearing along the sidewalls increases with the frequency of passing flutes. Therefore it could be possible to reduce the PEDOT smearing by increasing the feed rate (reduction in rotation).

However at too high feed rates (too low rotations) the chip size of the material becomes too large to be removed by the tool. The drill starts to act more as punching tool than as a drill. The increasing friction at the sidewall will most likely result an increased PEDOT deformation.

Determination of Polystyrene Drying Rate

To investigate the evaporation process of the solvent from the spin coated PS film, a Ø6 cm TOPAS foil was spin coated with 1 ml of a 5 mg/ml PS solution, dissolved in 1:1 (vol.) tetrahydrofuran/toluene at 1000 rpm for 60 s using an acceleration of 500 rpm/s. The foil was immediately afterwards transferred to a microbalance. In order to imitate the airflow above the foil during the spin coating, a stream of nitrogen was aligned horizontally about 2 cm above the PS covered foil. The change of the mass within the first 5 min was analyzed. To determine the mass of the foil after complete evaporation of the solvents from the PS film, the foil was placed for two minutes on a heated plate at 75°C and weighed. The mass change was determined again after another 60 minutes at room temperature. The mass changes are presented in Figure 75.

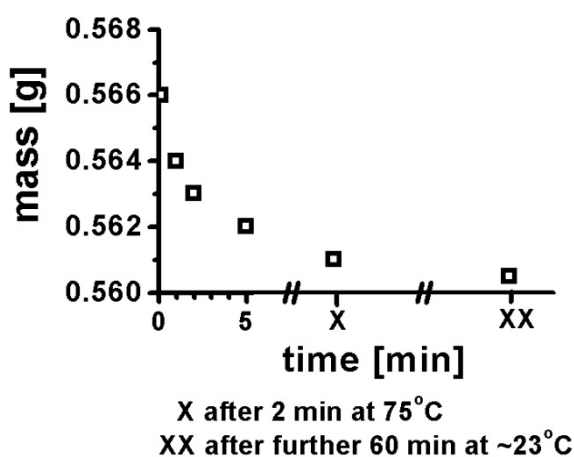


Figure 75: Determination of time dependent mass changes of a Ø6 cm TOPAS foil coated with a solution of dissolved polystyrene in 1:1 (vol.) tetrahydrofuran/toluene (spin time: 60 s, spin speed: 1000 rpm, acceleration: 500 rpm). Note: Breaks on the time axis indicate non-linear measurement regime.

A non-linear mass decrease of about 4 mg was observed within the first five minutes after the spin coating. A heating of the foil at 75°C for two minutes resulted in a decrease of an additional milligram. After 60 min at room temperature the mass of the foil was reduced by another 0.5 mg.

The decreasing mass of the foil documents the presence of remaining solvent after 60 s spinning. Therefore it can be assumed that the PS on the foil is not completely dried and that the PS chains at the interface are still flexible. Application of the polymerization solution directly after spin coating PS should cause the desired effect of a stronger interaction.

The small mass decrease of the foil after five minutes of about 1.5 mg supports the initial statement that the application of the polymerization solution was realized on an almost dried PS layer. This time was kept for the variation of the drilling feed rates since a transfer to a heating plate as well as spin duration of 60 min were unacceptable for the preparation of the final foil assembly.

Experimental Parameters-Feed rate variation

Electrodes were fabricated at different feed rates on assemblies prepared with 60 s as well as 300 s PS spin times. Feed rate variations were achieved by changing the spindle speed (rotation of the tool), in order to keep the fabrication time for a 10 electrode array at 20 s. Feed rates from 0.5 µm/rev to 10 µm/rev were investigated. 20 µm/rev was excluded since the high feed rates caused distorted holes. Silver dendrites were deposited at the tubular PEDOT electrodes to visualize the electro-active area. The samples were finally characterized by SEM with respect to differences in the PEDOT deformation. The height of each electrode was determined at least at three different points along the PEDOT ring. The mean and the standard deviation (error bars in Figure 76 A) were calculated from determined heights of electrodes fabricated with the same parameters.

Influence of PS Drying State and Drilling Feed Rates on Electrode Dimension

Drilling at different feed rates into assemblies prepared with PS spin times of 60 s and 300 s result in mainly two sets of electrode dimensions. Electrodes fabricated on assemblies prepared with a non-dried PS film (PS spin time: 60 s) were about $0.40 \pm 0.11 \mu\text{m}$ high while electrodes fabricated on assemblies prepared with an almost dry PS film (PS spin time: 300 s) were $0.97 \pm 0.22 \mu\text{m}$ high (Figure 76).

Different applied feed rates had no significant influence on the electrodes height. Electrodes fabricated on assemblies with the same PS spin time had almost the same heights. A comparison of the electrode heights fabricated at assemblies with PS spin times of 60 s and 300 s showed a significant difference. A shorter PS spin time (60 s) resulted in electrode heights of about the half compared to heights observed for a long PS spin time of 300 s. Therefore, the application of the polymerization solution on a non-dried PS film result in a reduced PEDOT deformation during electrode fabrication most likely based on a higher interaction between PEDOT and PS and.

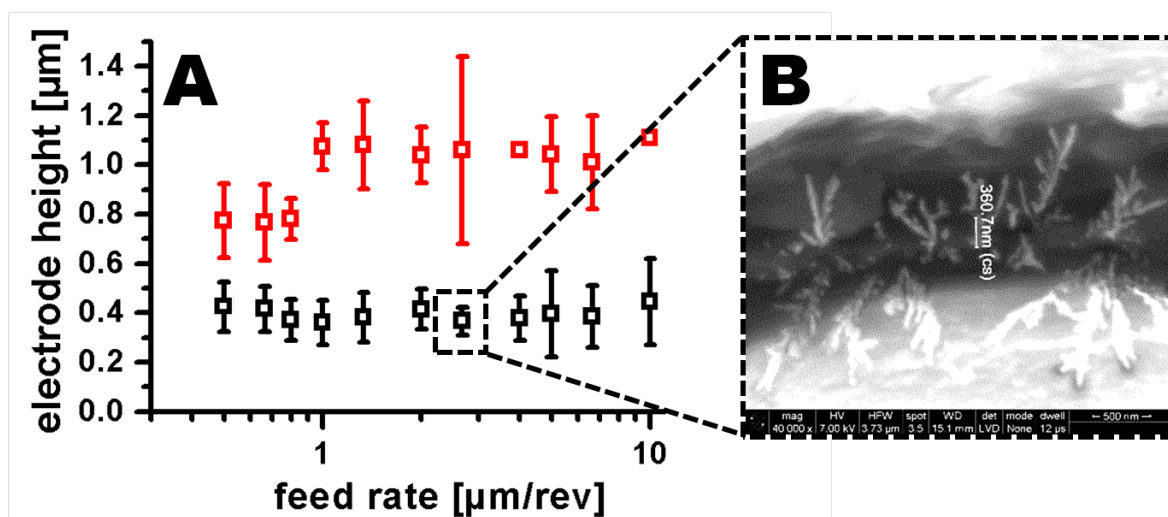


Figure 76: A) Measured electro-active PEDOT heights as function of applied feed rates for electrodes fabricated in assemblies produced with a non-dried (black symbols) and an almost dry (red symbols) polystyrene layer. The PEDOT heights were determined by measuring the distance between the origins of electrochemical deposited silver dendrites across the PEDOT layer. B) SEM image of a tubular PEDOT electrode fabricated at a feed rate of 2.7 $\mu\text{m}/\text{rev}$ after electrochemical deposition of silver dendrites.

5.2.7 Optimized Electrode Array Fabrication

For sensor applications, a high reproducibility of the electrode fabrication is important. Since the average electrode height was independent of the applied feed rate, the homogeneity of the electrodes was taken as indicator for optimal drilling parameters. The lowest deviation of $0.06 \mu\text{m}$ was observed for a feed rate of $2.7 \mu\text{m}/\text{rev}$ (Figure 76).

An array of ten $\text{Ø}100 \mu\text{m}$ electrodes was fabricated with a feed rate of $2.7 \mu\text{m}/\text{rev}$. After deposition of the silver dendrites, the 1st, 2nd, and 3rd as well as 6th and 9th electrode were analyzed with respect to reproducibility of fabrication process and homogeneity of the electrode height. Analyzed electrodes were measured at 5 different places (Figure 77).

Determined heights of the six analyzed electrodes were within the range of $0.37 \pm 0.06 \mu\text{m}$ (Figure 77) indicating a reproducible fabrication. The deviation is mainly caused by inhomogeneities within the single electrodes. A comparison of independent electrode arrays was demonstrated by recorded amperometric currents of potassium ferrocyanide (Chapter 5.2.9.1).

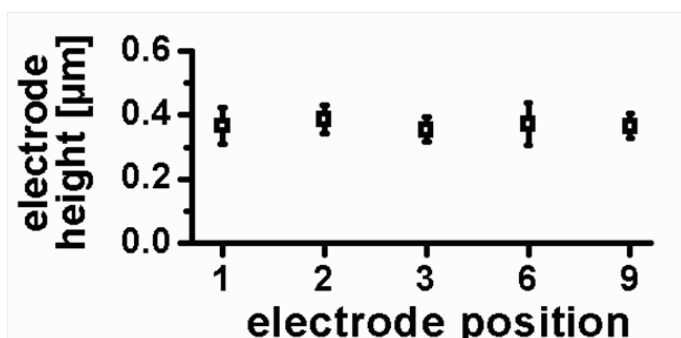


Figure 77: Obtained electrode heights for the 1st, 2nd, and 3rd as well as 6th and 9th electrode in a ten $\text{Ø}100 \mu\text{m}$ electrode array. Electrodes were fabricated at feed rate of $2.7 \mu\text{m}/\text{rev}$ on an assembly produced with a non-dried polystyrene layer.

Four electrodes of the array were analyzed regarding their diameter. The average diameter of these four electrodes was $101.4 \pm 1.6 \mu\text{m}$, measured on SEM images. A typical micrograph is presented in Figure 78 A.

The bright ring around the drilled holes is most likely polymer deformed during the drilling process. Profilometric analysis of these areas showed height differences of $3.3 \pm 1.6 \mu\text{m}$ which was not expected to significantly influence the performance of the electrochemical sensor (Figure 78 B).

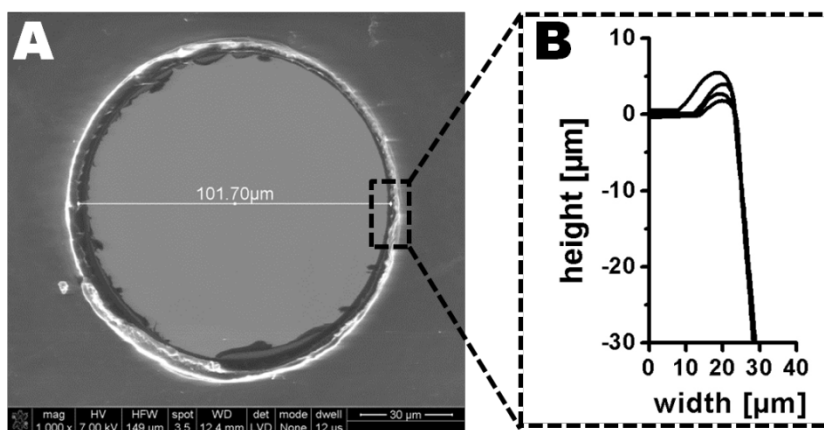


Figure 78: A) SEM image of a drilled through hole (top view). B) Profiles across the edge of drilled through holes (tool: Ø100 μm drill, feed rate: 2.7 μm/rev)

5.2.8 Bonding

Before drilling of the tubular electrodes, the assemblies were bonded to a multi-well system made of TOPAS 5013 (Figure 71) to increase mechanical stability of the foil. After drilling a second multi-well system was used to seal the system by applying a silicone based adhesive tape. The aligned and gently attached systems were bonded in a press by applying 2.5 bar for 600 s at 50°C (Figure 79).

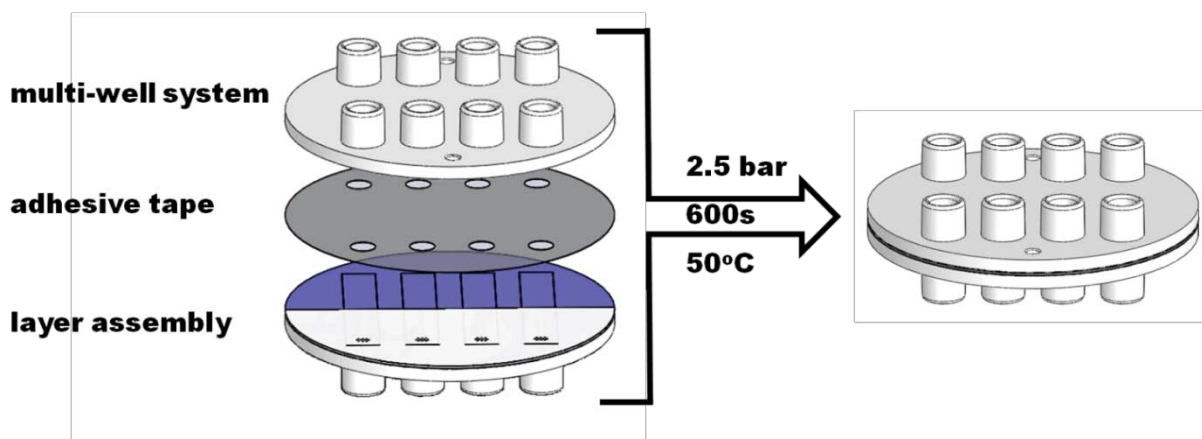


Figure 79: Assemblies with the electrodes arrays were bonded to a second multi-well system in order to seal the electrochemical system. The bonding was realized using silicone based adhesive tape and application of 2.5 bar for 600s at 50°C.

5.2.9 The Electrochemical Microfluidic System

The fabricated electrodes were used for amperometric detection of potassium ferrocyanide and hydrogen peroxide. The detection of potassium ferrocyanide was mainly done to demonstrate the reproducibility of the electrode fabrication. Hydrogen peroxide detection was demonstrated as a prerequisite for a future use of the tubular electrodes in a glucose sensor.

The drilled electrode arrays were connected with tubings to a syringe pump (inlet) and a disposable syringe tip (outlet). The syringe tip was used as waste container as well as to integrate a Ag|AgCl|3M NaCl reference electrode (Figure 80). The working electrodes (tubular electrode array with the layer assembly) and the counter electrode (planar PEDOT layer at the outlet) were electrically connected using spring loaded metal pins inside neighboring connection wells.

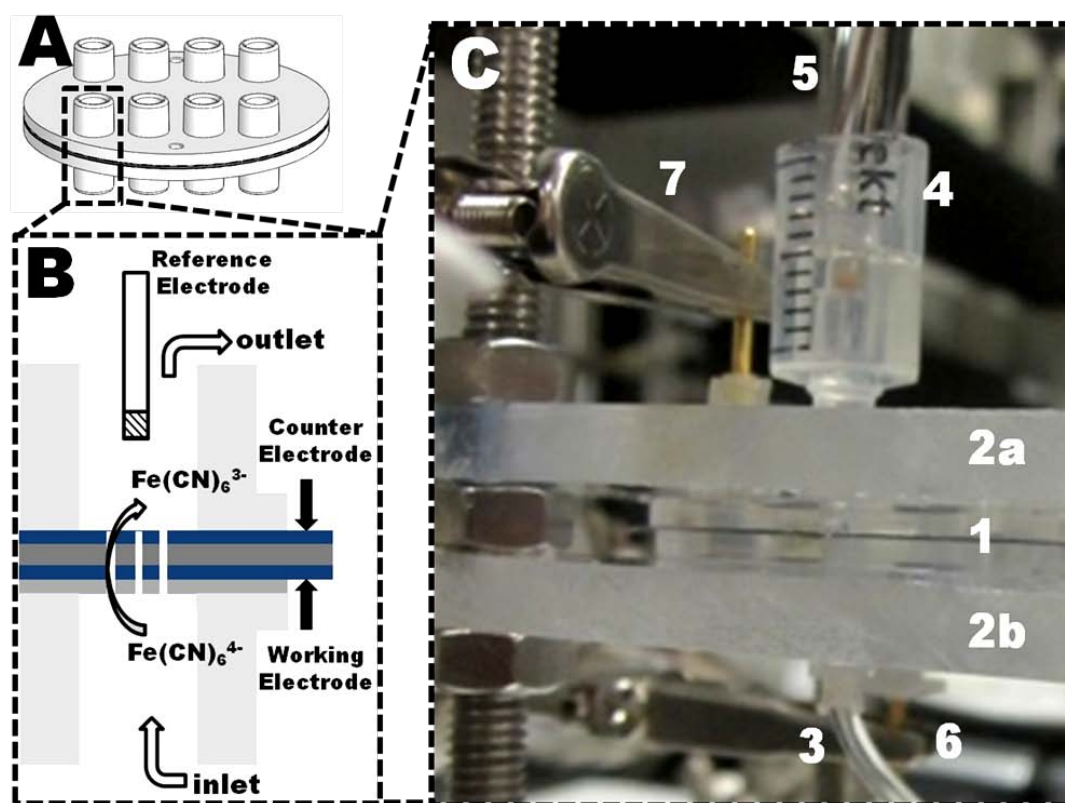


Figure 80: Detection principle and electrochemical setup: A) Assembly with electrode arrays bonded to two multi-well systems. B + C) For electrochemical analysis, the bonded system (1) was mounted into a holder (2a and 2b). A syringe pump was connected via tubings to a well at the bottom (3). A disposable syringe tip (4) at the outlet served as waste container and for integration of a Ag|AgCl reference electrode (5). The tubular working electrodes and the planar counter electrode were connected by spring loaded pins (6 and 7, respectively) through neighbored wells.

Experimental Parameters

Amperometric detection of potassium ferrocyanide was realized at 0.3 V vs. Ag|AgCl|3M NaCl in 0.1 M potassium phosphate buffer (pH 7.0) at a flowrate of 100 $\mu\text{l}/\text{min}$. After stabilization of a base current in phosphate buffer, a potassium ferrocyanide solution was continuously injected for 300 s (analyzed concentration range: 1 mM to 300 mM), followed by a continuous injection of phosphate buffer. Amperometry on prussian blue modified PEDOT films was carried out as described above, except an applied electrode polarization of 0 V vs. Ag|AgCl|3M NaCl and the application of hydrogen peroxide as analyte (concentration range: 0.1 mM to 5 mM).

5.2.9.1 Amperometric Detection of Potassium Ferrocyanide

The flow rate is an important parameter in amperometric experiments. The current needs to be recorded at different flow rates in order to avoid diffusion limited measurements. A diffusion limitation results in lower signal amplitudes and therefore in a sub-optimum sensor characteristic.

Flow Rate Variation

The influence of the flow rate on the amperometric response was analyzed by recording the oxidation current for 5 mM potassium ferrocyanide at 300 mV vs. Ag|AgCl|3M NaCl. Flow rates from 10 $\mu\text{l}/\text{min}$ up to 110 $\mu\text{l}/\text{min}$ were analyzed. Starting from 10 $\mu\text{l}/\text{min}$ the flow rate was increased and kept for 100 s before returning to the initial flow rate of 10 $\mu\text{l}/\text{min}$. Flow rates below 10 $\mu\text{l}/\text{min}$ could not be analyzed due to increased fluctuations from the pump.

An increase of the flow rate up to 100 $\mu\text{l}/\text{min}$ result in a non-linear increase in the current response from 450 nA to 557 nA. A further increase in flow rate did not change the current significant (Figure 81). A variation of the flow rate in absence of potassium ferrocyanide (phosphate buffer only) did not affect the base current.

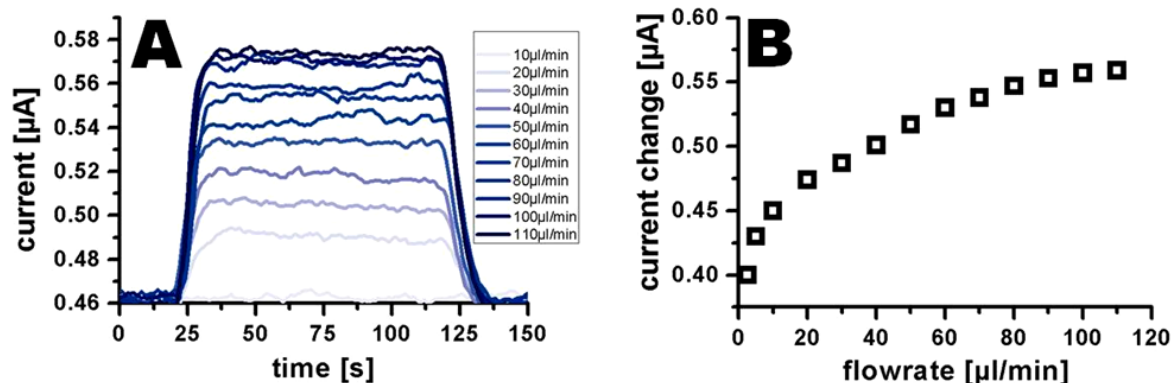


Figure 81: A) Amperometric signals of a ten $\text{\O}100\ \mu\text{m}$ tubular PEDOT electrode array, polarized at 300 mV vs. Ag|AgCl|3M NaCl in a 5 mM potassium ferrocyanide containing buffer solution at flowrates from 10 $\mu\text{l}/\text{min}$ to 110 $\mu\text{l}/\text{min}$. B) Determined current changes in dependency of the flowrate.

Amperometric Detection of Potassium Ferrocyanide

The amperometric detection of potassium ferrocyanide was realized at a working electrode potential of 300 mV vs. Ag|AgCl|3M NaCl using a flowrate of 100 $\mu\text{l}/\text{min}$. Concentrations from 1 to 30 mM caused a linear increase in the current response with a slope of 85 nA/mM (Figure 82 A and 83 B). A further increase in concentration up to 300 mM showed a non-linear response of the current, most likely based on saturation effects (Figure 82 B). The current responses of four independent systems (separate symbols in Figure 82 B) showed little variance, which demonstrates the high reproducibility of the fabrication process.

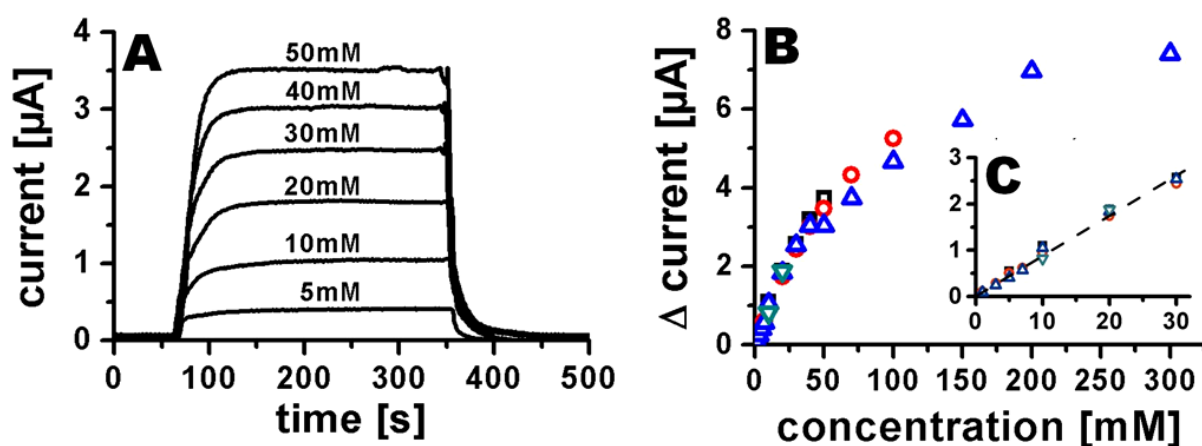


Figure 82: A) Amperometric response of a ten $\text{\O}100\ \mu\text{m}$ tubular PEDOT electrode array towards different potassium ferrocyanide concentrations in 0.1 M potassium phosphate buffer, at a flowrate of 100 $\mu\text{l}/\text{min}$ and an electrode polarization of 300 mV vs. Ag|AgCl|3M NaCl. B) Absolute current changes versus potassium ferrocyanide concentration, C) Magnification of the linear response regime in the range from 1 to 30 mM potassium ferrocyanide. Different symbols represent measurements with independent systems.

5.2.9.2 Amperometric Detection of Hydrogen Peroxide

For the detection of hydrogen peroxide, the PEDOT layer used as working electrode was modified with prussian blue. This was realized by adding prussian blue to the polymerization solution before synthesizing the PEDOT layers (Chapter 4.3). The fabrication of the tubular electrodes was realized as described previously.

The prussian blue modified PEDOT working electrode was polarized at 0 V vs. Ag|AgCl|3M NaCl in order to record the reduction current for hydrogen peroxide (Chapter 4.3). Injections of different concentrations from 0.1 to 5 mM resulted in an increasing sensor signal from 1 nA to 24 nA (Figure 83 A and 84 B). Higher concentrations caused signal instability, already visible at 5 mM. The linear range of the sensor was calculated for a concentration range from 0.1 to 1 mM with a sensitivity of 8.6 nA/mM.

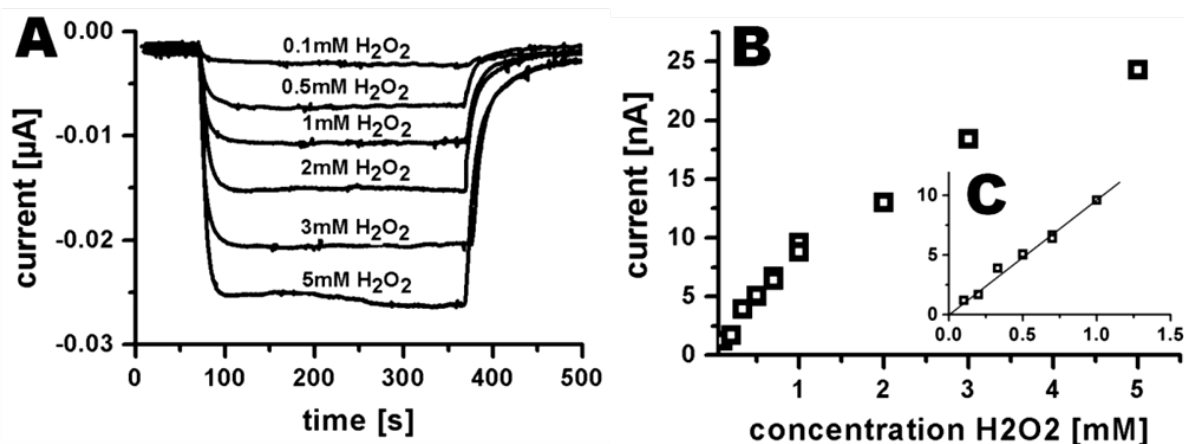


Figure 83: A) Amperometric response of an array of 10 electrodes, each being a $\text{\O}100\ \mu\text{m}$ tubular PEDOT/prussian blue electrode, towards different hydrogen peroxide concentrations diluted in 0.1 M potassium phosphate buffer at a flowrate of $100\ \mu\text{ml}/\text{min}$ and an electrode polarization of 0 mV vs. Ag|AgCl|3M NaCl B) Absolute current changes versus hydrogen peroxide concentration C) Magnification of the linear response regime in the range from 0.1 mM to 1 mM hydrogen peroxide.

5.2.10 Summary

A one-step fabrication strategy is presented for developing a microfluidic system with two integrated polymeric electrodes by using microdrilling. Microfluidic systems were fabricated by drilling through a TOPAS 5013 foil ($\text{\O}6$ cm, thickness $150\ \mu\text{m}$) spin coated on both sides with a layer of polystyrene (PS) followed by PEDOT. An additional PS layer electrically insulated the upper PEDOT layer. Drilling through the entire assembly resulted in a cylindrical drilling shaft, finally used as microfluidic channel, and two electrodes: a tubular PEDOT electrode integrated in the shaft sidewall and a large planar electrode placed at the end of the shaft.

A PS layer was introduced to increase the adhesion between the PEDOT layer and the TOPAS foil. Otherwise PEDOT delaminated during the drilling process from the TOPAS foil. The resulting electrodes had a diameter of $101.5 \pm 1.5\ \mu\text{m}$ defined mainly by the application of a $\text{\O}100\ \mu\text{m}$ drilling tool. The height of the electro-active PEDOT layer exposed during the drilling step was measured as maximum distance between electrochemical deposited silver dendrites at the electrode surface. The optimization of the fabrication process allowed drilling of homogenous tubular electrode arrays with an average PEDOT height of $370\ \text{nm} \pm 60\ \text{nm}$.

The electrochemical functionality of fabricated electrode arrays (10 electrodes, center-to-center spacing: $300\ \mu\text{m}$) was shown by recording the amperometric response to potassium ferrocyanide within a concentration range from 1 to 300 mM. Furthermore, the detection of hydrogen peroxide in a concentration range from 0.1 to 5 mM was successfully demonstrated after modification of the PEDOT electrodes with prussian blue. The hydrogen peroxide detection is an important step towards a possible glucose sensor.

5.2.11 References:

- [Andresen, 2010] Andresen, K. Ø.; Hansen, M.; Matschuk, M.; Jepsen, S. T.; Sørensen, H. S.; Utko, P.; Selmeczi, D.; Hansen, T. S.; Larsen, N. B.; Rozlosnik, N.; Taboryski, R. *Journal of Micromechanics and Microengineering* **2010**, *20*, 055010
- [Corti, 1995] Corti, H.; Ortiz, M.; Magallanes, J. *Electroanalysis* **1995**, *7*, 569-573
- [Engblom, 1996] Engblom, S. O.; Cope, D. K.; Tallman, D. E. *Journal of Electroanalytical Chemistry* **1996**, *406*, 23-31
- [Hansen, 2006] Hansen, T. S.; West, K.; Hassager, O.; Larsen, N. B. *Synthetic Metals* **2006**, *156*, 1203-1207
- [Heinze, 1993] Heinze, J. *Angewandte Chemie International Edition in English* **1993**, *32*, 1268-1288
- [Konash, 2009] Konash, A.; Harris, A. R.; Zhang, J.; Elton, D.; Hyland, M.; Kennedy, G.; Bond, A. M. *Journal of Solid State Electrochemistry* **2009**, *13*, 551-563
- [Kovach, 1985] Kovach, P.; Caudill, W.; Peters, D.; Wightman, R. *Journal of Electroanalytical Chemistry* **1985**, *185*, 285-295
- [Kyocera] Kyocera International, Inc; <http://www.kyoceramicrotools.com/>
- [Stulik, 2000] Stulik, K.; Amatore, C.; Holub, K.; Marecek, V.; Kutner, W. *Pure and Applied Chemistry* **2000**, *72*, 1483-1492

5.3 Fabrication of an Electrochemical System by a One Step Hot Embossing Procedure

5.3.1 Introduction

The fabrication of polymer microfluidic systems by hot embossing is already well established [Lee, 2001; Qi, 2002; Becker und Gärtner, 2008, Peng, 2009; Illa, 2010; Goral, 2011; Jena, 2011; Wang, 2011; Liedert, 2012]. The key advantage is a low cost replication of several hundred to thousand parts after fabrication of a stamp [Heckele and Schomburg, 2004; Becker und Gärtner, 2008]. The replication can be done in single embossing steps as well as by the application of roll to roll embossing [Yeo, 2009; Ng and Wang, 2009; Yeo, 2010, Liedert, 2012].

Structuring of metal as well as polymer electrodes was demonstrated with several methods. The most common methods for metal electrodes are cleanroom processes, including metal deposition, photo lithography and etching or lift off processes [Ceriotti, 2007; Cheng, 2010; Ges, 2010; Illa, 2010; Frey, 2011; Chen and White, 2011].

Conducting polymer electrodes can be fabricated by using cleanroom facilities as shown by Kiilerich-Pedersen et al. [Kiilerich-Pedersen, 2011]. However, polymer electrodes can also be defined by inkjet printing [Kawase, 2003, Chen, 2003; Mire, 2011; Tobjök and Österbacks, 2011], laser ablation [Schrödner, 2005] or wet chemistry [Hansen, 2007].

The fabrication of electrodes as well as the simultaneous fabrication of electrodes and the microfluidic system by a single hot embossing step has not been reported previously. A fabrication of electrodes and microfluidic channels in one step would reduce the processing time and avoid alignment problems during the assembly of chip components. Bonding of the final microfluidic system would only require an unstructured lid.

This chapter describes the fabrication of an electrochemical microfluidic system based on a one step hot embossing procedure. Optimized hot embossing parameters, presented in Chapter 3.2.2, were used for embossing a microfluidic channel into a PEDOT covered TOPAS bulk material. A working (WE) and a counter (CE) electrode were integrated into the channel by embossing slopes on opposite channel

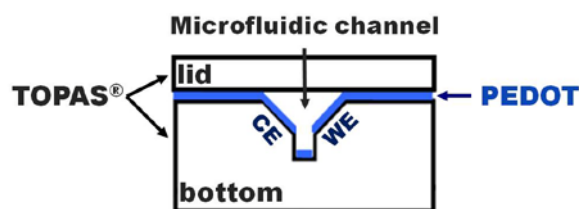


Figure 84: Cross section of the electrochemical, microfluidic system. The system consists of two parts: a lid as cover and a lower part which contains the embossed microfluidics with integrated working and counter electrodes at the surface. Electrodes are made out of PEDOT and exposed at the sloped channel sidewalls.

sidewalls. PEDOT on the sloped surfaces became integrated into the channel while retaining electrical connection to the PEDOT layer at the wafer surface. Thus, the PEDOT layer at sloped surface could be used as working electrode (WE) and counter electrode (CE). In order to disconnect WE and CE, slopes did not continue down to the channel bottom. A vertical step was applied between channel bottom and sloped PEDOT layer (Figure 84). An appropriate stamp design allowed the fabrication of a microfluidic system as well as the definition of the electrodes with only one hot embossing step (Figure 85).



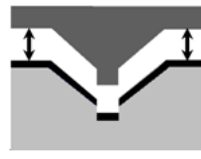

Nr.	Process step	Illustration
1	Cleaned non-conductive TOPAS [®] substrate (light gray)	
2	Spin on of a thin, conductive PEDOT layer (black)	
3	One step hot embossing procedure to define the microfluidic channel and the electrodes using a Al-stamp (dark grey)	
4	Sealing the system by thermal bonding of a TOPAS [®] lid	

Figure 85: Fabrication steps of the electrochemical system.

In order to optimize the stamp design two parameters were investigated: Firstly, the required step height for the disconnection of the sloped PEDOT from the PEDOT at the channel bottom (Chapter 5.3.2) was determined. Secondly, the maximum slope angle of the electrodes was analyzed (Chapter 5.3.3).

The final fabricated system was characterized by profilometry and scanning electron microscopy (SEM) (Chapter 5.3.4). Electrochemical functionality was demonstrated by amperometric detection of physiologically relevant glucose concentrations (0-10 mM) (Chapter 5.3.6).

5.3.2 Embossing of Isolated PEDOT Areas

A cross-section of the final chip design is presented in Figure 86 A. As highlighted by the red circle, the sloped electrodes did not proceed down to the channel bottom. The vertical step between the slopes and the channel bottom was used to isolate and therefore define the electrode areas. It was expected that due to certain stretchability, the PEDOT will be stretched across the vertical step for small step heights. The minimum step height was analyzed to ensure a complete PEDOT disconnection. Even minor electrical connections between a sloped electrode and the PEDOT at the channel bottom would lead to undefined electrode areas. This would cause inhomogeneous or unrepeatably electrochemical results. An electrical connection between both electrodes via the channel bottom would result in electrical short circuits during the measurement.

To determine the minimum step size for a complete disconnection channel structures with vertical sidewalls were embossed into PEDOT covered TOPAS bulk material (Figure 86 B).

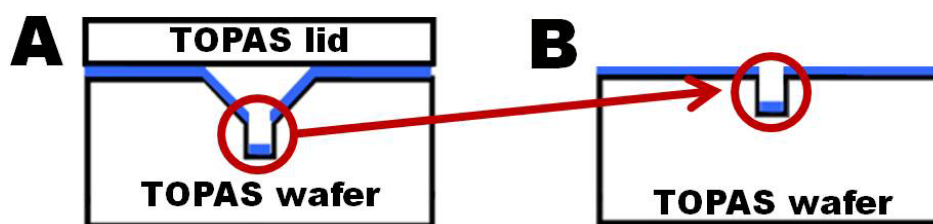


Figure 86: A) Sketch of the cross-section of the electrochemical microfluidic device. PEDOT electrodes are placed at the sloped channel sidewalls (blue). The red circle highlights a vertical step that isolates the sloped electrodes from the channel bottom as well as from each other. B) Test design to investigate critical vertical step height to disconnect PEDOT areas.

The disconnection between the embossed channel bottom and the PEDOT layer at the TOPAS surface was monitored by measuring the electrical resistance across the channel sidewall. To create a defined measurement area, the PEDOT layer at the TOPAS surface was partly deactivated by incubation with aqueous sodium hypochlorite using agarose stamping (Figure 87). The resistance analysis was realized between the conductive PEDOT at the channel bottom and two lines of remaining conductive PEDOT at the TOPAS surface (perpendicular to the channel direction).

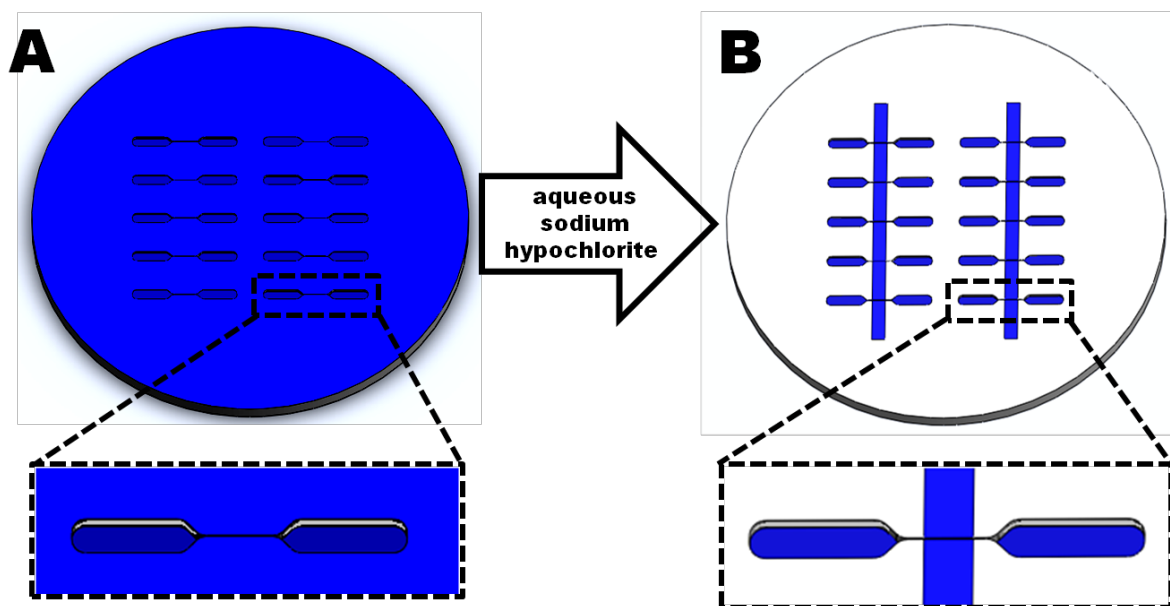


Figure 87: A) Model of a PEDOT covered TOPAS wafer after embossing of 10 microfluidic channels. B) Wafer after deactivation of the PEDOT at the wafer surface using aqueous sodium hypochlorite. Magnifications show a single microfluidic channel A) before and B) after the deactivation. All blue areas indicate conductive PEDOT, all white areas inactivated PEDOT.

Experimental Parameters

Channel structures, 50 μm to 400 μm in width and 10 μm to 50 μm in height were embossed into a PEDOT covered TOPAS 5013 (T_g about 135°C) bulk material at molding temperatures of 135°C, 143°C, and 150°C. Embossing pressure and time varied with the process temperature. Moldings at 135°C were performed with 6 bar for 240 s, at 143°C with 3 bar for 240 s, and at 150°C with 1.5 bar for 180 s. The embossing was realized on PEDOT layers with a height of 130 nm, 280 nm, and 430 nm. A detailed description of the PEDOT spin coating process can be found in Chapter 4.2, the stamp fabrication in Chapter 3.1.4, and the embossing process in Chapter 3.2.2.

Deactivation of the PEDOT layer at the TOPAS surface was realized after embossing the channel structures using an aqueous sodium hypochlorite loaded agarose stamp [Hansen, 2007]. The mold for the agarose stamp was fabricated by micromilling two free standing (inverse) channel structures out of a $\text{Ø}50$ mm TOPAS 5013 disc (Figure 88 A). Agarose stamps were casted from the mold (Figure 88 B) and loaded with aqueous sodium hypochlorite (10%). The stamp surface was briefly dried in nitrogen stream before being pressed gently onto the structured PEDOT/TOPAS wafer (Figure 88 C). Deactivation of the PEDOT at the surface was performed within 5 min. PEDOT areas without agarose contact (lines across the wafer and embossed channel structures) remained conductive.



Figure 88: Process of PEDOT deactivation by incubation with aqueous sodium hypochlorite using agarose stamping. A) After a mold fabrication, B) the mold surface was replicated in an agarose gel. C) The gel was loaded with aqueous sodium hypochlorite and pressed for 5 min against the structured PEDOT/TOPAS wafer. Deactivation took place only at contact areas, PEDOT at embossed areas as well as at the two lines of the mold structure remained conductive.

The stretching of the PEDOT across each vertical channel sidewall was analyzed by measuring the electrical resistance between the channel bottom and the upper surface level (Figure 89). Therefore, one spring loaded contact pin of a two point probe was connected to the PEDOT layer at the channel bottom, the second spring loaded pin was connected to the corresponding conductive PEDOT line at the upper surface level (Figure 89 B, Ω_1).

In cases of insufficient drying or too high pressure applied on the agarose gel, it rarely happened that the sodium hypochlorite solution penetrated the embossed structures and inactivated the PEDOT at the channel bottom. Inactive PEDOT at the channel bottom would distort a resistance analysis across the embossed step. The functionality of the PEDOT at the channel bottom was verified by a separate resistance measurement between the two embossed connection areas (Figure 89 B, Ω_2).

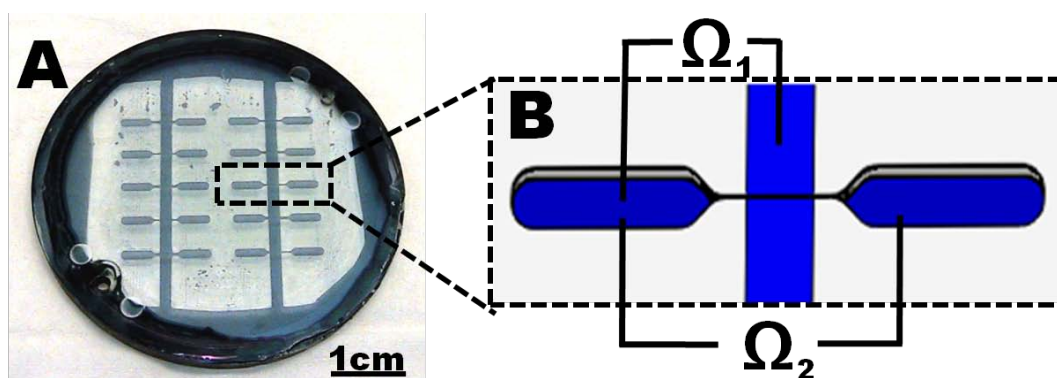


Figure 89: A) A structured PEDOT covered TOPAS wafer after PEDOT deactivation with aqueous sodium hypochlorite used for analysis of the minimum PEDOT disconnection height. B) A sketch of a separated embossed area with PEDOT at the channel bottom (dark blue) and a line of remaining conductive PEDOT after deactivation at the upper surface level (bright blue). The PEDOT stretching across the channel sidewall was analyzed by electrical resistance measurement between the PEDOT at embossed area and the remaining PEDOT at the surface (Ω_1). To ensure conductivity of the PEDOT at the embossed area, the electrical resistance between the two connection areas was measured (Ω_2).

Investigation of the Disconnection Height

Electrical disconnection of the PEDOT was usually achieved at an embossing height between 30 μm and 40 μm independent of channel width, PEDOT layer height, and molding temperature. In few cases disconnection took place at a larger embossing depth of 50 μm . A reason why the disconnection took rarely place at larger embossing depth could not be found since a variety of parameters like edge sharpness of the aluminum stamp structure, stamp-substrate-alignment during the embossing process, and manual release of molded parts and stamp, manual PEDOT deactivation influenced the final electrical resistance measurement. To ascertain PEDOT disconnection in the final device, a minimum embossing height of 50 μm was set for all channel dimensions and molding temperatures.

5.3.3 Embossing of Sloped PEDOT Areas

Embossing of sloped channel sidewalls enabled the integration of electrodes into the microfluidic channel. Deformation of the PEDOT layer along sloped surfaces created electrodes. Embossing of slopes into opposite channel sidewalls led to a spatial separation of two electrodes (working and counter electrode) forming an entire electrochemical microfluidic system.

In order to achieve electrode surfaces without imperfections or cracks, the maximum deformation angle for the PEDOT layer was analyzed. Therefore, a stamp with slopes ranging from 15° to 60° to the surface plane was fabricated by micromilling (Chapter 3.1.4) and embossed into a PEDOT covered TOPAS 5013 bulk material. The slopes were visualized by SEM in a 25° tilted perspective. A sketch of the embossed structure is presented in Figure 90. The imaged part is highlighted by the black, dotted rectangular together with a SEM image of a slope.

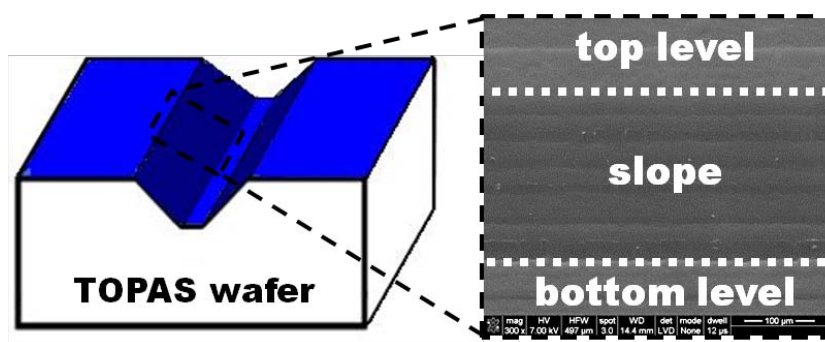


Figure 90: Left: Sketch of embossed PEDOT covered TOPAS wafer. The area which is surrounded by the black, dotted square represents the recorded area of the following SEM pictures. Right: Example of a recorded SEM picture of a 15° sloped surface. The sloped area is within the dotted, white lines. The area above the upper dotted line represents the wafer surface level, the area below the lower dotted line the lowest embossed area.

Deformation of 130 nm thick PEDOT Layer

A SEM analysis of embossed slopes in 130 nm thick PEDOT layer showed the ability of a deformation up to 15° with only a small amount of imperfections. With an increased slope angle of 30° the amount of imperfections increased. Eventually small cracks within the PEDOT layer were observed. An angle of 45° caused large cracks across the sloped area and therefore a total disconnection of the PEDOT layer (Figure 91).

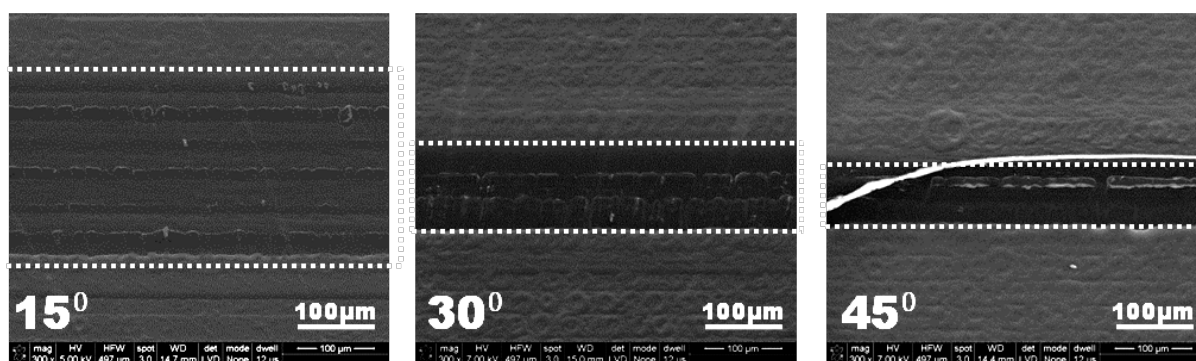


Figure 91: SEM images of sloped PEDOT areas after hot embossing (view: 25° tilted). Slopes of 15° (left), 30° (middle), and 45° (right) to the surface plane are defined within the dotted lines. The deformation was realized by embossing the stamp into a 130 nm thick PEDOT layer on a TOPAS 5013 substrate. (embossing realized at 150°C with 1.5 bar for 180 s)

Increase of the Deformation Angle by Integration of PEDOT into TOPAS

Hansen et al. increased the stretchability of PEDOT by integration into polyurethane while retaining conductivity [Hansen, 2007]. The effect of integrated PEDOT into the TOPAS substrate was analyzed regarding changing deformability behavior. PEDOT was integrated into the TOPAS substrate by washing the synthesized PEDOT layer using a tetrahydrofuran and toluene mixture [Hansen, 2006]:

After spin coating an approximately 130 nm thick PEDOT on a Ø50 mm TOPAS 5013 wafer, the PEDOT film was baked to increase the polymerization rate and to evaporate remaining solvent. Instead of using deionized water, the PEDOT film was washed with 3 ml of a mixture of tetrahydrofuran and toluene (1:1, vol %). The solvent mixture was continuously applied on the rotating sample (spin coater) within the first 10 s of a 30 s long spinning step at 1000 rpm. The sample was finally dried out on a hot plate for 5 min at 65°C, before being used for embossing of the slopes.

Dark field images of the sloped areas showed that integrated PEDOT layers already crack at slope angles of 15° to the surface plane (Figure 92). The stretchability of PEDOT could not be increased by an integration of PEDOT into the TOPAS bulk material. Furthermore, the PEDOT displayed a total loss of conductivity after embossing.

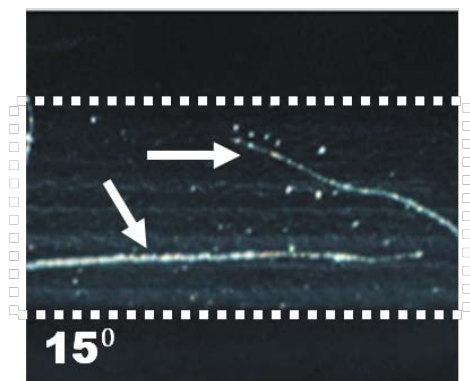


Figure 92: Dark field images of a 15° sloped PEDOT area after hot embossing (top view). The sloped areas are within the white dotted lines. A 130 nm thick PEDOT layer was integrated into TOPAS by washing with tetrahydrofuran and toluene. Arrows highlight cracks within the PEDOT layer at the sloped surface. (embossing was realized at 150°C with 1.5 bar for 180 s)

Increase of the Deformation Angle through Different Moulding Temperatures

The application of different molding temperatures could influence the deformation behavior of the 130 nm thick PEDOT layer due to changes in flow behavior of the underlying bulk TOPAS material. Embossing temperatures of 135°C , 143°C , and 150°C were investigated.

Figure 93 presents sloped 30° surfaces, embossed at 135°C (Figure 93 A), 143°C (Figure 93 B), and 150°C (Figure 93 C). Similar patterns of imperfections at the sloped PEDOT areas (in between the dotted white lines) were found for all three molding temperatures. For a molding temperature of 135°C , small cracks were observed at the bottom of the sloped areas which indicates a decreased stretchability of the PEDOT at lower embossing temperatures. Thus, a variation of the molding temperature did not improve the surface quality of the deformed PEDOT area.

The fact that for all molding temperature similar imperfection patterns were observed could also lead to the conclusion that the imperfections are caused by the surface of the stamp. If the imperfections would be caused by the PEDOT film a more irregular pattern would have been expected.

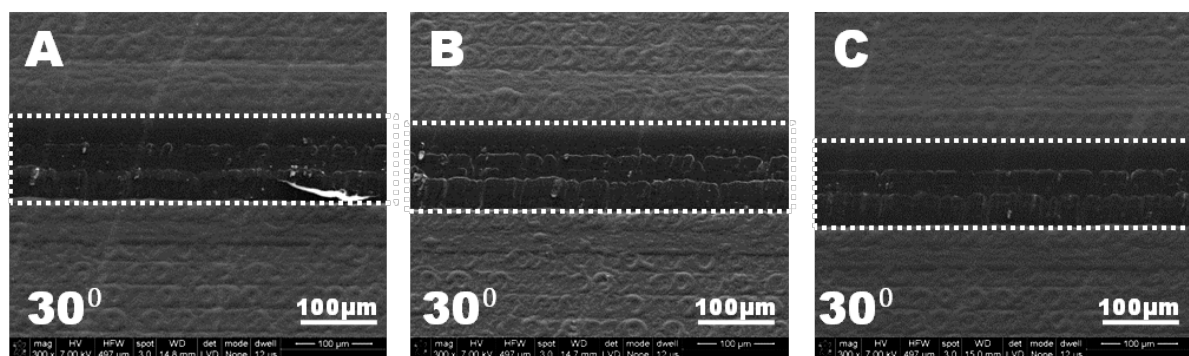


Figure 93: SEM images of sloped PEDOT areas after hot embossing (view: 25° tilted). All images present slopes of 30° to the surface plane which are between the white dotted lines. Embossing was realized at temperature of A) 135°C, B) 143°C, and C) 150°C.

Increase of the Deformation Angle by an Increased PEDOT Layer Thickness

Besides embossing temperature and PEDOT integration into TOPAS, the PEDOT layer thickness might influence the deformability. A thicker PEDOT layer might be more resistant to stamp imperfections due to a decreasing ratio of the imperfection height at the stamp and PEDOT layer thickness. Stamp inhomogeneities might not be able to penetrate the entire PEDOT layer causing a fully PEDOT covered slope. PEDOT films of 280 nm and 430 nm in thickness embossed at 150°C were investigated.

SEM images of slopes defined in a 280 nm thick PEDOT layer are presented in Figure 94. The increase of the PEDOT thickness reduced imperfections significantly for slope angles of 30°. Homogeneous PEDOT layer were obtained at 30° sloped surfaces. No cracks, only imperfections were observed at 45° slopes. The pattern of imperfections at 45° slopes was similar to patterns observed before at the 30° sloped areas.

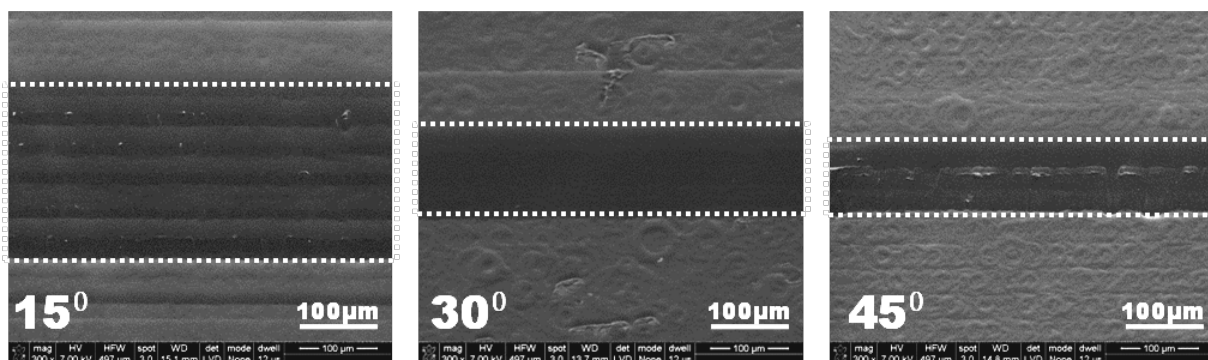


Figure 94: SEM images of sloped PEDOT areas after hot embossing (view: 25° tilted). Slopes of 15° (left), 30° (middle), and 45° (right) to the surface plane are shown between the white dotted lines. The deformation was realized by embossing a stamp into a 280 nm thick PEDOT layer on a TOPAS 5013 substrate. (embossing was realized at 150°C with 1.5 bar for 180 s)

To investigate if a further improvement of the maximum slope angle can be achieved by a further increase in PEDOT thickness, a 430 nm thick layer was deformed (molding temperature: 150°C).

SEM images presented in Figure 95 show an almost identical appearance as observed for a 280 nm thick PEDOT layer. Thus, a further increase of the PEDOT layer thickness does not seem to allow higher deformation angles. However, it was not investigated if a further increase in layer thickness would enable higher deformation angles.

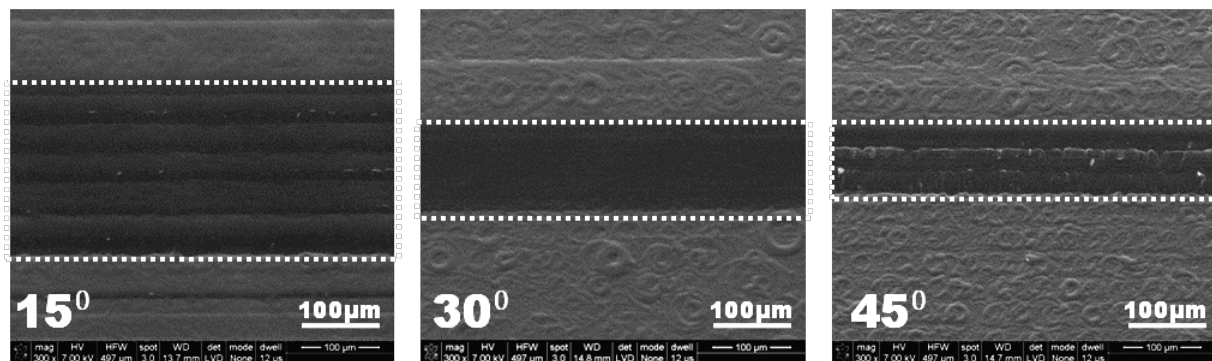


Figure 95: SEM images of sloped PEDOT areas after hot embossing (view: 25° tilted). Slopes of 15° (left), 30° (middle), and 45° (right) to the surface plane are shown between the white dotted lines. The deformation was realized by embossing a stamp into a 430 nm thick PEDOT layer, previously spin coated on a TOPAS 5013 substrate. (embossing realized at 150°C with 1.5 bar for 180 s)

5.3.4 Design of the Electrochemical Microfluidic System

From results described in Chapter 5.3.2 and Chapter 5.3.3 the dimensions of the final electrochemical microfluidic system were defined. As discussed, the working and counter electrode can be integrated into the microfluidic channel by embossing slopes into the opposite channel sidewalls. Both electrodes are spatially separated by a microfluidic channel in between and isolated from the PEDOT at the channel bottom by embossing a vertical step between slope and channel bottom. A minimum step height of 50 μm is required to ensure a disconnection between the PEDOT electrodes and the PEDOT at the bottom of the microfluidic channel (Chapter 5.3.2). For a 280 nm thick PEDOT layer the slope angle of the electrodes can not exceed 30° to the surface plane (Chapter 5.3.3).

A sketch of the electrochemical microfluidic system with fixed dimensions is presented in Figure 96. The length of the working electrode (parallel to the channel direction) was defined as 0.5 mm, the height as 0.1 mm. Due to the slope angle of 30° , the electrode area is 0.1 mm^2 . The counter electrode was designed with the same height and angle but 4 mm long.

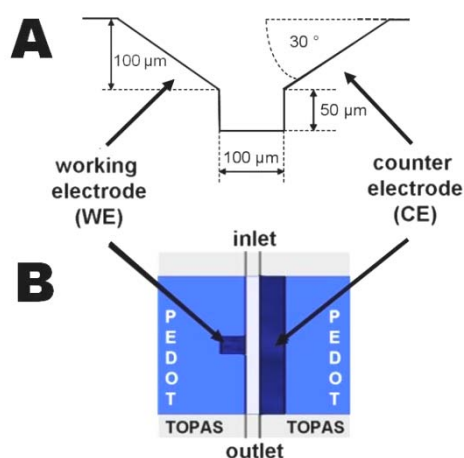


Figure 96: Design of the microfluidic system with integrated working and counter electrode. Electrodes are defined as slopes at the channel sidewalls and electrically disconnected by a steep channel in between. A) Sketch of the cross-section with corresponding dimensions, B) Model of the system as top view.

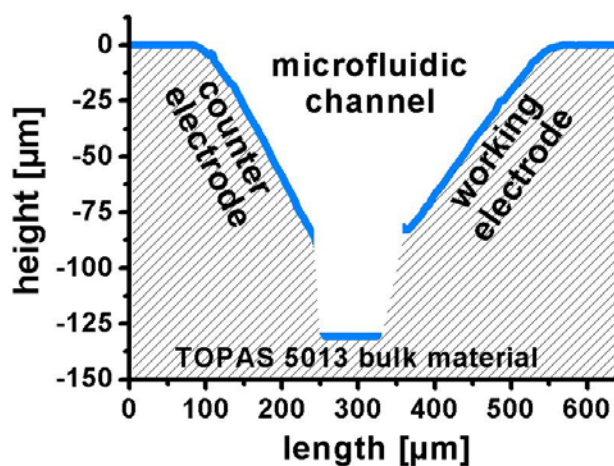


Figure 97: Manually modified profile of the cross-section of an embossed electrochemical system. The different parts of the system were enhanced to visualize the TOPAS bulk material (line pattern) and the PEDOT covered areas of the surface (blue lines). (Note: vertical axis is expanded by factor of 3)

The embossed electrochemical system was characterized using profilometry as well as SEM. A profile of the cross-section is presented in Figure 97 (scan direction from left to right). The area under the scanned profile was patterned to visualize the TOPAS bulk material. Blue lines in the profile symbolize PEDOT covered areas. An evaluation of the embossed slope angle resulted in 31° for the counter electrode and 27° for the working electrode. The smaller deformation angle of the working electrode is most likely an artifact of the profilometer measurement.

SEM images were recorded to visualize the PEDOT electrode surfaces. Figure 98 A presents a 45° tilted view of the embossed electrochemical system with focus on the working electrode. Figure 98 B presents a magnification of the right side of the working area. Both pictures show a homogenous deformation of the PEDOT layer at the sloped area. Also visible is the well defined disconnection of the PEDOT layer across the vertical step between slope and channel bottom (Figure 98 B).

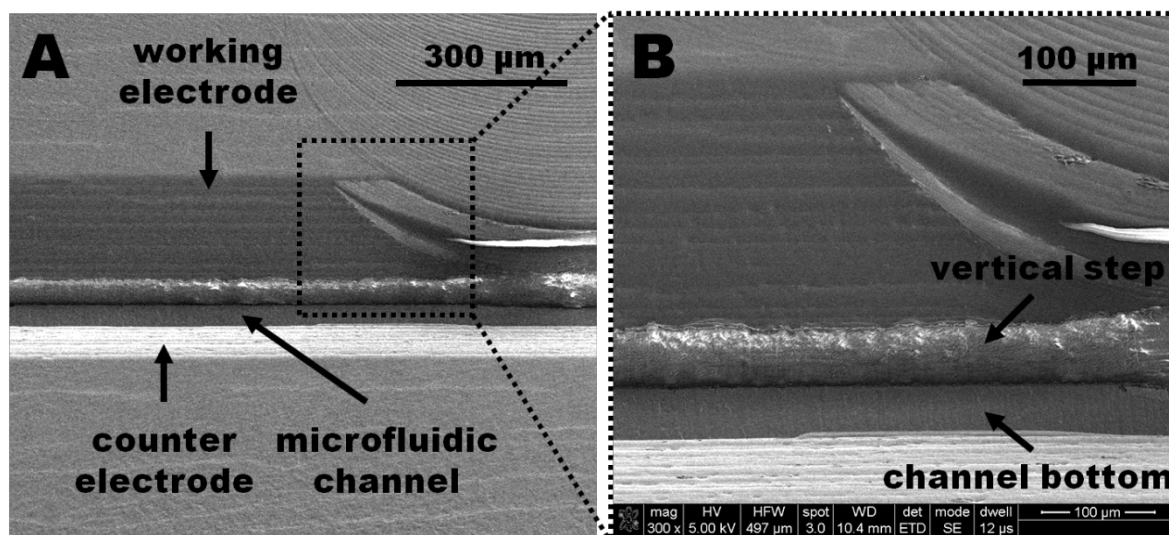


Figure 98: A) SEM image of an embossed electrochemical microfluidic system with focus on the working electrode (45° tilted) and B) a magnification presenting the right side of the working electrode, the lower part of the microfluidic channel and the vertical step between the electrode (slope) and the channel bottom.

5.3.5 Bonding of the Electrochemical Microfluidic System

The embossed microfluidic system was thermally bonded to a Ø50 mm TOPAS 5013 multi-well system (Figure 99 A). Four of the twelve wells were aligned with the embossed system: two to connect the inlet and outlet and two for electrical access to the electrodes (Figure 99 B).

The PEDOT around the electrode areas was previously removed in order to achieve a stable bond between the embossed wafer and the cover. Only PEDOT areas required for electrodes and electrical connection (5 mm wide and 10 mm long PEDOT stripes) were left on the TOPAS wafer. The removal was realized before embossing using adhesive tape, since a removal afterwards was extremely difficult.

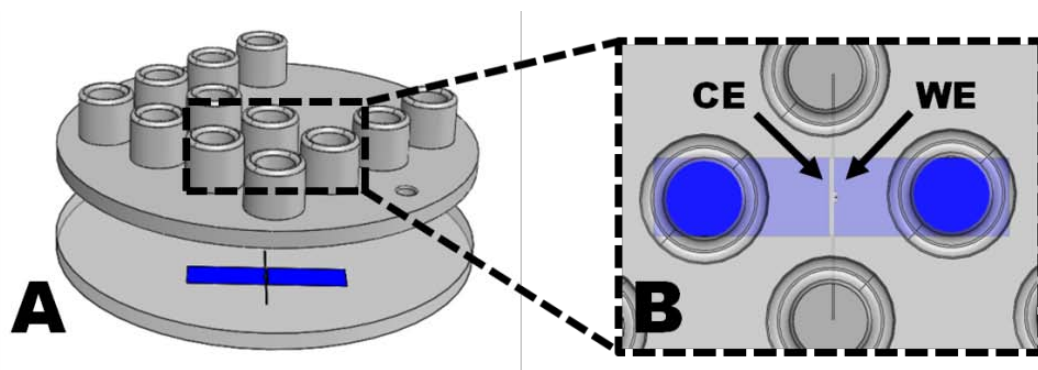


Figure 99: A) Alignment of the embossed electrochemical microfluidic system with a multi-well system before thermal bonding. B) Two wells were aligned with the inlet and outlet of the channel and two wells with the PEDOT area. The latter were used for inserting spring loaded metal pins to achieve electrical access to the working and counter electrode.

Thermal bonding was realized with the same press used for hot embossing. The bottom part with the embossed electrochemical microfluidic system and the multi-well system (lid) were aligned and placed between the heating elements of the press. For homogeneously applied pressure and heat distribution an aluminum holder with openings for the wells was used. Thereby, the pressure and heat were directly applied to the base plate of the lid. After heating up to a predefined temperature, a bonding pressure of 2.5 bar was applied and maintained for 600 s. The samples were cooled down to 60°C before the pressure was released and the samples removed from the press.

To achieve a stable bond, temperatures from 126°C to 130°C were investigated. Bonding quality was analyzed by manually injecting red ink into the wells. A possible bending of the lid into the channel during the bonding process was analyzed after mechanical separation of lid and bottom using a scalpel. The bending was calculated from recorded profiles of the lid.

Investigation of Bonding Quality

Figure 100 A shows a photograph of a complete electrochemical microfluidic system after thermal bonding at 128°C and injection of red ink. A magnification of the wells and the underlying electrochemical system is presented in Figure 100 B. No ink was observed around the connectors or along the channel. Microscope images of the systems bonded at 126°C, 128°C, and 130°C are presented in Figure 100 C - 101 E. For systems bonded at 126°C, red ink penetrated the interstice between both TOPAS wafers, indicating an uncompleted bonding. For bonding temperatures of 128°C to 130°C no leakage and therefore a sufficient bonding quality was observed.

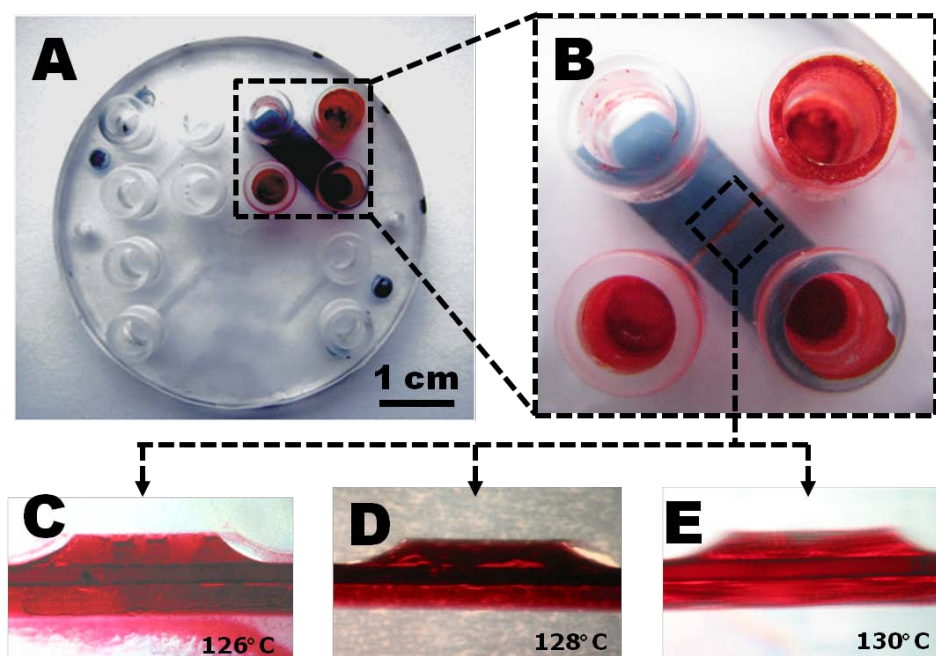


Figure 100: A) Photograph of a Ø 50 mm TOPAS wafer with an electrochemical microfluidic system, thermally bonded to a multi-well system and B) a magnification of the electrochemical system. Red ink was injected into the wells to analyze the bonding quality. Micrographs below present microfluidic channels at the place of the working electrode, bonded at C) 126°C, D) 128°C, and E) 130°C.

Investigation of the Lid Bending into the Channel

To analyze the bending of the lid into the channel during thermal bonding, bonded systems were mechanically opened using a scalpel. Profiles of lids were recorded by scanning the surface opposite to the electrode location (largest channel width). Recorded surface profiles are presented in Figure 101 A. For the quantification of the bending, the maximum distance of the profile to the baseline was measured.

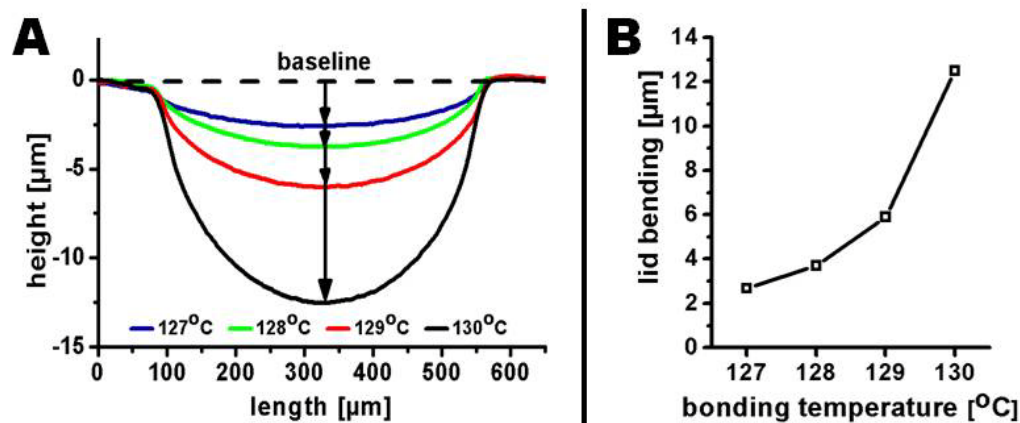


Figure 101: A) Profiles of lids in opposite to electrode location (largest channel width) for bonding temperatures of 127°C (blue), 128°C (green), 129°C (red), and 130°C (black). Inserted arrows define the position of the maximum lid bending (Note: different scaling for vertical and horizontal axis). B) Maximum lid bending calculated from profiles presented in (A).

A non-linear increase of the bending into the channel was observed within the analyzed bonding temperature range from 127°C to 130°C (Figure 101 B). For 127°C an absolute bending of 2.7 μm, for 128°C of 3.7 μm, for 129°C of 5.9 μm, and for 130°C of 12.5 μm were determined.

Profiles of the bended lids together with the embossed fluidic system are presented in Figure 102. Only the lid bending at 130°C influenced the channel and electrode dimensions by a notable penetration into the channel. The bending for remaining bonding temperatures is negligible for given system dimensions.

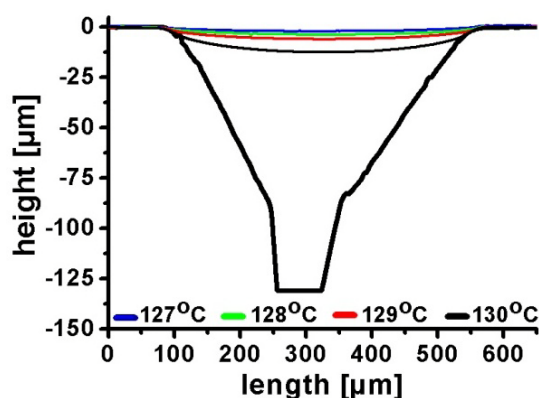


Figure 102: Profiles of the electrochemical system and lids after thermal bonding at 127°C (blue), 128°C (green), 129°C (red), and 130°C (black).

5.3.6 Glucose Detection

The electrochemical functionality and sensor applicability of the fabricated system was demonstrated by detecting different glucose concentrations in a buffer solution. Glucose oxidase is usually used for electrochemical detection of glucose. It is an enzyme with a high specificity for glucose and is commonly immobilized at the electrode surface. Glucose oxidase recognizes, binds and oxidizes glucose to gluconolactone. During this process the redox active center of the glucose oxidase is changed into a reduced state. In the presence of oxygen, the electrons from the redox active center will be transferred to the oxygen under formation of hydrogen peroxide. The hydrogen peroxide can be subsequently detected at the electrode.

A prussian blue working electrode allows a reduction of hydrogen peroxide at electrode potentials between -0.1 V and 0 V vs. $\text{Ag}|\text{AgCl}$ [Chiu, 2009]. The advantage of the low potential is that redox active substances like ascorbic and uric acids as well as some drugs (e.g. acetaminophen) present in analyte solutions like serum or blood samples, will only minimally interfere with the signal for the hydrogen peroxide [Wang, 2008]. The entire detection principle for glucose is summarized in Figure 103.

The immobilization of glucose oxidase by electrochemical deposition of a conducting polymer can be achieved e.g. by synthesis during cyclic voltammetry [Chiu, 2009; Fabiano, 2002], galvanostatic deposition (constant current) [Huang, 2007], or potentiostatic deposition (constant potential) [Piro, 2001; Zhu, 2005; Rohde, 1993].

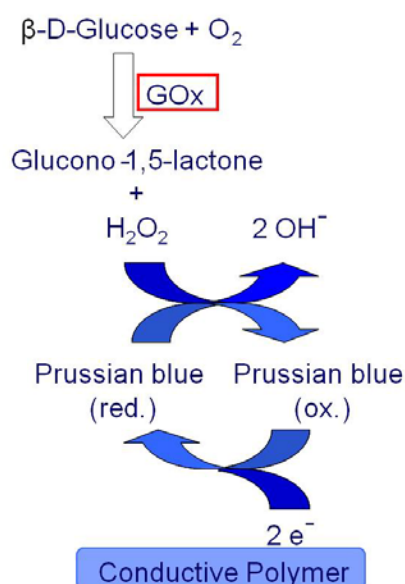


Figure 103: Electrochemical detection scheme for glucose: glucose oxidase (GOx) recognizes, binds and transforms glucose in the presence of oxygen to glucono-1.5-lactone and hydrogen peroxide. Prussian blue mediates the reduction of hydrogen peroxide. At an adequate electrode potential, the prussian blue can be renewed through reduction. The resulting reduction current is measured and used as sensor signal.

Experimental Parameters

The electrochemical setup was similar to the one used for tubular electrodes (Chapter 5.2.9). A tubing at the inlet connected the microfluidic channel to a pump. A disposable syringe tip was inserted into the well at the outlet and was used as waste container and to integrate a Ag|AgCl reference electrode into the system. Two spring loaded metal pins were inserted into the wells at the PEDOT films for electrical access of working and counter electrode.

PEDOT films were modified with prussian blue by adding 50 mg of the mediator to the polymerization solution before spin coating. Electropolymerization of polypyrrole took place in a 50 mM pyrrole solution containing 1200 units/ml glucose oxidase (Type II-S from *Aspergillus niger*, 39800 units/g, Sigma-Aldrich) under constant current conditions at 1 mA/cm^2 for 100 s.

Electrochemical experiments were carried out in freshly prepared 0.1 M potassium hydrogen phthalate/NaOH buffer (pH 5.5) (Sigma-Aldrich, >99%) using an Ag|AgCl reference electrode. Amperometric measurements were done at 0 mV vs. Ag|AgCl and at a flow rate of $150 \mu\text{l/min}$.

5.3.6.1 Amperometric Glucose Detection

Amperometric signals for injected glucose concentrations from 0.3 mM to 10 mM are presented in Figure 104 A. Before glucose solutions were injected, the base current for the buffer was recorded until stabilization was achieved. After injection of glucose solution for 700 s, the system was flushed with buffer to reestablish the initial baseline.

The current after establishment of a stable signal (steady state) was taken as sensor response for the corresponding glucose concentration. For comparison of different systems the absolute current change (baseline current with buffer subtracted from the current measured with glucose) was normalized to the signal of 10 mM glucose. The resulting calibration curve is presented in Figure 104 B. Different approaches to steady state are mainly based on the manually exchange of the syringes containing buffer or glucose solutions.

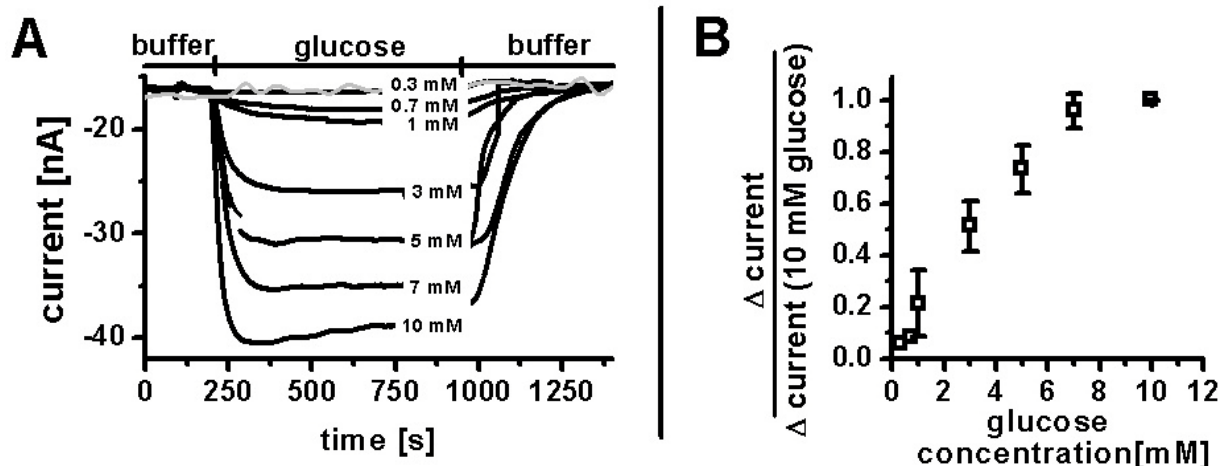


Figure 104: A) Amperometric signal of 0.3 mM, 0.7 mM, 1 mM, 3 mM, 5 mM, 7 mM, and 10 mM glucose solutions prepared with 0.1 M potassium hydrogen phthalate/NaOH buffer (pH 5.5), respectively, using a PEDOT / prussian blue / polypyrrole / glucose oxidase working electrode (black curves, top to down) and for 5 mM glucose solution using a PEDOT / prussian blue / polypyrrole working electrode (grey curve) as standard at 0 mV vs. Ag|AgCl. B) Signal amplitudes for each glucose concentration normalized to the amplitude at 10 mM).

A linear sensor range was found for glucose concentration of up to 8 mM. Glucose concentrations of 10 mM indicated a saturation of the signal. Injections of higher glucose concentration led to unstable and fluctuating signals, most likely due to oxygen depletion in the system [Wang, 2008]. A detection limit of 0.9 mM was determined in a lin-log data presentation by extrapolation of the linear range to the intersection with the x-axis as presented in Figure 105.

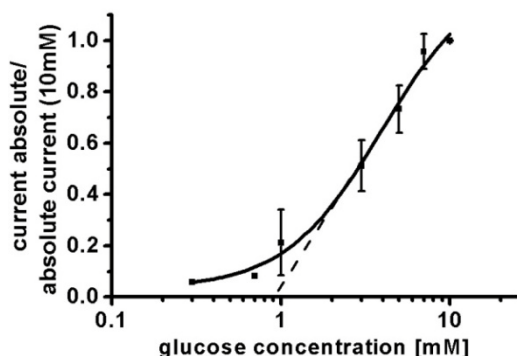


Figure 105: Normalized signal amplitudes for each glucose concentration to the amplitude of 10 mM in a lin-log data presentation. The dashed line extends the sensor detection range until intersection with x-axis which defines the lowest detection limit of the system.

The sensor range covers the normal physiological blood glucose concentrations of 3.5 to 7.8 mM [International diabetes institute]. Further optimization is required in order to achieve blood glucose concentration relevant for diabetes mellitus patients in the range of 8.3 and 16.6 mM [Chiu, 2009]. However, a comparison of the presented sensor characteristic with other research groups shows similar upper detection limits of about 10 mM glucose, independent of the electrochemical detection method [Chiu, 2009; Fabiano, 2002; Zhu, 2005; Retama, 2005].

5.3.7 Summary

A new approach towards fabrication of an electrochemical system by a one-step hot embossing process is presented. After application of a nanometer thick PEDOT layer on a TOPAS bulk material, the microfluidic pattern as well as the electrodes were defined in only one embossing step. Thereby, electrodes were integrated by embossing slopes into the channel sidewalls. Electrical disconnection of both electrodes was achieved by applying a height difference of 50 μm . Investigation of the highest possible slope angle showed that a 130 nm thick PEDOT layer obtained imperfections already at deformation angles above 15°. Embossing procedures at different molding temperatures led to similar results. An increase of the PEDOT layer thickness to 280 nm decreased the amount of imperfections and resulted in homogeneous electrode areas with slope angles of up to 30° to the surface plane.

An electrode modification with prussian blue and glucose oxidase enabled a reproducible glucose detection between 1 and 10 mM. A linear signal increase for glucose concentrations between 1 and 8 mM was recorded, which covers physiologically relevant blood concentration between 3.5 and 7.8 mM.

5.3.8 References

- [Becker and Gärtner, 2008] Becker, H.; Gärtner, C. *Analytical and bioanalytical chemistry* **2008**, *390*, 89-111
- [Ceriotti, 2007] Ceriotti, L.; Ponti, J.; Broggi, F.; Kob, a.; Drechsler, S.; Thedinga, E.; Colpo, P.; Sabbioni, E.; Ehret, R.; Rossi, F. *Sensors and Actuators B: Chemical* **2007**, *123*, 769-778
- [Chen, 2003] Chen, B.; Cui, T.; Liu, Y.; Varahramyan, K. *Solid-State Electronics* **2003**, *47*, 841-847

- [Chen, 2011] Chen, I.-J.; White, I. M. *Biosensors & bioelectronics* **2011**, *26*, 4375-81
- [Cheng, 2010] Cheng, W.; Klauke, N.; Smith, G.; Cooper, J. M. *Electrophoresis* **2010**, *31*, 1405-13
- [Chiu, 2009] Chiu, J.-Y.; Yu, C.-M.; Yen, M.-J.; Chen, L.-C. *Biosensors & bioelectronics* **2009**, *24*, 2015-20
- [Fabiano, 2002] Fabiano, S.; Tran-Minh, C.; Piro, B.; Dang, L. A.; Pham, M. C.; Vittori, O. *Materials Science and Engineering: C* **2002**, *21*, 61-67
- [Frey, 2011] Frey, O.; van der Wal, P. D.; Spieth, S.; Brett, O.; Seidl, K.; Paul, O.; Ruther, P.; Zengerle, R.; de Rooij, N. F. *Journal of neural engineering* **2011**, *8*, 066001
- [Ges, 2010] Ges, I. a; Baudenbacher, F. *Biosensors & bioelectronics* **2010**, *26*, 828-33
- [Goral, 2011] Goral, V. N.; Hsieh, Y.-C.; Petzold, O. N.; Faris, R. a; Yuen, P. K. *Journal of Micromechanics and Microengineering* **2011**, *21*, 017002
- [Hansen, 2006] Hansen, T. S.; West, K.; Hassager, O.; Larsen, N. B. *Synthetic Metals* **2006**, *156*, 1203-1207
- [Hansen, 2007] Hansen, T. S.; West, K.; Hassager, O.; Larsen, N. B. *Advanced Materials* **2007**, *19*, 3261-3265
- [Heckele, 2004] Heckele, M.; Schomburg, W. K. *Journal of Micromechanics and Microengineering* **2004**, *14*, R1-R14
- [Huang, 2007] Huang, C.-J.; Chen, Y.-H.; Wang, C.-H.; Chou, T.-C.; Lee, G.-B. *Sensors and Actuators B: Chemical* **2007**, *122*, 461-468
- [Illa, 2010] Illa, X.; Ordeig, O.; Snakenborg, D.; Romano-Rodríguez, A.; Compton, R. G.; Kutter, J. P. *Lab on a chip* **2010**, *10*, 1254-61
- [Jena, 2011] Jena, R. K.; Chester, S. a.; Srivastava, V.; Yue, C. Y.; Anand,

- L.; Lam, Y. C. *Sensors and Actuators B: Chemical* **2011**, *155*, 93-105
- [Kawase, 2003] Kawase, T. *Thin Solid Films* **2003**, *438-439*, 279-287
- [Kiilerich-Pedersen, 2011] Kiilerich-Pedersen, K.; Poulsen, C. R.; Jain, T.; Rozlosnik, N. *Biosensors and Bioelectronics* **2011**, *28*, 386-392
- [Lee, 2001] Lee, G.-B.; Chen, S.-H.; Huang, G.-R.; Sung, W.-C.; Lin, Y.-H. *Sensors and Actuators B: Chemical* **2001**, *75*, 142-148
- [Liedert, 2012] Liedert, R.; Amundsen, L. K.; Hokkanen, A.; Mäki, M.; Aittakorpi, A.; Pakanen, M.; Scherer, J. R.; Mathies, R. a; Kurkinen, M.; Uusitalo, S.; Hakalahti, L.; Nevanen, T. K.; Siitari, H.; Söderlund, H. *Lab on a chip* **2012**, *12*, 333-339
- [Mire, 2011] Mire, C. a.; Agrawal, A.; Wallace, G. G.; Calvert, P.; in het Panhuis, M. *Journal of Materials Chemistry* **2011**, *21*, 2671
- [Ng, 2009] Ng, S. H.; Wang, Z. F. *Microsystem Technologies* **2009**, *15*, 1149-1156
- [Pemg, 2009] Pemg, B.-Y.; Wu, C.-W.; Shen, Y.-K.; Lin, Y. *Polymers for Advanced Technologies* **2009**, *21*, 457-466
- [Piro, 2001] Piro, B.; Dang, L. A.; Pham, M. C.; Fabiano, S.; Tran-Minh, C. *Journal of Electroanalytical Chemistry* **2001**, *512*, 101-109
- [Qi, 2002] Qi, S.; Liu, X.; Ford, S.; Barrows, J.; Thomas, G.; Kelly, K.; McCandless, A.; Lian, K.; Goettert, J.; Soper, S. a *Lab on a chip* **2002**, *2*, 88-95
- [Retama, 2005] Retama, J. R.; Mecerreyes, D.; Lopez-Ruiz, B.; Lopez-Cabarcos, E. *Colloids and Surfaces A: Physicochemical and Engineering Aspects* **2005**, *270-271*, 239-244
- [Rohde, 1993] Rohde, E.; Dempsey, E.; Smyth, M. R.; Vos, J. G.; Emons, H. *Structure* **1993**, *278*, 5-16
- [Schrödner, 2005] Schrödner, M.; Stohn, R.-I.; Schultheis, K.; Sensfuss, S.; Roth,

H.-K. *Organic Electronics* **2005**, *6*, 161-167

- [Tobjörk, 2011] Tobjörk, D.; Österbacka, R. *Advanced materials (Deerfield Beach, Fla.)* **2011**, *23*, 1935-61
- [Wang, 2008] Wang, J. *Chemical reviews* **2008**, *108*, 814-25
- [Wang, 2011] Wang, X.; Zhang, L.; Chen, G. *Analytical and bioanalytical chemistry* **2011**, *401*, 2657-65
- [Yeo, 2009] Yeo, L. P.; Ng, S. H.; Wang, Z.; Wang, Z.; de Rooij, N. F. *Microelectronic Engineering* **2009**, *86*, 933-936
- [Yeo, 2010] Yeo, L. P.; Ng, S. H.; Wang, Z. F.; Xia, H. M.; Wang, Z. P.; Thang, V. S.; Zhong, Z. W.; de Rooij, N. F. *Journal of Micromechanics and Microengineering* **2010**, *20*, 015017
- [Zhu, 2005] Zhu, M.; Jiang, Z.; Jing, W. *Sensors and Actuators B: Chemical* **2005**, *110*, 382-389

Chapter 6

Conclusions

The objective of the project was to establish new strategies for the fabrication of all-polymer electrochemical sensors. Three different systems were established based on conducting polymers using novel fabrication methods:

Arrays of circular electrodes were successfully fabricated by using a novel fast prototyping strategy useful to validate simulated results on real systems before mass production of electrode arrays.

Microelectrode arrays were fabricated by resistance-controlled microdrilling through a protective insulating polymer layer down to, but not through, an underlying layer of the highly conductive polymer PEDOT. Resistance-controlled microdrilling allows very precise determination of the physical contact between the drilling tool and the PEDOT layer by a significant drop in the continuously monitored electrical resistance between both. Without an extremely precise drilling process it would be easily possible to fracture the few micrometer thick PEDOT layer. Multiple microelectrode arrays with minimum electrode widths and separations of 30 μm were prototyped.

The individual amperometric responses of each microelectrode array at steady state corresponded in general with results obtained from finite element modeling. However, the experimentally determined rate of approach to steady state was significant slower than the modeled kinetics. The discrepancy in time could be attributed to the electrochemical activity of the PEDOT electrodes themselves. The subtraction of the contribution from the PEDOT electrode led to an excellent agreement of time scales and current levels between the models and the experiments.

Arrays of tubular electrodes were fabricated by drilling through a 150 μm thick TOPAS 5013 foil coated with a tri-layer of polystyrene, PEDOT and polystyrene. The drilling process resulted in tubular electrodes integrated in the drilling shaft with an average diameter of $101.4 \pm 1.6 \mu\text{m}$ and height of $370 \pm 60 \text{ nm}$. An additional modification of the backside of the TOPAS foil with a polystyrene layer and another PEDOT layer allowed the simultaneous fabrication of a second electrode which was used as counter electrode. By using the drilling shaft as microfluidic channel, the assembly allowed the formation of an entire electrochemical microfluidic system with two integrated polymer electrodes by a single drilling step. Multiple drilling steps resulted in homogenous tubular electrode arrays. Drilling of arrays consisting of ten tubular electrodes typically lasted about 20 s.

The reproducibility of the fabrication method was confirmed by consistent amperometric responses of independently fabricated electrode arrays towards potassium ferrocyanide within

a concentration range from 1 to 300 mM. The detection of hydrogen peroxide in a concentration range from 0.1 to 5 mM after modification of the PEDOT layer with prussian blue demonstrated its use as a sensor. The linear response regime of the sensor was within a concentration range of 0.1 to 1 mM with a sensitivity of 8.6 nA/mM.

Planar electrodes were fabricated by hot embossing of a microfluidic channel with partly sloped sidewalls (angle of 30°) into a 280 nm thick PEDOT layer on top of a TOPAS bulk substrate. During embossing the PEDOT layer on the sloped sidewalls became part of the channel while retaining electrical contact to the top layer. Consequently, the PEDOT layer at the sloped areas could be used as electrodes. Electrodes placed on opposite channel sidewalls were spatially separated by a 100 μm wide microfluidic channel in between. The electrical insulation of the PEDOT electrodes from the PEDOT at the channel bottom was achieved by embossing a vertical step of 50 μm.

Stamps for hot embossing of planar electrodes were made from aluminum using micromilling. Micromilling was the method of choice since the innovative sensor design with combined straight as well as sloped surfaces could be comparably easy fabricated. Highly optimized equipment and process parameters allowed the fabrication of structures down to 10 μm in height. A high precision of the milling process was crucial to fabricate slopes with a high surface finish in order to avoid fracturing of the embossed PEDOT layer.

A PEDOT layer thickness of 280 nm was necessary to achieve homogeneous PEDOT areas on 30° sloped surfaces. For lower thicknesses cracks in the PEDOT layers were observed. Thicker PEDOT layers did not allow embossing of higher slope angles. Cracks and imperfections in the embossed region were observed. Higher slope angles were also not achieved by a variation of the molding temperature.

The final, thermally bonded electrochemical microfluidic systems were used as amperometric glucose sensors. The responses towards glucose concentrations in the range from 1 to 10 mM were recorded after a modification of the PEDOT layer with prussian blue and immobilization of glucose oxidase at the working electrodes. The linear signal range of the fabricated sensors for glucose concentration was 1 to 8 mM, which covers physiologically relevant blood concentrations between 3.5 and 7.8 mM.

The developed novel fabrication strategies demonstrate the advantage of using conducting polymers in electrochemical microfluidic systems. Structuring methods, already established for non-conducting polymers, were used to prototype electrodes in conducting polymers simultaneously during the formation of the microfluidic system.

Designs of the two presented electrochemical microfluidic systems with tubular as well as planar electrodes were developed towards possible mass fabrication. The presented stack assembly demonstrates the possibility of a one step fabrication of tubular electrode based electrochemical microfluidic systems. The developed design of the hot embossed electrochemical microfluidic system should be directly applicable for a mass fabrication. Certainly, it would be required to change from flat-to-flat to roll-to-roll embossing, but without changes in the design.

Due to the electrochemical contribution of the polymer itself, conducting polymers experience a slow approach to steady state during amperometric measurements. This mainly limits the use of conducting polymers to applications where fast current responses are not required. A reference system in parallel to the measurement cell would be necessary to achieve steady state signals by forming the difference between the currents of the reference system and these of the sensor.

Sensor applicability of the fabricated electrochemical microfluidic systems was demonstrated for tubular electrodes by detecting hydrogen peroxide and, for embossed electrodes by detecting glucose. Especially the latter shows the importance of presented results. Further sensor analysis and optimization is required, especially regarding interferences on the signal, ability of glucose measurements in real plasma or blood sample, and long term stability. However, the detection range of the fabricated glucose sensors covers physiologically relevant blood concentration of non-diabetes mellitus patients which is a promising result for future applications.

The application of the fabricated electrochemical systems is not limited to glucose sensors. Electrode modifications with other recognition elements would enable a wide range of possible applications for these fast producible systems in fields of clinical, industrial, environmental, and agricultural analysis.

Appendix

Publication 1

Published in Microelectronic Engineering (2010)

*Title: Fabrication of an all-polymer electrochemical sensor
by using a one-step hot embossing procedure*

Authors: Jan Kafka, Niels B. Larsen, Steen Skaarup, Oliver Geschke



Fabrication of an all-polymer electrochemical sensor by using a one-step hot embossing procedure

Jan Kafka^{a,*}, Niels B. Larsen^a, Steen Skaarup^b, Oliver Geschke^a

^a Department of Micro and Nanotechnology, Technical University of Denmark, Bld. 345e, DK-2800 Kgs. Lyngby, Denmark

^b Department of Chemistry, Technical University of Denmark, Bld. 345e, DK-2800 Kgs. Lyngby, Denmark

ARTICLE INFO

Article history:

Received 14 September 2009

Received in revised form 19 November 2009

Accepted 25 November 2009

Available online 4 December 2009

Keywords:

Polymer

Electrochemical sensor

Hot embossing

PEDOT

Glucose detection

ABSTRACT

We present a fast one-step hot embossing procedure for fabricating an all-polymer electrochemical sensor based on a thin, conductive film of poly(3,4-ethylenedioxythiophene) (PEDOT), a few 100s of nanometers in thickness, polymerised on top of a non-conductive TOPAS[®] (Cyclic Olefin Copolymer) carrier material. A microfluidic channel was embossed into this two component system. Working (WE) and counter (CE) electrode were integrated into the channel by embossing slopes into the channel sidewalls. Since both electrodes were placed at opposite channel sidewalls, electrical disconnection of electrodes was achieved by spatial separation (Fig. 1). Functionality of the electrochemical system was shown by amperometric detection of physiologically relevant glucose concentrations (0–10 mM).

© 2009 Elsevier B.V. All rights reserved.

1. Introduction

The application of electrochemical microfluidic systems in many fields of biological and chemical analysis is an attractive route to enable high throughput analysis. Replacement of standard metal electrodes by inexpensive conductive polymers like polypyrrole or poly(3,4-ethylenedioxythiophene) (PEDOT) allows a further price reduction and gives furthermore access to fast and easy polymer structuring processes like laser ablation [1,2] and hot embossing [3,4]. Finally the functionalisation of a polymer electrode with a biological recognition element allows the construction of a specific, mass producible and noble-metal free detection electrode [5,6].

We present a fast one-step method for simultaneous patterning of the electrodes and shaping the microchannels of an all-polymer electrochemical sensor, applicable to, e.g., glucose detection.

2. Experimental

All PEDOT films were synthesised by spin coating 0.7 ml of a solution containing 2.166 ml CLEVIOS[™] C-B50 (H.C. Starck), 0.666 ml ultra-pure water (≥ 18 M Ω cm), 0.05 ml pyridine (Fluka, 99%), and 0.08 ml CLEVIOS[™] M V2 (H.C. Starck, >98%) on a Ø50 mm TOPAS[®] 5013 wafer (Technical University of Denmark) at 1000 rpm for 60 s. For PEDOT films used for glucose detection

0.05 g prussian blue (soluble, Fluka) was added to the solution. To speed up the polymerisation and evaporate remaining solvents all substrates were annealed for 15 min at 65 °C. Finally the substrates were washed with deionised water and dried under a nitrogen stream.

Stamps for hot embossing experiments were milled in aluminium using a desktop milling machine Mini-Mill/3PRO from Minitech. Hot embossing was realised at 150 °C and 7.6 bars for 5 min. Stamp quality was controlled by measuring the profile with a Dektak 8 profilometer with a 5 μ m radius stylus and a force of 5 mg. Replicas were analysed by two-point probe electrical measurements and structural characterization by profilometry and scanning electron microscopy.

Thermal bonding was carried out at 128 °C and 2.5 bar for 10 min after removing the PEDOT layer around the areas of interest by adhesive tape. For thermal bonding a Ø50 mm TOPAS[®] 5013 wafer with integrated female luer connectors (Technical University of Denmark) was used as cover.

All electrochemical experiments were carried out in freshly prepared 0.1 M potassium hydrogen phthalate/NaOH buffer (pH 5.5) (Sigma–Aldrich, >99%) using an Ag|AgCl|3M KCl reference electrode placed at the inlet of the system. Electropolymerisation of polypyrrole took place in a 0.05 M pyrrole solution containing 1200 units/ml glucose oxidase (Type II-S from *Aspergillus niger*, 39,800 units/g, Sigma–Aldrich) under constant current conditions. Amperometric measurements were done at 0 mV vs. Ag|AgCl|3M KCl and at a flow rate of 150 μ l/min.

* Corresponding author. Tel.: +45 4525 5852; fax: +45 4588 6313.

E-mail address: Jan.kafka@nanotech.dtu.dk (J. Kafka).

3. Results and discussion

In order to apply a homogeneous single PEDOT layer on a Ø50 mm TOPAS® 5013 wafer, untreated as well as acetone, isopropanol, and ethanol cleaned TOPAS® substrates were investigated. To analyse the thickness and homogeneity of the PEDOT layers three different wafers for each cleaning procedure were measured at five different points across the surface. PEDOT layer thicknesses of 130 ± 9 nm for untreated, 136 ± 7 nm for acetone, 126 ± 4 nm for isopropanol, and 128 ± 8 nm for ethanol cleaned TOPAS® substrates were recorded. So, apart from a slightly smaller deviation for an isopropanol cleaned surface there were no differences in the layer thicknesses. However in further experiments ethanol cleaned substrates were processed to avoid possible handling contaminations of the TOPAS® substrates.

A microfluidic system was formed by embossing a 100 µm wide and 150 µm deep groove into the PEDOT (conductive) covered TOPAS® (non-conductive). Simultaneously, the electrodes were structured and integrated into the channel system by embossing two slopes into the channel sidewall. Thereby a two-electrode system (counter (CE) and working (WE) electrode) was formed (Figs. 1–3).

Fig. 2 shows that the electrodes were spatially separated by applying a step height in between. A variation of the channel width and height showed that neighbouring PEDOT areas separated by up to 200 µm were fully electrically disconnected only if the region in between was embossed by at least 50 µm.

In order to integrate the electrodes by embossing slopes into the channel side walls the stretching behaviour of the PEDOT network needed to be analysed. Slope angles in the range of 15–60° from the surface plane were investigated. A single PEDOT layer of 128 ± 8 nm thickness starts to crack at a deformation angle of more than 15° resulting in an inhomogeneous electrode surface. Total loss of conductivity was obtained at higher deformation angles. Hansen et al. [7] increased the stretchability of PEDOT by integration into polyurethane while retaining conductivity. To increase the stretchability PEDOT was integrated into TOPAS® as shown by Hansen et al. [8]. However, the integration of PEDOT into TOPAS® resulted in a decreased stretchability and therefore a loss of conductivity already at a deformation angle of 15°.

The application of a second PEDOT layer on top of a single layer resulted in an increase in thickness to 305 ± 25 nm as well as in an increased stretchability. By using a double layer, deformation angles of up to 30° without any defects in the embossed area were

Nr.	Process step	Illustration
1	Cleaned non-conductive TOPAS® substrate (light gray)	
2	Spin on of a thin, conductive PEDOT layer (black)	
3	One step hot embossing procedure to define microfluidics and electrode structures using a Al-stamp (dark grey)	
4	Sealing the system by thermal bonding of a TOPAS® lid	

Fig. 1. Process flowchart.

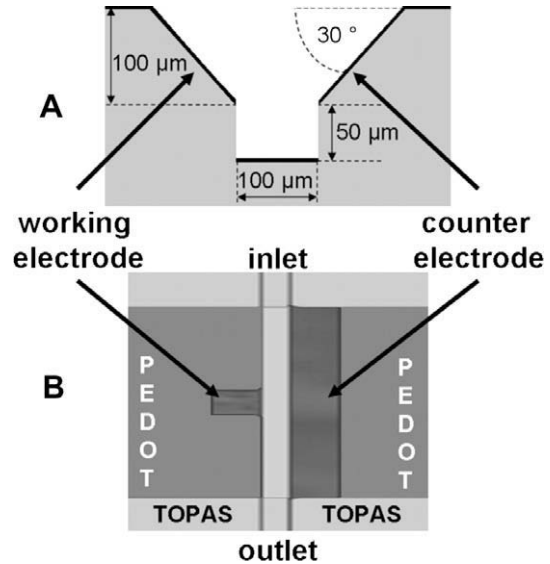


Fig. 2. Design of the microfluidic system with integrated WE and CE. Electrodes are defined as slopes at the channel sidewalls and electrically disconnected by simultaneous embossing a steep channel in between. (A) Scheme of cross section and (B) top view.

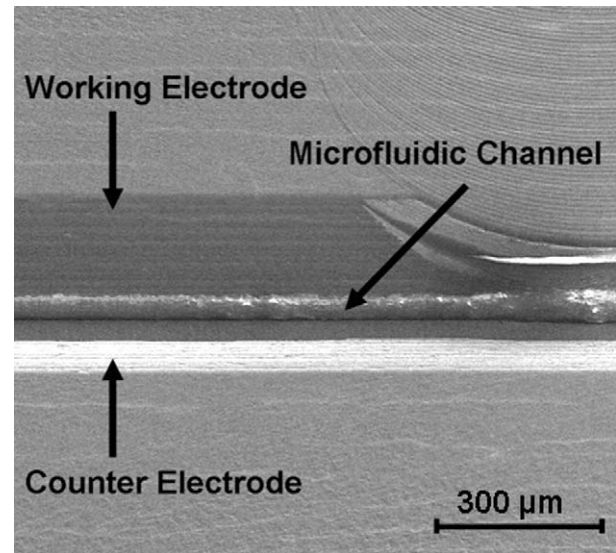


Fig. 3. SEM of an embossed electrochemical fluidic system with integrated electrodes at the channel sidewalls (tilted 45°).

achieved. A further increase of stretchability by applying a third PEDOT layer was not investigated due to decreased homogeneity of the PEDOT layer thickness (470 ± 45 nm) and a commencing crystallisation.

The embossed microfluidic system was sealed by thermal bonding using a Ø50 mm TOPAS® 5013 wafer with integrated female luer connectors as cover. Luer connectors were used to connect the microfluidic pattern to a pump as well as for integrating spring loaded metal pins for connecting the PEDOT electrodes. In order to achieve a proper sealing, PEDOT areas around the embossed fluidic system needed to be removed. Thermal deformation of the lid resulted in a bending of the lid into the channel. For 128 °C which was sufficient to achieve a stable bonding a maximum bending expansion of 3.7 µm was found in the middle of the channel. However for the chosen system dimensions this bending is negligible.

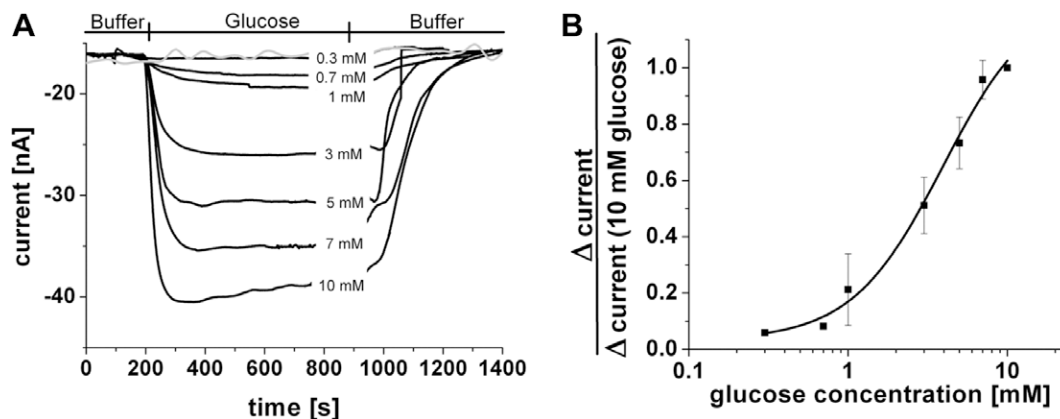


Fig. 4. (A) Amperometric signal of 0.3 mM, 0.7 mM, 1 mM, 3 mM, 5 mM, 7 mM, and 10 mM glucose solutions prepared with 0.1 M potassium hydrogen phthalate/NaOH buffer (pH 5.5), respectively, using a PEDOT/prussian blue/polypyrrole/glucose oxidase working electrode (black curves, top to down) and for 5 mM glucose solution using a PEDOT/prussian blue/polypyrrole working electrode (grey curve) as standard at 0 mV vs. Ag|AgCl|3M KCl. (B) Signal amplitudes for each glucose concentration normalised to the amplitude at 10 mM.

An application of the system was demonstrated by sensing glucose after a modification of the WE: by incorporating of prussian blue as an electron mediator into the PEDOT layer an electrode sensitive to hydrogen peroxide was fabricated. Subsequent immobilization of glucose oxidase (GOD) by electropolymerisation of polypyrrole on top of the WE resulted in a glucose sensitive electrode. Amperometric measurements while injecting glucose concentrations in a random order from 0.3 mM to 10 mM resulted in a reduction current characteristic of the glucose concentration (Fig. 4A). A further increase of glucose concentration led to an unstable signal most likely due to oxygen depletion in the system. Normalisation of the absolute current (baseline current with buffer in the channel subtracted from the current measured with analyte) for each concentration to the saturated signal at 10 mM glucose resulted in a calibration curve for the sensor with a linear range from 2 mM to 8 mM in a lin–log data presentation. The detection limit of 0.9 mM was found by extrapolation of the linear range to the intersection with the x-axis (Fig. 4B).

4. Summary

We have presented a new approach to an electrochemical system which was fabricated in only one hot embossing step. At first a thin layer of PEDOT was spin coated on a Ø50 mm TOPAS® wafer. Ethanol treatment of the TOPAS® substrate before spin coating prevented handling contaminations and allowed synthesis of reproducible and homogeneous PEDOT layers. In the following embossing step the microfluidic pattern as well as the electrodes were defined. Thereby electrodes were integrated by embossing slopes into the channel sidewalls. Electrical disconnection of both

electrodes was achieved by applying a height difference of at least 50 µm in between. An investigation of the highest possible slope angle showed that a single PEDOT layer already starts to crack at a deformation angle above 15°. The deformation angle could be increased up to 30° by applying a double PEDOT layer. A decreased angle was observed after integration of the PEDOT layer into TOPAS®.

After modification of the electrodes reproducible glucose detection between 0 and 10 mM was proven. The sensor behaviour in the physiological relevant concentration interval between 3.5 and 7.8 mM (International Diabetes Institute) is approximately linear vs. the logarithm of the concentration.

Acknowledgement

This work was financially supported by the Danish Research Council for Technology and Production Sciences. Grant No. 26-04-0074.

References

- [1] J. Bargon, R. Baumann, *Microelectronic Engineering* 20 (1993) 55–72.
- [2] D. Yuan, S. Dasa, *Journal of Applied Physics* 101 (2) (2007) 24901–24906.
- [3] H. Becker, C. Gärtner, *Analytical and Bioanalytical Chemistry* 390 (2008) 89–111.
- [4] Y.K. Shen, J.D. Lin, R.H. Hong, *Polymer Engineering and Science* 49 (2009) 104–114.
- [5] F.R.R. Teles, L.P. Fonseca, *Materials Science and Engineering* 28 (2008) 1530–1543.
- [6] N.K. Guimarda, N. Gomez, C.E. Schmidt, *Progress in Polymer Science* 32 (2007) 876–921.
- [7] S.T. Hansen et al., *Synthetic Metals* 157 (2007) 961–967.
- [8] S.T. Hansen et al., *Synthetic Metals* 156 (2006) 1203–1207.

Publication 2

Published in Microelectronic Engineering (2011)

*Title: Fast prototyping of conducting polymer microelectrodes
using resistance-controlled high precision drilling*

Authors: Jan Kafka, Oliver Geschke, Steen Skaarup, Niels B. Larsen



Fast prototyping of conducting polymer microelectrodes using resistance-controlled high precision drilling

Jan Kafka^{a,*}, Oliver Geschke^a, Steen Skaarup^b, Niels B. Larsen^a

^a Department of Micro and Nanotechnology, Technical University of Denmark, Ørstedts Plads, Building 345e, DK-2800 Kgs. Lyngby, Denmark

^b Department of Chemistry, Technical University of Denmark, Ørstedts Plads, Building 345e, DK-2800 Kgs. Lyngby, Denmark

ARTICLE INFO

Article history:

Available online 15 February 2011

Keywords:

Polymer fast prototyping
Microelectrode array
Microdrilling
Polymer
PEDOT
Finite element modeling

ABSTRACT

We present a straightforward method for fast prototyping of microelectrode arrays in the highly conductive polymer poly(3,4-ethylenedioxythiophene) (PEDOT). Microelectrode arrays were produced by electrical resistance-controlled microdrilling through an insulating polymer layer (TOPAS[®] 5013) covering a PEDOT layer. The sudden drop in electrical resistance between the metal drill and the PEDOT layer upon physical contact was employed as stop criterion for the drilling process. Arrays of 3 × 3 microelectrodes of diameter 30 μm or 100 μm, respectively, and having center-to-center electrode spacings of 130 μm and 300 μm, respectively, were fabricated. Their functionality was verified by chronoamperometry on potassium ferro-/ferricyanide. Comparison of the experimentally obtained results to finite element modeling of the respective electrode configurations shows that the conducting polymer electrodes approach the steady state currents predicted from modeling, but at a much slower rate than expected. This is shown to be caused by the use of electroactive PEDOT electrodes. Subtraction of the latter contribution gives approach to steady state currents within a few seconds, which is in very good agreement with the modeled response time.

© 2011 Elsevier B.V. All rights reserved.

1. Introduction

The recent availability of stable and processable highly conducting polymers has enabled the fabrication of low-cost all-polymer chips for electrochemical analysis with integrated polymer microelectrodes [1]. Microelectrodes are increasingly preferred over macroelectrodes due to faster response times and better signal-to-noise ratios [2]. A disadvantage is the low currents associated with individual microelectrodes. Arranging microelectrodes in arrays increases the signal while retaining the electrochemical advantages of a single electrode. This, however, is only valid for a proper array design. A number of simulation tools are available for the analysis of array configurations in order to avoid interference between two neighboring electrodes, for instance by the overlapping of diffusion radii. Fast prototyping strategies are necessary to corroborate the simulated results with real systems before an electrode array design can be mass produced for a practical application, in particular for conducting polymer electrodes where the electrode material itself can contribute to the measurement [3]. We present a facile fabrication method for prototyping arrays of circular polymer microelectrodes using a desktop milling machine. Proof of electrochemical functionality is demonstrated by

recording the electrochemical response to potassium ferrocyanide after integration into an electrochemical cell. The experimental results are verified against finite element modeling of the microelectrode arrays.

2. Experimental

PEDOT films were produced by repeated application of PEDOT layers to a freshly ethanol-cleaned polymer substrate: each layer was synthesized by spin coating 0.5 ml of a solution containing 2.166 ml CLEVIOS[™] C-B50 (H.C. Starck), 0.666 ml ultra-pure water ($\geq 18 \text{ M}\Omega \text{ cm}$), 0.05 ml pyridine (Fluka, 99%), and 0.08 ml CLEVIOS[™] M V2 (H.C. Starck, >98%) onto an injection molded Ø 50 mm disc (TOPAS[®] 5013, Topas Advanced Polymers) at 500 rpm for 40 s. Before application of the next layer, the substrate was baked at 65 °C for 15 min to increase the polymerization rate and to evaporate remaining solvent, followed by washing with deionized water and drying in a stream of nitrogen. The process was repeated 12 times to form a 3.5 μm thick PEDOT: tosylate film, as measured by profilometry (Dektek 8, Veeco Instruments). An electrically insulating coating was applied to the PEDOT film by spin coating a solution of 40 wt.% TOPAS[®] 5013 in toluene/tetrahydrofuran (1:1) at 500 rpm for 1 min, to form a layer of average thickness 7.5 μm as measured by profilometry. Electrical access to the TOPAS[®]-coated PEDOT layer was secured by masking a small area

* Corresponding author.

E-mail address: Jan.Kafka@nanotech.dtu.dk (J. Kafka).

of the PEDOT film by adhesive tape during the TOPAS[®] coating step.

Electrochemical experiments were carried out in freshly prepared aqueous solutions of 0.1 M KCl (Sigma–Aldrich, >99%) containing potassium ferri-/ferrocyanide (Sigma–Aldrich). Analysis on \varnothing 100 μm electrodes used an initial ferri-/ferrocyanide concentration of 1 mM (of each species), while 5 mM (of each species) was used on \varnothing 30 μm electrodes to increase the signal intensity. A Ag|AgCl|3 M KCl reference electrode and a platinum counter electrode were placed at the inlet of the system. To avoid bubbles on the electrodes, the cells were rinsed with an aqueous solution having low surface tension (40 wt.% ethanol/water [4]) followed by rinsing three times with pure water before being filled with the KCl solution.

The microelectrode arrays were modeled in a 3D solution environment using the finite modeling package COMSOL 4 (COMSOL AB, Stockholm). The electrodes were modeled as perfect sinks of the solute at an otherwise mass transport insulated “floor” of a $2 \times 2 \times 2 \text{ mm}^3$ simulation box. The solute concentration at the four side walls and at the ceiling was fixed to be at the initial concentration. The experimental conditions were mimicked by modeling the \varnothing 100 μm electrodes using 1 mM solute and the \varnothing 30 μm electrodes using 5 mM solute (diffusion constant of $8 \times 10^{-10} \text{ m}^2/\text{s}$ [5]). Both steady state and time dependent (up to 90 s) conditions were investigated. The molar flux across the microelectrodes was converted to a current given that one electron is transferred for the reaction of each ferrocyanide ion.

Quantitative analysis of electrode dimensions were performed on three independent samples, and chronoamperometric measurements were performed on four independent samples. Results of both types of analysis are presented as the average mean and standard deviation.

3. Results and discussion

Microelectrodes were fabricated by stepwise drilling through the electrically insulating TOPAS[®] layer to the electrically conducting PEDOT layer, as illustrated in Fig. 1. The process proceeded in steps of 0.5 μm using a desktop computer controlled milling machine (Mini-Mill/3PRO, Minitech) running at 500 rpm with \varnothing 30 μm or \varnothing 100 μm flat end milling tools. The end-point of the drilling process was determined by a sharp decrease in electrical resistance from infinity to approximately 20 k Ω upon physical contact between the rotating tool and the PEDOT film. After contact, one additional drilling step of 0.5 μm depth was performed to ensure complete removal of the TOPAS[®] coating above the electrode area.

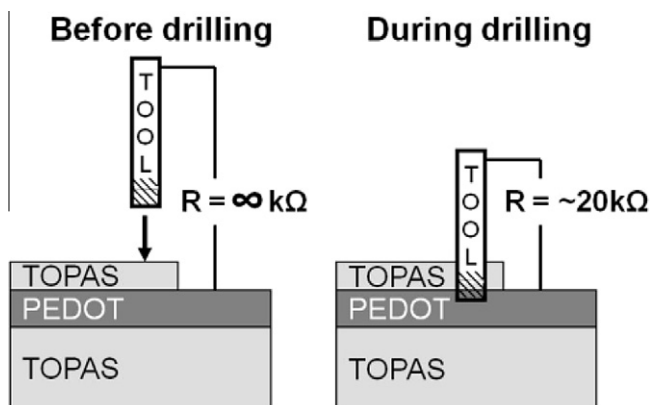


Fig. 1. Schematic of the resistance-controlled drilling process: drilling proceeds through the insulating cover layer until electrical contact is made with the conductive polymer layer.

The control software of the milling machine was employed to control spacing and separation of the multiple electrode arrays on each TOPAS[®]/PEDOT-coated substrate. Arrays were produced with center-to-center spacings of 130 μm and 300 μm , respectively. Milling of a single 3×3 array typically lasted 10 min. The final patterned substrate was bonded to an injection molded multi-well plate (Fig. 2A), and electrochemical measurements were performed by immersion of a reference electrode and a counter electrode into each well (Fig. 2B and C).

Optical dark-field micrographs of the resulting electrode arrays are presented in Fig. 3A (center rows). Arrays with edge-to-edge separations of 30 μm could be produced routinely. We modeled chronoamperometric analysis on all four electrode configurations. The resulting solution concentration of the redox active species after 90 s of analysis is shown in Fig. 3A (top and bottom). Both sets of 30 μm electrodes behave largely as independent electrodes with hemispherical concentration gradient profiles. In contrast, the closely spaced 100 μm electrodes (distance 130 μm) develop an almost planar diffusion profile above the center electrode. The resulting reduced redox kinetics mainly affects the center electrode of this 3×3 array, i.e., one out of nine electrodes. In square arrays containing more electrodes, the fraction of electrodes affected will obviously be higher. Increasing the electrode spacing to 300 μm reduces the effect, with each electrode largely acting as an individual \varnothing 100 μm electrode.

Complete removal of TOPAS[®] was verified by SEM analysis. Grounding of the PEDOT layer prevented electrostatic charging of the electrodes during imaging and allowed a clear differentiation to charged TOPAS[®] residues. Furthermore the geometry as well as the dimensions of the electrodes were quantified by SEM. All analysed electrodes had a circular shape of $94.8 \pm 0.6 \mu\text{m}$ and $32.2 \pm 0.5 \mu\text{m}$ in diameter for \varnothing 100 μm and \varnothing 30 μm electrodes, respectively (Fig. 3B).

Fig. 4 compares the modeled and the experimentally obtained chronoamperometric measurements. Modeling of the electrochemical kinetics shows a much slower approach to steady state for \varnothing 100 μm electrodes (Fig. 4A) than for the \varnothing 30 μm electrodes (Fig. 4C). For both electrode dimensions (Fig. 4A and C), a spacing of 130 μm (trace “b”) is observed to yield a significantly smaller current at all time points compared to a spacing of 300 μm (trace “c”). This is in agreement with the planar diffusion field for \varnothing 100 μm electrodes with a spacing of 130 μm shown in Fig. 3A (top left cross-section) and indicates an overlapping diffusion radii also

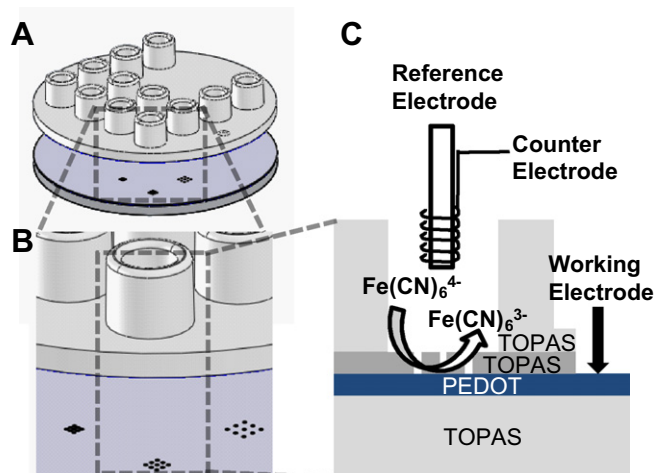


Fig. 2. (A) Multiple microelectrode arrays with different spacings are bonded to an injection molded TOPAS[®] multi-well system [6]. (B and C) Electrochemical analysis proceeds by immersion of a counter- and reference-electrode into the well while contacting the PEDOT layer as working electrode.

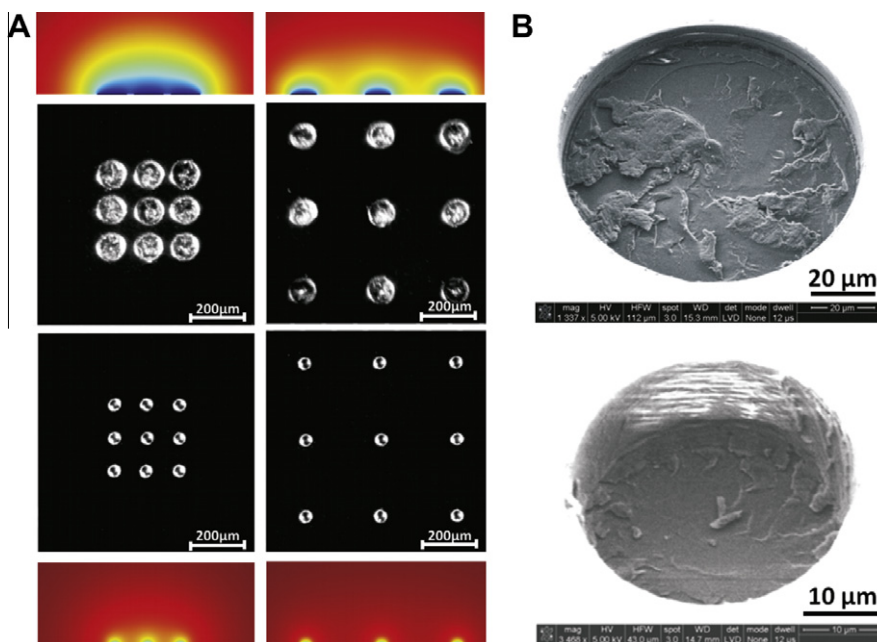


Fig. 3. (A) Center rows: dark-field micrographs of the fabricated microelectrode arrays of spacings 130 μm (left) and 300 μm (right). The upper and lower rows show electrodes produced using a \varnothing 100 μm or \varnothing 30 μm tool, respectively. Top and bottom rows: finite element modelling of the redox active species concentration, shown above the respective electrode arrays after running chronoamperometric measurements for 90 s. The graphs are presented as cross-sectional views through the three center electrodes of each array (dark red: initial concentration; black: zero concentration). (B) SEM of a single \varnothing 100 μm (top) and \varnothing 30 μm (bottom) electrode in a 30 tilted perspective. (For interpretation of the references to color in this figure legend, the reader is referred to the web version of this article.)

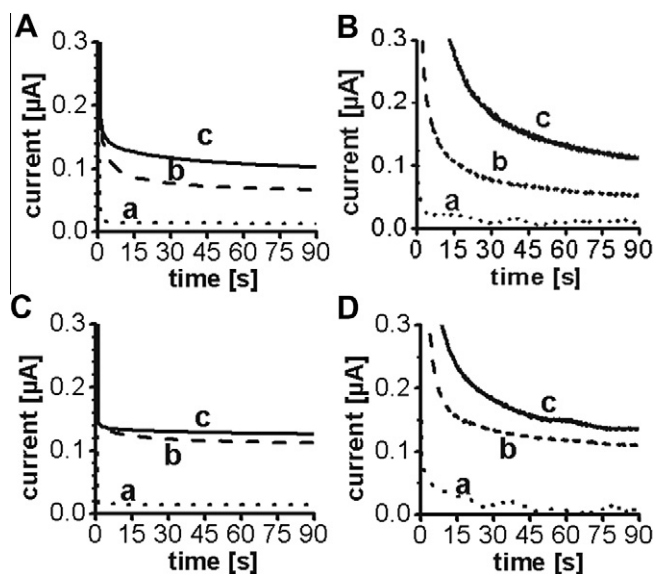


Fig. 4. Comparison of chronoamperometric results from modelling (A and C) and from experiments (B and D) using PEDOT microelectrodes. (A) Modelling of \varnothing 100 μm electrodes; trace (a) is a single electrode, while traces (b) and (c) are 3×3 arrays with spacings of 130 μm and 300 μm , respectively. (B) Experiments on \varnothing 100 μm electrodes. (C) Modelling of \varnothing 30 μm electrodes. (D) Experiments on \varnothing 30 μm electrodes.

for the \varnothing 30 μm electrodes. The experimental results display a similar trend: The dense arrangement of \varnothing 100 μm electrodes (center-to-center spacing of 130 μm) caused a reduced steady state current of 77 ± 22 nA (simulation: 66 nA) compared to 105 ± 8 nA (simulation 102 nA) for independently acting electrodes with 300 μm spacing (Fig. 4B). Interference of the diffusion radii of the electrodes was also found for \varnothing 30 μm electrode arrays. Steady state currents of 97 ± 17 nA (simulation 112 nA) and 128 ± 10 nA (simu-

lation: 126 nA) for arrays with spacings of 130 μm and 300 μm , respectively, were recorded (Fig. 4D).

The experimentally determined rate of approach to steady state is much slower than the modeled kinetics, even for single electrodes (Fig. 4, traces “a”). We attribute this discrepancy in time to the electrochemical activity of the PEDOT electrodes themselves: The potential step applied to initiate the chronoamperometric measurement will result in partial oxidation of the PEDOT layer to establish a new equilibrium condition [3]. The latter process may last several minutes and will be overlaid on the response from the redox active species in solution. We investigated this hypothesis by comparing chronoamperometric measurements on microelectrode arrays, first with pure KCl solution, the second time using potassium ferrocyanide, and the third time in pure KCl solution again. Representative results are presented in Fig. 5, together with a trace “d” showing the difference between the first and sec-

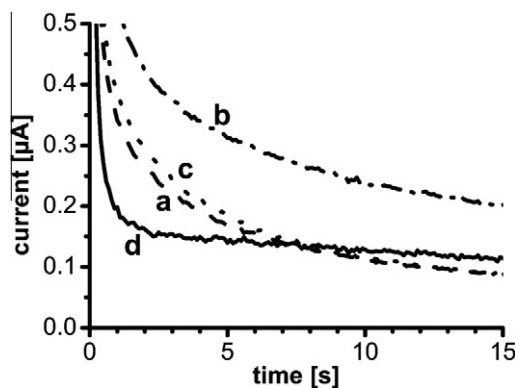


Fig. 5. Chronoamperometric measurements on a 3×3 array of \varnothing 100 μm microelectrodes with a spacing of 300 μm . Traces (a) through (c) are measured sequentially using (a) 0.1 M potassium chloride solution, (b) 1 mM ferro-/ferrocyanide in 0.1 M potassium chloride, and (c) 0.1 M potassium chloride. Trace (d) is the calculated difference of (a) and (b).

ond experiments. The latter clearly supports our hypothesis by showing that the current contribution from the dissolved redox active species approaches steady state within a few seconds, as expected from modelling (Fig. 4A, trace “c”). Analysis of the extracted current contribution after 15 s resulted in a steady state current for \varnothing 100 μm electrode arrays of 72 ± 2 nA as well as 104 ± 11 nA with spacings of 130 μm and 300 μm , respectively. This is in good agreement with 66 nA and 102 nA predicted by the simulation of the small and large spaced arrays, respectively. The same tendency was found for \varnothing 30 μm electrode arrays. Currents of 113 nA and 140 ± 14 nA were calculated for arrays with spacings of 130 μm and 300 μm , respectively, compared to predicted currents of 112 nA and 126 nA, respectively.

4. Summary

Resistance-controlled microdrilling through a protective insulating polymer layer was successfully used to prototype microelectrode arrays in the conducting polymer PEDOT with minimum demonstrated electrode widths and separations of 30 μm . Multiple microelectrode arrays bonded to a polymer multi-well part were analyzed individually by chronoamperometry, and the general trends at steady state agreed with results obtained from finite element modeling of the arrays. However, a significant discrepancy was observed for the kinetics of the manufactured electrodes, with

much slower approach to steady state than predicted. Subtraction of the contribution from the PEDOT electrode led to excellent agreement of time scales and current levels between the models and the experiments. These results demonstrate that the access to fast prototyping of real microelectrode arrays is of great importance when designing electrochemical analytical systems that use conducting polymer microelectrodes.

Acknowledgements

This work was financially supported by the Danish Research Council for Technology and Production Sciences Grant 26-04-0074. We thank Maciej Skolimowski for helpful discussions and technical support.

References

- [1] J. Kafka, N.B. Larsen, S. Skaarup, O. Geschke, *Microelectron. Eng.* 87 (2010) 1239.
- [2] J. Heinze, *Angew. Chem.* 32 (1993) 1288.
- [3] J. Heinze, B.A. Frontana-Urbe, S. Ludwigs, *Chem. Rev.* 110 (2010) 4724.
- [4] G. Vazquez, E. Alvarez, J.M. Navaza, *J. Chem. Eng. Data* 40 (1995) 611.
- [5] M. Kakihana, H. Ikeuchi, G.P. Sato, K. Tokuda, *J. Electroanal. Chem.* 117 (1981) 201.
- [6] K.O. Andresen, M. Hansen, M. Matschuk, S.T. Jepsen, H.S. Sorensen, P. Utko, D. Selmecki, T.S. Hansen, N.B. Larsen, N. Rozlosnik, R. Taboryski, *J. Micromech. Microeng.* 20 (2010) 055010.

